UNDERSTANDING THE SLOW TRANSIENT OPTOELECTRONIC RESPONSE OF HYBRID ORGANIC-INORGANIC HALIDE PEROVSKITES

by

Daniel Louis Jacobs

A dissertation submitted to the faculty of
The University of Utah
in partial fulfillment of the requirements for the degree of

Doctor of Philosophy

Department of Materials Science and Engineering

The University of Utah

May 2017

Copyright © Daniel Louis Jacobs 2017

All Rights Reserved

The University of Utah Graduate School

STATEMENT OF DISSERTATION APPROVAL

The dissertation of **Daniel Louis Jacobs**

has been approved by the following supervisory committee members:

Ling Zang	, Chair	**12/07/2016** Date Approved
Jennifer Shumaker-Parry	, Member	**12/07/2016** Date Approved
Michael A. Scarpulla	, Member	**12/07/2016** Date Approved
Ashutosh Tiwari	, Member	**12/07/2016** Date Approved
Rajesh Menon	, Member	**12/07/2016** Date Approved

and by **Feng Liu** , Chair/Dean of

the Department/College/School of **Materials Science and Engineering**

and by David B. Kieda, Dean of The Graduate School.

ABSTRACT

Hybrid organic-inorganic halide perovskites, particularly methylammonium lead triiodide ($MAPbI_3$), have emerged within the past decade as an exciting class of photovoltaic materials. In less than ten years, $MAPbI_3$-based photovoltaic devices have seen unprecedented performance growth, with photoconversion efficiency increasing from 3% to over 22%, making it competitive with traditional high-efficiency solar cells. Furthermore, the fabrication of $MAPbI_3$ devices utilize low-temperature solution processing, which could facilitate ultra low cost manufacturing. However, $MAPbI_3$ suffers from significant instabilities under working conditions that have limited their applications outside of the laboratory. The instability of the $MAPbI_3$ material can be generalized as a complex, slow transient optoelectronic response (STOR). The mechanism of the generalized STOR is dependent on the native defects of $MAPbI_3$, but detailed understanding of the material defect properties is complicated by the complex ionic bonding of $MAPbI_3$. Furthermore, characterization of the intrinsic material's response is complicated by the diverse approach to material processing and device architecture across laboratories around the world. In order to understand and mitigate the significant problems of $MAPbI_3$ devices, a new approach focused on the material response, rather than the full device response, must be pursued.

This dissertation highlights the work to analyze and mitigate the STOR intrinsic to $MAPbI_3$. An experimental platform was developed based on lateral interdigitated

electrode (IDE) arrays capable of monitoring the current and photoluminescence response simultaneously. By correlating the dynamics of the current and photoluminescence (PL) responses, both charge trapping and ion migration mechanisms were identified to contribute to the STOR. Next, a novel fabrication technique is introduced that is capable of reliably depositing $MAPbI_3$ thin films with grain sizes at least an order of magnitude larger than most common techniques. These films were studied with confocal microscopy to give insight into the intra-grain PL dynamics of $MAPbI_3$. Finally, the lateral IDE device platform was used to study the composition and morphology dependent STOR and revealed important correlations between defect formation and the STOR. These results represent an important step toward realizing a deeper understanding of the intrinsic limitations of $MAPbI_3$ needed to progress the technology outside of the laboratory.

To my parents who have provided unending support and encouragement at every turn throughout my life. To my wife for her love, support, and being my best friend through all of the adventures we have had together, and those still to come.

TABLE OF CONTENTS

LIST OF FIGURES

ACKNOWLEDGEMENTS

I would like to thank my advisor, Dr. Ling Zang, for providing me with this great opportunity. This dissertation would not have been possible without his constant insight, support, and encouragement to pursue my research interests. I would also like to thank my fellow lab members for making the past 6 years a fun and supportive place to work. Specifically, I would like to thank Dr. Benjamin Bunes for his guidance through the graduate program and for being the sounding board to bounce off all of my terrible ideas. I would also like to thank my Integrative Graduate Education and Research Traineeship Program (IGERT) co-advisor, Dr. Jennifer Shumaker-Parry, for her support and guidance in the initial years of my graduate studies, as well as the lab members in the Shumaker-Parry group for welcoming me into the world of nanocrescent fabrication. Furthermore, I would like to thank Dr. Michael Scarpulla for his collaboration and insight that helped make this thesis project possible. Finally, I would like to thank Dr. Jordan Gerton and Lauren Simonsen for their generous help with the confocal studies and entrusting me to use their impressive and delicate confocal microscope.

I am very thankful for the support of the National Science Foundation (NSF) IGERT fellowship that allowed me the freedom to pursue a novel and collaborative research topic when I entered the graduate program. Similarly, I would like to thank the Utah Science Technology and Research (USTAR) program and the University of Utah for their generous funding.

Finally, I would like to thank my family and friends for their endless support and encouragement that not only helped me get through graduate school, but who have shaped me into the person I am today.

CHAPTER 1

INTRODUCTION

1.1 Motivation for Solar Energy

Growing populations and the rise of developing nations across the globe are demanding an ever increasing energy supply.[1] Currently, 78% the worldwide energy demand is met with fossil fuel-based energies including coal, oil, and natural gas. The impact of suppling this increasing energy demand with fossil fuel-based energies can have disastrous effects on the environment. Since the 1700s before the industrial revolution, the atmospheric CO_2 concentration has increased about 40% from 280 ppm to 400 ppm today.[2] If the global energy source continues to be dominated by fossil fuels with no goals to incorporate renewable energies, the CO_2 concentration is expected to continue to increase at an alarming rate with irreversible global temperature increasing by more than 2˚C.[3] Thus, it is essential that clean and renewable energy technologies be adopted to prevent further environmental damage.

Solar energy is the largest energy resource on the planet by a huge margin, as clearly depicted in the schematic in Figure 1.1. In fact, in only 90 min of sunlight, the earth's surface receives roughly 1.5×10^5 TWh of energy,[4] which is nearly the amount of energy that was consumed across the globe in the entire year of 2012. In addition to the abundance of solar energy available, it is also completely free and renewable, making the

motivation to adopt solar energy technologies clear. Of the different types of solar energy technologies, photovoltaics (PV) has several advantages making it the fastest growing electricity source in the world. In contrast to many other energy sources, PV energy is passive (requires no input of energy or materials to extract the energy), modular (can be easily scaled to meet specific demands), and can be installed for residential, industrial, as well as utility energy generation. The onsite power of solar energy makes it particularly advantageous for the developing nations that are expected to add the majority of the growing energy demands in the coming decades,[1] since infrastructure will not necessarily need to be built to supply rural areas with electricity and these nations generally are close to the equator where solar energy is even larger. Thus, PV energy has the highest potential to provide clean and cost-effective energy to the increasing global population.

1.2 Photovoltaic Theory

A PV device uses a semiconductor material that is able to absorb light energy from the sun and convert it into electricity. Light is absorbed in a semiconductor when it has an energy greater than or equal to the band gap of the material, at which point it can promote an electron from the valence band into the conduction band of the lattice leaving behind a positively charged hole in the valence band causing the material to be conductive. If electrical contacts are applied, the electrons and holes can be conducted through the material by applying a bias. In order to extract power out of the device, a rectifying junction is required. A general rectifying junction is created by putting a negative (n-type) material in contact with a positive (p-type) material creating an internal electric field, as depicted in the schematic in Figure 1.2a. The material is n-type or p-

typed by doping the semiconductor with specific atoms that either add excess electrons into the conduction band (n-type) or remove electrons from the valence band, effectively adding excess holes (p-type). If the semiconductor is not doped, it is considered intrinsic. Doping shifts the average energy level of the electron (Fermi level, E_f) from the center of the band gap (intrinsic case), to either just under the conduction band (n-type) or just above the valence band (p-type). Figure 1.2b shows the energy diagram of a general p-n junction at zero applied voltage labeling the Fermi level with respect to position along the p-n junction. Under light illumination, photogenerated charges are created throughout the material, producing minority electrons in the p-type side and holes in the n-type side. The internal electric field at the junction will cause the electrons to drift into the n-type and holes into the p-type side, causing a negative generation current.

The performance of a solar cell is measured with current density-voltage (JV) scans. The p-n junction current density, J, as a function of the applied voltage, V, is described as

$$J = J_0 \left[exp\left(\frac{qV}{kT}\right) - 1 \right] - J_L \qquad [1.1]$$

where J_0 is the saturated current density of the p-n diode, q is the elementary charge, k is the Boltzmann's constant, T is the temperature, and J_L is the light generated current density.[5] A graph of a typical JV curve is shown in Figure 1.2d. There are three important parameters that can be extracted from the JV curve that are used to compare the performance across photovoltaic devices: the short circuit current density (J_{sc}), the open circuit voltage (V_{oc}), and the fill factor (FF). The J_{sc} is a measure of the amount of

generation current, with no energy, that is collected when no voltage is applied (Figure 1.2b). This is largely a factor of the light intensity and the optical absorption properties of the material. The V_{oc} is a measure of the maximum voltage created at flat-band conditions where the drift current of the photogenerated carriers is equal to the opposite diffusion current created by the concentration gradient resulting in a net zero current (Figure 1.2c). The V_{oc} can be understood as chemical potential difference between the collected electrons and holes as seen in Figure 1.2c. The *FF* is a measure of the junction performance compared to the ideal case. It is calculated by the ratio of the product of the maximum power point voltage (V_{mp}) and current (J_{mp}) to the product of the V_{oc} and J_{sc}. A high performing rectifying junction will have a very square JV curve and a *FF* close to 1. The efficiency of the solar cell device is then calculated as:

$$\eta = \frac{J_{sc}V_{oc}FF}{P_{in}} \qquad [1.2]$$

where P_{in} is the incident light power. For testing and comparing solar cells, the P_{in} is based on the solar spectrum that passes through an air mass of 1.5 atmospheres (AM1.5) and is roughly 1000 W/m^2. A detailed balance based on thermodynamic losses can then be used to estimate the theoretical maximum solar cell efficiency, known as the Shockley-Queisser limit. This limit shows that the maximum attainable efficiency for a single junction solar cell is 33% from a semiconductor with a bandgap of 1.4 eV.[6] However, this only takes into account thermodynamic losses, and not inescapable extrinsic losses due to reflection off the surface or defects in the semiconductor. Thus, approaching the Shockley-Quessier limit is a significant challenge that requires

optimization of every aspect of the solar cell material properties, architecture, and optical properties.

1.3 Photovoltaic Technologies

1.3.1 Driving force for innovation in photovoltaic technologies

In order to realize large scale installation of photovoltaic energy, the price of solar energy is a more important parameter than the ultimate efficiency, since solar energy needs to compete with other sources of electricity, particularly coal.[1] The SunShot initiative in the US has set goals for the total installed cost of photovoltaic energy to have a levelized cost of electricity (LCOE) of $1.00/W by 2020 to achieve grid parity.[7] In order to do this, there are several benchmarks, including hard costs (module price) and soft costs (supply chain, installation, taxes, fees, etc.), that must be met. Concerning the module costs, the initial SunShot goal is to manufacture a module at or below $0.06/kWh by 2020.[7] Current module costs are close to the goal at around $0.07/kWh.[8] However, to meet and surpass this important benchmark, significant effort to reduce the module cost of photovoltaic technology through either improving the efficiency and manufacturing costs of established technologies, or developing new PV technologies, is still needed. These efforts are summarized in Figure 1.3, which shows the certified performance evolution of all PV technologies over three decades.

1.3.2 Introduction to photovoltaic technologies

The most common PV system is based on silicon, which dominates the PV market at 93%.[9] Silicon has many advantages as a solar material, including earth abundance and it is a mature technology, meaning less upfront manufacturing costs. The record silicon cell efficiencies are 25.6% and 21.25% for single and multicrystalline silicon devices, respectively.[10] However silicon is an indirect bandgap material (meaning it has low optical absorption), has a bandgap of 1.1 eV (lower than the optimum based on the Shockley-Queisser limit), and requires highly crystalline thick (> 150μm) wafers to afford sufficient absorption of sunlight, which significantly raises the manufacturing and material costs.[11-12] Despite their dominance in the market, these disadvantages may limit the ultimate levelized cost of electricity (LCOE) of silicon devices, and alternative systems need to be investigated. Gallium Arsenide (GaAs) based PV devices hold the highest record single junction solar cell efficiency across all PV technologies at 28.8%.[10] These solar cells use a thin film of single crystal GaAs, which has ideal optoelectronic properties (direct band gap of 1.4 eV). However, the price of GaAs is about 2 orders of magnitude higher than that of silicon,[13-14] making them useful only for space applications where cost is less important. Other PV technologies that have a better possibility to compete with silicon include cadmium telluride (CdTe) and copper indium gallium selenide (CIGS). These technologies use only a thin polycrystalline film (<5 μm), which can be deposited via large area deposition techniques, resulting in the material price to be only a fifth of the module price.[12] The record cell efficiencies of both of these technologies are catching up with that of silicon at 22%.[15] However, these materials contain toxic (cadmium) or rare and expensive (gallium, indium, tellurium) materials that

make large production scale-up a challenge. Third-generation devices are being developed with the goal to use only earth abundant and nontoxic materials. These include chalcopyrite (copper zinc tin sulfide/selenide, CZTS) solar cells, organic photovoltaic (OPV), and dye sensitized solar cells (DSSC). All of these third generation technologies have advantage in using thin films that can be solution processed, bringing down the manufacturing costs significantly. Despite their economic potential, their efficiencies are still around 11%[10] and have stability issues that ultimately decrease their LCOE compared to the more established technologies. Thus, there is still a need to develop a photovoltaic material that meets the standard of being abundant, inexpensive, stable, and capable of high efficiencies.

1.3.3 Motivation for hybrid halide perovskite technologies

Organic-inorganic hybrid halide perovskite photovoltaics is a relatively recent technology that has made unprecedented progress in less than a decade, as seen in Figure 1.3. The first use of a hybrid halide perovskite material in solar cell application was in 2009 by Kojima et al. in a DSSC device where methylammonium lead triiodide ($MAPbI_3$) was used only as the light absorber.[16] This device exhibited a modest efficiency of 3.9% and showed very fast degradation. However, since then $MAPbI_3$-based perovskite solar cells have shown unprecedented performance growth with record lab scale efficiencies already above 22%.[10] Beyond the high efficiencies, $MAPbI_3$ is made of extremely low cost and earth abundant materials (lead, methylamine, and iodide), uses an ultra thin active layer (< 500 nm), can be processed from a number of low-temperature solution deposition techniques, and can be printed on flexible substrates. Thus, the perovskite

solar cell not only matches the ultra low material cost of the third-generation PV technologies, but can match the performance of high-efficiency thin film inorganic solar cells. Moreover, the ultra light weight and flexibility give them the capability for high throughput manufacturing, such as roll to roll printing, and novel low-cost module installation that can further reduce soft costs and bring down the LCOE.[17-18] However, $MAPbI_3$, and its derivatives, suffer from significant degradation leading to challenging stability issues that limit their introduction into the market.[19-20] Furthermore, while the performance is already over 22%, theoretical understandings of the material properties are still largely unknown, so effective, systematic optimization is challenging.[21] Despite the current challenges facing perovskite photovoltaics, the unprecedented performance growth and cost effectiveness of the technology have really exciting potential to transform the solar energy market if the stability issues can be understood and mitigated.

1.4 Fundamental Properties of $MAPbI_3$ Perovskite Material

1.4.1 Structural properties of hybrid halide perovskite materials

Perovskite is a general crystal structure first discovered in the mineral, calcium titanate ($CaTiO_3$), but is seen in many different materials with the general structure formula of ABX_3. Most of the naturally occurring perovskite materials are oxide perovskites, however, in halide perovskite, the oxygen is replaced with a halide anion at the X-site. In hybrid halide perovskites, the A-site is an organic ammonium cation and the B-site is a divalent metal cation. The optimal cubic structure has the B-site cation with 6-fold octahedral symmetry surrounded by the X-site anion, and the A-site cation with 12-fold cuboctahedral symmetry with the surrounding X-site anions, as seen in

Figure 1.4a. Formation of the perovskite structure is very sensitive to the relative ion sizes, which is related by the Goldschmidt tolerance factor, *t*, defined as:

$$t = \frac{r_A + r_X}{\sqrt{2}(r_B + r_X)} \quad [1.3]$$

where r_A, r_B, and r_X are the atomic radii of the A-site cation, B-site cation, and X-site anion, respectively. The ideal case is $t = 1$, which will have a cubic perovskite structure. Generally, the stability of the perovskite is limited to $0.8 < t < 1$, but there are many difficulties in relating the hybrid halide perovskites to this tolerance factor. For example, the heavy iodide ion is much less electronegative compared to O^{2-}, meaning the hard sphere model to calculate the ionic size may not be relevant. Similarly, the A-site cation is an organic cation, and cannot be reliably modeled as a sphere with a defined radius. Nevertheless, this factor is still relevant to predicting the hybrid halide perovskites.[22]

$MAPbI_3$ has a tetragonal crystal structure at room temperature with a lattice constant of a=b=8.8 Å and c=12.67 Å, as depicted in Figure 1.4b.[23] Below 162.2 K, it exists in an orthorhombic phase, and above 327.4 K it exists in a cubic phase.[24] Substitutions of all lattice sites can be made to tune the optoelectronic properties as well as the stability of the material. Interestingly, the energy bands of the hybrid halide perovskite materials are defined only by the BX_6^{4-} octahedral, and the A-site cation only acts to neutralize the charge of the PbI_6^{4-} lattice. Therefore, substituting the B-site or X-site will directly change energy bands of the material. For example, halide substitution with Br^- and Cl^- will lead to an increase in the band gap to 2.3 and 3.7 eV, respectively, but such large band gaps make them impractical for solar applications. Tin (Sn)

substitution at the B-site has gained research interest due to the replacement of the toxic lead with a nontoxic, but still earth abundant element. The Sn-based perovskites have a lower bandgap at 1.3 eV for full substitutions,[25] and interestingly show a further reduction in bandgap with partial substitution with Pb, making them useful as bottom cell candidates in multijunction solar cell devices.[26] However, Sn will quickly oxidize to Sn^{4+} under ambient conditions, which has limited their use in devices. Substitutions at the A-site with ions of different sizes is more difficult due to the already large size of the MA ion. Formamadinium (FA) has been the only other organic cation successfully incorporated into the 3-D perovskite structure, which leads to a slight reduction of the bandgap but quickly destabilizes to a nonperovskite phase at room temperature.[27] The material can be stabilized with partial substitution of MA at the A-site or Br at the X-site. If the organic cation is larger than FA, the perovskite structure can break down into a 2-D perovskite phase, where single layers of the PbI_6 corner sharing octahedral are isolated by the larger organic cation, such as butylammonium (BA). This causes quantum confinement of the energy bands to the semiconducting PbI_6 layers resulting in widening the bandgap to energies not applicable to photovoltaics. However, partial substitution of BA to form $(MA)_{n-1}(BA)_nPb_nI_{3n+1}$ will form the Ruddelson-Popper phase, where BA layers will surround n-layers of the 3-D $MAPbI_3$ phase, as seen in Figure 1.3c, and results in a reduction of the bandgap towards that of $MAPbI_3$ as n approaches infinity.[28-31]

1.4.2 Fundamental optoelectronic properties of $MAPbI_3$

While the range of potential hybrid halide perovskite materials is broad, $MAPbI_3$ remains the most studied material for solar cell applications. The high-efficiency stems

from the good intrinsic optoelectronic properties. $MAPbI_3$ has a direct bandgap of 1.6 eV, slightly larger than the optimum value, and a high absorption coefficient comparable to, if not slightly better than, most thin film solar cell materials.[32] The exciton binding energy of $MAPbI_3$ is calculated to be lower than 50 meV.[33-35] This suggests that the material creates free charge carriers upon excitation at room temperature rather than exhibiting excitonic characteristics. Single crystal $MAPbI_3$ shows low carrier concentrations on the order of 10^{10} and remarkably low trap state concentrations on the order of 10^9,[36-38] implying it is an intrinsic compound semiconductor.[37] The effective masses are calculated to be low (around $0.1m_0$-$0.2m_0$) for both electrons and holes implying efficient amipolar transport.[34, 39-40] This leads to mobilities along the range of 10^3 $cm^2V^{-1}s^{-1}$ for electrons and holes in single crystals. One unique property of $MAPbI_3$ that has been challenging for theoretically understanding is the role of the MA molecule. Since the positive charge sits on the nitrogen group of the molecule, a strong permanent dipole of about 2.3 debye is created.[34] Furthermore, the molecule is short, and can rotate within the lattice void, with the possibility of long range dipole alignment leading to ferroelectric effects. Although, at room temperature, it is expected that the thermal energy is too large to exhibit any significant ferroelectric effect.[41] That being said, the result of a freely rotating dipole could be a mechanism for the efficient charge separation and reduced recombination observed in $MAPbI_3$.[41-42]

1.4.3 Intrinsic defects in $MAPbI_3$

As in any optoelectronic device, the performance is highly dependent on the defects of the materials, and controlling these defects is essential for optimization of the

device. Defect formation in compound semiconductor materials is typically regulated by the relative chemical potential of each atomic/molecular species during crystallization. However, the strong ionic bonding of $MAPbI_3$ leads to very rich and complex defect chemistry. Calculations of the defect formation energies of the possible point defects reveal that vacancies (V_{MA}, V_I, and V_{Pb}) have the lowest formation energies and hypothesized to be the dominant defects.[43-45] These defects have energy levels close to the band edges making V_I an intrinsic donor and V_{Pb} and V_{MA} intrinsic acceptors. The lack of deep level trap states with low formation energy is likely a significant reason behind the favorable optoelectronic properties of $MAPbI_3$. Furthermore, it has been calculated that within a broad window of growth conditions, the formation energies of the dominant vacancy defects are actually not dependent on the chemical potentials of the various species.[44, 46-47] One hypothesis for this phenomenon is the low (close to zero) formation enthalpy for $MAPbI_3$, meaning that there is low enthalpy barrier for the formation of MAI and PbI_2. Schottky defect formation, where vacancies of positive and negative ions are formed together maintaining a net neutral charge, are expected to be a major defect type.[44, 47] This can theoretically lead to large defect concentrations, with low charge carrier densities, which to some extent has been observed theoretically.[44] However, experimental measurements have found the perovskite to be mostly n-type.[48-49] While the n-type doping is relatively weak ($n \sim 10^{14}$), it is likely a result of excess iodide vacancies being the most common defect species.[49]

Generally, defects with deep level trap states that could lead to nonradiative recombination in $MAPbI_3$ have much higher formation energy than the low lying defects, suggesting that nonradiative recombination in the bulk crystal is low. However,

calculations have shown that under specific growth conditions, the formation energy of these deep level defects may significantly decrease. It was calculated that under I-rich growth conditions, antisite defects, such as Pb_I (replacement of Pb with I), may have low formation energies and can be lead to significant nonradiative recombination.[43] Thus, I-poor growth conditions (using an alternative lead source to PbI_2) could decrease the deep level trap formation. Alternatively, it was calculated that stabilization of vacancy defects, such as V_I can lead to strong covalent bonding to form a Pb-dimer state with a mid gap energy level acting as a recombination center.[50]

For the dominant vacancy defect species, it was calculated that V_I and V_{MA} might also have low hopping activation energy enabling mobile charged defects.[51-52] V_I defects are expected to have the lowest activation energy for migration ($0.08 < E_a < 0.5$) making them likely to migrate under working conditions. However, the activation energy for migration of V_{MA} may be too large ($0.46\ eV < E_a < 0.84$) to permit room temperature migration. The implications of mobile defect states are significant considering the large concentrations of these vacancy defects. The potential impact of these mobile defects on the performance will be discussed in a later section.

1.4.4 Intrinsic degradation of $MAPbI_3$

One of the major promises of $MAPbI_3$ to realize cost-effective solar energy, is the capability to use low-temperature processing. This is a result of the low enthalpy of formation as described in the previous section. However, a low energy of formation also implies that the reversing to its initial state also requires less energy. Indeed, $MAPbI_3$ suffers from severe degradation effects that limits its potential as a robust solar cell

material. In particular, water vapor can result in complete degradation of the material to PbI_2 within days at ambient humidity, or hours at higher humidity depending on the exact film properties and encapsulation.[53] It is hypothesized that the water acts to disrupt the hydrogen bonding between MA^+ and PbI_6^{4-} lattice leading to deprotonation of MA^+ to form MA^0 and hydrogen iodide gas (HI), which can then evaporate from the surface leaving a PbI_2 film.[34, 53] Because the water vapor acts as a catalyst for degradation, rather than being used in the reaction, even small amounts of water can potentially lead to complete degradation overtime. Therefore, fabrication is usually done under inert environments.

Fabrication and testing performed in inert atmospheres, or with encapsulation, does substantially improve the stability of the device.[53-54] However, degradation can still occur under these controlled conditions. This is again likely a result of the low enthalpy of formation for $MAPbI_3$, which leads to large concentrations of mobile defects as described above. Under light illumination, increased temperature, and electrical bias, these defects can increase, migrate, and decompose to precursor phases.[55-56] Therefore, avoiding these defects is a significant challenge and must be considered to improve the stability of these perovskite materials.

1.5 $MAPbI_3$ Photovoltaic Devices

1.5.1 $MAPbI_3$ solar cell device architecture

Unlike most other PV technologies, there is not a true "standard" device architecture for $MAPbI_3$-based PV devices. This is a result of the interdisciplinary evolution of perovskite PVs. The first solar cells using $MAPbI_3$ were in DSSC device

architectures where nanoparticles of $MAPbI_3$ were used as the light sensitizer loaded onto a porous TiO_2 film, and they were capable of efficiencies as high as between 3% and 9%.[16, 57] However, the major breakthrough came from Lee et al. who discovered the efficient electrical properties of $MAPbI_3$ by replacing the electron conducting layer of TiO_2 nanoparticles with insulating Al_2O_3 nanoparticles, resulting in a performance just over 10% with an impressive V_{oc} of over 1 V.[23] This quickly led to the planar device architecture, where a thin film of $MAPbI_3$ is sandwiched between a thin compact TiO_2 film and the hole conducting polymer, and is representative of the "modern" perovskite PV architecture depicted in Figure 1.5a. It is noted that many of the high-efficiency devices today still use a very thin layer of porous TiO_2 to ensure uniform and pinhole-free films across large areas. These are known as mesoscopic devices, but the underlying mechanisms are the same as the planar devices since the TiO_2 does not contact the hole conductor.[23] Since the $MAPbI_3$ layer is not intentionally doped, this architecture, with TiO_2 deposited on the transparent conductive oxide (TCO) electrode substrate, is considered as an n-i-p junction. Here, the intrinsic $MAPbI_3$ layer is the optical absorbing layer as well as conducts electrons and holes, matching with the theoretical observations of efficient ambipolar transport as discussed above. The n and p-layers are termed the electron and hole transport layers (ETL, HTL), respectively, and serve to block the recombination of holes and electrons at the electrode interfaces.

This planar device structure resembles that of an organic solar cell device architecture, where the organic semiconducting thin film is similarly sandwiched between a HTL and ETL. Indeed, devices using the traditional OPV-based architecture with $MAPbI_3$ sandwiched between the conductive polymer, PEDOT:PSS, as the HTL and the

fullerene derivative, PCBM, as the ETL (forming a p-i-n junction), were able to produce comparable device efficiencies.[58] This subsequently lead to incorporating the large range of interface layers established in high-performance OPV devices, including: PEDOT:PSS,[58] NiO,[59] and P3HT[60] as hole transport layers (HTL), and C_{60},[61] PCBM,[58] PTCDI,[62] and ZnO[59] as the electron transport layers (ETL). These are only a few examples of the different ETL and HTL layers possible for use in $MAPbI_3$ solar cell devices. Furthermore, it has been shown that removing the ETL[63] or HTL[64] can still produce devices with efficiencies near 15%. This large range of potential interlayer materials adds significant challenges for comparing device performances and reaching a fully optimized device design.

1.5.2 $MAPbI_3$ deposition techniques

The strong ionic nature of the hybrid halide perovskites results in high solubility of precursor materials enabling facile solution-based and low-temperature deposition techniques as depicted in the schematics in Figure 1.5b. The synthesis of $MAPbI_3$ is generally performed by reacting the precursor compounds PbI_2 and MAI. The simplest technique to do this is a 1-step deposition technique. Here, the precursor solutions are mixed in a solvent, typically dimethyl formamide (DMF) or gamma butyrolactone (GBL), and the solution is deposited on the substrate through spin coating. The material is then crystallized as the solvent dries through thermal annealing at around 100˚C. Films from this 1-step approach tend to be hard to control and exhibit large grains and nonuniform films with significant pinhole areas, which is detrimental for photovoltaic devices.[65] The nonuniformity likely stems from slow nucleation kinetics due to strong solvent

interactions, but fast crystal growth kinetics once nucleated.[66] Solvent engineering can be used to control the crystallization kinetics to form smooth and uniform thin films. For example, by introducing a miscible bad solvent (dissolves DMF but not $MAPbI_3$) during the spin coating process, the fast removal of the good solvent will cause fast and uniform nucleation throughout the film resulting in a smooth, fine-grained film (200-500 nm).[67] A similar approach uses DMSO as the solvent or solvent additive, which is capable of forming a stable intermediate with $MAPbI_3$. After the deposition, the intermediate film is washed with the orthogonal solvent to crystallize the $MAPbI_3$.[68] Finally, the hot casting technique was developed and entailed deposition of a warmed solvent (70˚C) directly onto a hot substrate (>150˚C) leading to immediate crystallization. This produced films that had apparent grain sizes of hundreds of microns, although further analysis suggest that these grains actually consist of small crystal grains that form together in a Volmer-Weber growth mechanism.[69-70]

An alternative approach to deposit $MAPbI_3$ is the 2-step deposition technique. In contrast to the 1-step technique, where crystallization is governed by solvent evaporation, the 2-step technique reacts a predeposited PbI_2 film with MAI. The reaction can take place with MAI in the solid, liquid, or vapor phase. In the solid phase, MAI is deposited onto a PbI_2 thin film, typically by evaporation, followed by thermal annealing.[71] In the liquid phase reaction, the PbI_2 thin film is immersed into the orthogonal solution (where the organic halide has high solubility, but the metal halide has low solubility, typically isopropyl alcohol (IPA)) of MAI.[72] In the vapor phase, the PbI_2 is placed into a chamber with a vapor pressure of MAI created by heating MAI powder, and the PbI_2 film to modest temperatures of around 120-150˚C.[73] In all of these cases, the mechanism of

perovskite formation is diffusion of the organic halide into the metal halide film and subsequent reaction to form the perovskite phase. The controlled reaction leads to uniform, smooth, and fine grained films (< 1 μm). However, controlling the reaction can be challenging as it is sensitive to a number of parameters including the concentration of the MAI, morphology of the PbI_2 film, and the exact temperature of the system. Without precise and repeatable control of the conversion process, the films can have inconsistent compositions or unreacted phases.

Most deposition techniques require postdeposition thermal annealing to fully convert the film to the perovskite phase. Alternatively, solvent annealing can also be used as a postdeposition technique to enhance the thin film quality. In solvent annealing, the films are immersed in an atmosphere with high concentration of a polar solvent vapor, such as DMF, at elevated temperatures (~100˚C).[74] The solvent vapor can infiltrate the film, loosening the ionic bonding, and enable molecular and atomic rearrangement to realize higher crystallinity. The solvent annealing can also lead to larger grain sizes upwards of 1 micron. Similarly, methylamine (MA^0) gas can be used for a postdeposition annealing technique.[75-76] Surprisingly, introduction of MA^0 results in a complete breakdown of the ionic bonding in $MAPbI_3$ and a fast (< 1 s) phase transition into a $MAPbI_3$-$x$$MA^0$ liquid phase. When the MA^0 gas is removed, the phase transition quickly reverses, returning back to the solid state $MAPbI_3$. The resulting film exhibits much stronger and oriented crystallinity and ultra-smooth uniform films. However, in contrast to traditional solvent annealing, MA^0 exposure goes through a complete melting and fast recrystallization, so the grain sizes can be up to an order of magnitude smaller than the grains produced in the 2-step techniques.

1.5.3 Performance of $MAPbI_3$ photovoltaic devices

The performance of the $MAPbI_3$ photovoltaic devices varies largely due to the large variations of the device architecture, film deposition techniques and the material growth properties. Impressively, high-performance devices have been made across most of these parameter ranges, indicating the robust nature of these materials. Common average efficiencies of high-performance $MAPbI_3$ devices are around the mid-to-high teens with efficiencies above 18% common. The highest efficiency $MAPbI_3$-based devices have used both A-site cation substitution (FA/Cs) and X-site halide substitution (Br) to reduce the bandgap and stabilize the lattice, and they have efficiencies upwards of over 20%.[77] Still, the $MAPbI_3$ devices exhibit surprisingly performance parameters for a solution processed device, the most notable of which is the V_{oc} of these devices: $0.8 < V_{oc} < 1.1$ eV. Compare these to the record V_{oc} for the mature CdTe technology that has just recently exhibited a record V_{oc} of 1.0 eV dispite the similar bandgap.[78] The large V_{oc} in $MAPbI_3$ based devices is an indication of low concentrations of deep level trap states and possibly a result of efficient charge screening due to the MA dipole.[42] High-performance cells also have relatively high FF above 0.7. This is indicative of low series resistance (large mobility) of the $MAPbI_3$ and low shunt resistance (pin hole free, low diffusion of electrode atoms) due to the low-temperature processing.

The most glaring flaw in $MAPbI_3$ performance, beyond the degradation over time, is the existence of hysteresis in the JV curves. Depending on the rate of the JV scan, light soaking before JV measurement, or electrical bias before JV measurement, the JV curve can shift between forward and backward scans.[79] This has obvious implications on the reliable reporting of solar cell performance. The cause of the hysteresis is still a subject of

great debate across the field, with potential mechanisms including ferroelectric polarization of the MA ions,[34, 80] charge trapping in bulk or interface defect states,[70, 81] or ion migration of shallow charged defects leading to electric field compensation.[51-52, 82] To overcome the challenges with reliable reporting of device parameters, it is common to accompany JV performance curves with time resolved performance parameters over seconds to minutes to show that the performance is stabilized. However, the hysteresis is still a significant determent to bringing the technology from the lab bench to the market. The solar cell needs to have a stable and reliable performance that can be verified. Thus, understanding and mitigating the hysteresis effect is essential for the progression of perovskite solar cell technologies.

1.5.4 Slow transient optoelectronic response in $MAPbI_3$

The hysteresis effect observed in the JV scans of the perovskite devices was the first indication of slow transient optoelectronic response (STOR) in $MAPbI_3$. Measurement of time resolved photocurrent revealed that the current response to light and electrical bias exhibited a slow response to steady state on the order of up to tens of seconds.[80] Thus, depending on the scan rate of the JV measurement, the material might not be at steady state resulting in an undershoot, or overshoot, of the true steady state current. The mechanism of this is attributed to alignment of the molecular dipoles leading to a ferroelectric response,[80] charge trapping in bulk or grain boundary trap states,[81] or ionic migration leading to electric field compensation.[52, 83] While ferroelectric polarization is now not expected to be a significant contributor to at room temperature due to the fast molecular orientation of MA,[41] subsequent electrical measurements have

confirmed the existence of both charge trapping and ionic migration leading to the transient electric response. For example, tuning the ETL and HTL layers has been successful in reducing the hysteretic effect, signifying that the interface trap density has a significant contribution in the transient response.[81, 84-85] Furthermore, using fullerene as the ETL can significantly reduce the hysteresis by diffusing in the grain boundaries and passivating grain boundary traps. Alternatively, ion migration has been characterized through transient voltage and current measurements where the build up of space charge reduces the voltage or photocurrent. The low frequency response in impendence or capacitance measurements are also identified with ionic migration. As discussed above, the most likely mobile ions are expected to be V_{MA}^{-} and V_{I}^{+}.[51-52] Direct evidence of this ion migration effect was observed as a giant switchable photovoltaic effect, where light and voltage biasing of $MAPbI_3$ with symmetric electrodes could lead to diode behavior with a photovoltaic response.[82, 86-87] Since the mobile ions have shallow defect energy levels, they act as doping centers to create a dynamic n-i-p junction. Switching the bias during poling could reverse the effect, thus signifying the reversibility of the drifting of mobile ions. Reduction of ion migration could be challenging due to the high concentrations of defects that are expected at room temperature or even at higher working conditions. One way to alleviate this problem is to block the ion migration pathway, but the pathway for migrating ions is still under debate. Some research has suggested that ion migrate along the grain boundaries or at surfaces.[88] Therefore, reducing the grain boundary size through large crystalline grains is a promising route to reduce ionic migration. Indeed, using nanoscaled electronic probing with conductive AFM found that the transient response only occurred at the grain boundary. That being said, defects are

still expected to be mobile in the bulk phase.

In addition to the electronic slow transient response, there is also a light-induced slow transient photoluminescence (PL) response. Under extended light illumination from dark of $MAPbI_3$, a slow increase of the PL is observed.[89] However, the response is highly dependent on the environment. In dry oxygen atmospheres, the PL would show a strong increase over time in the minutes to hours time scale, but when it was switched to inert atmospheres, it would decrease.[90] From this it was determined that the oxygen can act to passivate low lying defect trap centers.[91] Alternatively, it was also hypothesized that iodide migration through diffusion under light bias was leading to trap deactivation as I_i diffused to V_I, for example.[56] Modulating the electric field can also lead to transient responses in the PL indicating that the electronic and light-induced slow transient responses are correlated. [92]

The mechanisms of the STOR, either ion migration or charge trapping, are dependent on the defect properties of the material. Therefore, to fully characterize the defect dependent STOR, there needs to be a standard from which the material variations can be reliably compared. However, as highlighted in the above section, the range of material deposition techniques and device architectures makes comparison of the intrinsic material response nearly impossible. Most research has focused more on optimization of material properties within a specific device architecture in order to maximize the performance for that system. Therefore, the intrinsic mechanism of $MAPbI_3$ and its derivatives is still under debate.

1.6 Dissertation Outline

The work presented in this dissertation highlights studies to understand and control the STOR using a standard platform to facilitate comparisons across samples and characterization techniques.

1.6.1 Development and characterization of a standard testing platform

An interdigitated electrode device was developed and used as a platform to effectively and reliably monitor optical and electrical transient responses. This device design enabled spatial, spectral, and dynamic measurements of the PL and simultaneous current measurements. Based on these studies, PL and current slow transient response trends were correlated to both ion migration and charge trapping mechanisms.

1.6.2 Fabrication of large grained $MAPbI_3$ thin films

A new annealing technique is introduced based on the solid to liquid phase transition of $MAPbI_3$ under methylamine gas atmosphere. It was discovered that this phase transition is reversible at higher temperatures. An annealing path was developed known as thermally induced recrystallization under methylamine atmosphere (TIRMA) by recrystallizing the $MAPbI_3$ film through slow heating under methylamine flow. The resulting films exhibited substantially larger grain sizes and improved crystallinity. Confocal microscopy was used to characterize the properties of the large highly crystalline grains. Initial analysis of the time and spectrally resolved PL mapping reveal the high quality of the $MAPbI_3$ films.

1.6.3 Compositional and morphological dependence of the STOR

The effect of $MAPbI_3$ precursor composition and the film morphology on the slow transient response was tested. Tuning the precursor concentration around the stoichiometric ratio revealed clear distinct trends in the slow transient optoelectronic responses. These trends were correlated to the expected dominant defects in $MAPbI_3$ based on the specific growth conditions. The proposed mechanisms leading to the variation in transient responses were supported by further testing the dependence on light intensity and electric field strength. Finally, TIMRA treated samples were tested within the IDE device platform, which revealed a significant decrease in the transient response, further supporting the hypothesis that the TIMRA films have smaller defect concentrations.

1.7 References

1. *International Energy Outlook 2016*; DOE/EIA-0484(2016); Office of Energy Analysis: Washington, DC, 2016.

2. Butler, J. H.; Montzka, S. A. The NOAA Annual Greenhouse Gas Index http://www.esrl.noaa.gov/gmd/aggi/aggi.html (accessed November 1, 2016).

3. IPCC *Climate Change 2014: Synthesis Report. Contribution of Working Groups I, II and III to the Fifth Assessment Report of the Intergovernmental Panel on Climate Change*; Intergovernmental Panel on Climate Change: Geneva, Switzerland, 2015.

4. Philibert, C. *Renewable Energy Technologies: Solar Energy Perspective*; International Energy Agency: Paris, France, 2011.

5. Sze, S. M.; Ng, K. K., *Physics of Semiconductor Devices*, 3rd ed.; John Wiley & Sons, Inc.: Hoboken, New Jersey, 2007.

6. Shockley, W.; Queisser, H. J., Detailed Balance Limit of Efficiency of p-n Junction Solar Cells. *J. Appl. Phys.* **1961,** *32*, 510-519.

7. Woodhouse, M.; Jones-Albertus, R.; Feldman, D.; Fu, R.; Horowitz, K.; Chung, D.; Jordan, D.; Kurtz, S. *On the Path to SunShot: The Role of Advancements in Solar*

Photovoltaic Efficiency, Reliability, and Costs; NREL/TP-6A20-65872; National Renewable Energy Laboratory: Golden, CO, 2016.

8. Philibert, C. d. *Technology Roadmap: Solar Photovoltaic Energy*; International Energy Agency: Paris, France, 2014.

9. *Photovoltaics Report*; Fraunhofer Institute for Solar Energy Systems: Freiburg, Germany, June 6, 2016.

10. Green, M. A.; Emery, K.; Hishikawa, Y.; Warta, W.; Dunlop, E. D., Solar Cell Efficiency Tables (Version 47). *Prog. Photovoltaics* **2016,** *24*, 3-11.

11. Green, M. A.; Zhao, J.; Wang, A.; Wenham, S. R., Progress and Outlook for High-Efficiency Crystalline Silicon Solar Cells. *Sol. Energ. Mat. Sol. Cells* **2001,** *65*, 9-16.

12. Jones-Albertus, R.; Feldman, D.; Fu, R.; Horowitz, K.; Woodhouse, M., Technology Advances Needed for Photovoltaics to Achieve Widespread Grid Price Parity. *Prog. Photovoltaics* **2016,** *24*, 1272-1283.

13. Schnebele, E. K. *Silicon: Material Commodity Summary*; United States Geological Survey: Reston, VA, 2016.

14. Jaskula, B. W. *Gallium: Materials Commodity Summary*; United States Geological Survey: Reston, VA, 2016.

15. NREL Best Research-Cell Efficiencies. http://www.nrel.gov/pv/assets/images/efficiency_chart.jpg (accessed 10/26/2016).

16. Kojima, A.; Teshima, K.; Shirai, Y.; Miyasaka, T., Organometal Halide Perovskites as Visible-Light Sensitizers for Photovoltaic Cells. *J. Am. Chem. Soc.* **2009,** *131*, 6050-6051.

17. Krebs, F. C.; Espinosa, N.; Hösel, M.; Søndergaard, R. R.; Jørgensen, M., 25th Anniversary Article: Rise to Power – OPV-Based Solar Parks. *Adv. Mater.* **2014,** *26*, 29-39.

18. Schmidt, T. M.; Larsen-Olsen, T. T.; Carlé, J. E.; Angmo, D.; Krebs, F. C., Upscaling of Perovskite Solar Cells: Fully Ambient Roll Processing of Flexible Perovskite Solar Cells with Printed Back Electrodes. *Adv. Energy Mater.* **2015,** *5*, 1500569.

19. Li, B.; Li, Y.; Zheng, C.; Gao, D.; Huang, W., Advancements in the Stability of Perovskite Solar Cells: Degradation Mechanisms and Improvement Approaches. *RSC Adv.* **2016,** *6*, 38079-38091.

20. Leijtens, T.; Eperon, G. E.; Noel, N. K.; Habisreutinger, S. N.; Petrozza, A.; Snaith, H. J., Stability of Metal Halide Perovskite Solar Cells. *Adv. Energy Mater.* **2015,** *5*, 1500963.

21. Egger, D. A.; Edri, E.; Cahen, D.; Hodes, G., Perovskite Solar Cells: Do We Know What We Do Not Know? *J. Phys. Chem. Lett.* **2015,** *6*, 279-282.

22. Travis, W.; Glover, E. N. K.; Bronstein, H.; Scanlon, D. O.; Palgrave, R. G., On the Application of the Tolerance Factor to Inorganic and Hybrid Halide Perovskites: A Revised System. *Chem. Sci.* **2016,** *7*, 4548-4556.

23. Lee, M. M.; Teuscher, J.; Miyasaka, T.; Murakami, T. N.; Snaith, H. J., Efficient Hybrid Solar Cells Based on Meso-Superstructured Organometal Halide Perovskites. *Science* **2012,** *338*, 643-647.

24. Ong, K. P.; Goh, T. W.; Xu, Q.; Huan, A., Mechanical Origin of the Structural Phase Transition in Methylammonium Lead Iodide CH3NH3PbI3. *J. Phys. Chem. Lett.* **2015,** *6*, 681-685.

25. Hao, F.; Stoumpos, C. C.; Cao, D. H.; Chang, R. P. H.; Kanatzidis, M. G., Lead-Free Solid-State Organic-Inorganic Halide Perovskite Solar Cells. *Nat. Photonics* **2014,** *8*, 489-494.

26. Eperon, G. E.; Leijtens, T.; Bush, K. A.; Prasanna, R.; Green, T.; Wang, J. T.-W.; McMeekin, D. P.; Volonakis, G.; Milot, R. L.; May, R.; Palmstrom, A.; Slotcavage, D. J.; Belisle, R. A.; Patel, J. B.; Parrott, E. S.; Sutton, R. J.; Ma, W.; Moghadam, F.; Conings, B.; Babayigit, A.; Boyen, H.-G.; Bent, S.; Giustino, F.; Herz, L. M.; Johnston, M. B.; McGehee, M. D.; Snaith, H. J., Perovskite-Perovskite Tandem Photovoltaics with Optimized Bandgaps. *Science* **2016,** *354*, 861-865.

27. Weller, M. T.; Weber, O. J.; Frost, J. M.; Walsh, A., Cubic Perovskite Structure of Black Formamidinium Lead Iodide, α-[HC(NH2)2]PbI3, at 298 K. *J. Phys. Chem. Lett.* **2015,** *6*, 3209-3212.

28. Cao, D. H.; Stoumpos, C. C.; Farha, O. K.; Hupp, J. T.; Kanatzidis, M. G., 2D Homologous Perovskites as Light-Absorbing Materials for Solar Cell Applications. *J. Am. Chem. Soc.* **2015,** *137*, 7843-7850.

29. Cheng, Z.; Lin, J., Layered Organic-Inorganic Hybrid Perovskites: Structure, Optical Properties, Film Preparation, Patterning and Templating Engineering. *CrystEngComm* **2010,** *12*, 2646-2662.

30. Stoumpos, C. C.; Cao, D. H.; Clark, D. J.; Young, J.; Rondinelli, J. M.; Jang, J. I.; Hupp, J. T.; Kanatzidis, M. G., Ruddlesden–Popper Hybrid Lead Iodide Perovskite 2D Homologous Semiconductors. *Chem. Mater.* **2016,** *28*, 2852-2867.

31. Tsai, H.; Nie, W.; Blancon, J.-C.; Stoumpos, C. C.; Asadpour, R.; Harutyunyan, B.; Neukirch, A. J.; Verduzco, R.; Crochet, J. J.; Tretiak, S.; Pedesseau, L.; Even, J.;

Alam, M. A.; Gupta, G.; Lou, J.; Ajayan, P. M.; Bedzyk, M. J.; Kanatzidis, M. G.; Mohite, A. D., High-Efficiency Two-Dimensional Ruddlesden–Popper Perovskite Solar Cells. *Nature* **2016,** *536*, 312-316.

32. Green, M. A.; Ho-Baillie, A.; Snaith, H. J., The Emergence of Perovskite Solar Cells. *Nat. Photonics* **2014,** *8*, 506-514.

33. Sestu, N.; Cadelano, M.; Sarritzu, V.; Chen, F.; Marongiu, D.; Piras, R.; Mainas, M.; Quochi, F.; Saba, M.; Mura, A.; Bongiovanni, G., Absorption F-Sum Rule for the Exciton Binding Energy in Methylammonium Lead Halide Perovskites. *J. Phys. Chem. Lett.* **2015,** *6*, 4566-4572.

34. Frost, J. M.; Butler, K. T.; Brivio, F.; Hendon, C. H.; van Schilfgaarde, M.; Walsh, A., Atomistic Origins of High-Performance in Hybrid Halide Perovskite Solar Cells. *Nano Lett.* **2014,** *14*, 2584-2590.

35. Menéndez-Proupin, E.; Palacios, P.; Wahnón, P.; Conesa, J. C., Self-Consistent Relativistic Band Structure of the CH3NH3PbI3 Perovskite. *Phys. Rev. B* **2014,** *90*, 045207.

36. Saidaminov, M. I.; Abdelhady, A. L.; Murali, B.; Alarousu, E.; Burlakov, V. M.; Peng, W.; Dursun, I.; Wang, L.; He, Y.; Maculan, G.; Goriely, A.; Wu, T.; Mohammed, O. F.; Bakr, O. M., High-Quality Bulk Hybrid Perovskite Single Crystals Within Minutes by Inverse Temperature Crystallization. *Nat. Commun.* **2015,** *6*, 7586.

37. Shi, D.; Adinolfi, V.; Comin, R.; Yuan, M.; Alarousu, E.; Buin, A.; Chen, Y.; Hoogland, S.; Rothenberger, A.; Katsiev, K.; Losovyj, Y.; Zhang, X.; Dowben, P. A.; Mohammed, O. F.; Sargent, E. H.; Bakr, O. M., Low Trap-State Density and Long Carrier Diffusion in Organolead Trihalide Perovskite Single Crystals. *Science* **2015,** *347*, 519-522.

38. Lian, Z.; Yan, Q.; Gao, T.; Ding, J.; Lv, Q.; Ning, C.; Li, Q.; Sun, J.-l., Perovskite CH3NH3PbI3(Cl) Single Crystals: Rapid Solution Growth, Unparalleled Crystalline Quality, and Low Trap Density toward 108 cm–3. *J. Am. Chem. Soc.* **2016,** *138*, 9409-9412.

39. Motta, C.; El-Mellouhi, F.; Sanvito, S., Charge Carrier Mobility in Hybrid Halide Perovskites. *Sci. Rep.* **2015,** *5*, 12746.

40. Galkowski, K.; Mitioglu, A.; Miyata, A.; Plochocka, P.; Portugall, O.; Eperon, G. E.; Wang, J. T.-W.; Stergiopoulos, T.; Stranks, S. D.; Snaith, H. J.; Nicholas, R. J., Determination of the Exciton Binding Energy and Effective Masses for Methylammonium and Formamidinium Lead Tri-Halide Perovskite Semiconductors. *Energy Environ. Sci.* **2016,** *9*, 962-970.

41. Leguy, A. M. A.; Frost, J. M.; McMahon, A. P.; Sakai, V. G.; Kockelmann, W.; Law, C.; Li, X.; Foglia, F.; Walsh, A.; O'Regan, B. C.; Nelson, J.; Cabral, J. T.; Barnes,

P. R. F., The Dynamics of Methylammonium Ions in Hybrid Organic–Inorganic Perovskite Solar Cells. *Nat. Commun.* **2015,** *6*, 7124.

42. Zhu, H.; Miyata, K.; Fu, Y.; Wang, J.; Joshi, P. P.; Niesner, D.; Williams, K. W.; Jin, S.; Zhu, X.-Y., Screening in Crystalline Liquids Protects Energetic Carriers in Hybrid Perovskites. *Science* **2016,** *353*, 1409-1413.

43. Buin, A.; Pietsch, P.; Xu, J.; Voznyy, O.; Ip, A. H.; Comin, R.; Sargent, E. H., Materials Processing Routes to Trap-Free Halide Perovskites. *Nano Lett.* **2014,** *14*, 6281-6286.

44. Walsh, A.; Scanlon, D. O.; Chen, S.; Gong, X. G.; Wei, S.-H., Self-Regulation Mechanism for Charged Point Defects in Hybrid Halide Perovskites. *Angew. Chem., Int. Ed.* **2015,** *54*, 1791-1794.

45. Yin, W.-J.; Shi, T.; Yan, Y., Unusual Defect Physics in CH3NH3PbI3 Perovskite Solar Cell Absorber. *Appl. Phys. Lett.* **2014,** *104*, 063903.

46. Ming, W.; Chen, S.; Du, M.-H., Chemical Instability Leads to Unusual Chemical-Potential-Independent Defect Formation and Diffusion in Perovskite Solar Cell Material CH3NH3PbI3. *J. Mater. Chem. A* **2016,** *4*, 16975-16981.

47. Yang, J.-H.; Yin, W.-J.; Park, J.-S.; Wei, S.-H., Self-Regulation of Charged Defect Compensation and Formation Energy Pinning in Semiconductors. *Sci. Rep.* **2015,** *5*, 16977.

48. Wang, Q.; Shao, Y.; Xie, H.; Lyu, L.; Liu, X.; Gao, Y.; Huang, J., Qualifying Composition Dependent P and N Self-Doping in CH3NH3PbI3. *Appl. Phys. Lett.* **2014,** *105*, 163508.

49. Yu, H.; Lu, H.; Xie, F.; Zhou, S.; Zhao, N., Native Defect-Induced Hysteresis Behavior in Organolead Iodide Perovskite Solar Cells. *Adv. Funct. Mater.* **2016,** *26*, 1411-1419.

50. Agiorgousis, M. L.; Sun, Y.-Y.; Zeng, H.; Zhang, S., Strong Covalency-Induced Recombination Centers in Perovskite Solar Cell Material CH3NH3PbI3. *J. Am. Chem. Soc.* **2014,** *136*, 14570-14575.

51. Azpiroz, J. M.; Mosconi, E.; Bisquert, J.; De Angelis, F., Defect Migration in Methylammonium Lead Iodide and its Role in Perovskite Solar Cell Operation. *Energy Environ. Sci.* **2015,** *8*, 2118-2127.

52. Eames, C.; Frost, J. M.; Barnes, P. R. F.; O'Regan, B. C.; Walsh, A.; Islam, M. S., Ionic Transport in Hybrid Lead Iodide Perovskite Solar Cells. *Nat. Commun.* **2015,** *6*, 7497.

53. Han, Y.; Meyer, S.; Dkhissi, Y.; Weber, K.; Pringle, J. M.; Bach, U.; Spiccia, L.; Cheng, Y.-B., Degradation Observations of Encapsulated Planar CH3NH3PbI3

Perovskite Solar Cells at High Temperatures and Humidity. *J. Mater. Chem. A* **2015,** *3*, 8139-8147.

54. Habisreutinger, S. N.; Leijtens, T.; Eperon, G. E.; Stranks, S. D.; Nicholas, R. J.; Snaith, H. J., Carbon Nanotube/Polymer Composites as a Highly Stable Hole Collection Layer in Perovskite Solar Cells. *Nano Lett.* **2014,** *14*, 5561-5568.

55. Yuan, Y.; Wang, Q.; Shao, Y.; Lu, H.; Li, T.; Gruverman, A.; Huang, J., Electric-Field-Driven Reversible Conversion Between Methylammonium Lead Triiodide Perovskites and Lead Iodide at Elevated Temperatures. *Adv. Energy Mater.* **2016,** *6*, 1501803.

56. deQuilettes, D. W.; Zhang, W.; Burlakov, V. M.; Graham, D. J.; Leijtens, T.; Osherov, A.; Bulović, V.; Snaith, H. J.; Ginger, D. S.; Stranks, S. D., Photo-Induced Halide Redistribution in Organic–Inorganic Perovskite Films. *Nat. Commun.* **2016,** *7*, 11683.

57. Kim, H.-S.; Lee, C.-R.; Im, J.-H.; Lee, K.-B.; Moehl, T.; Marchioro, A.; Moon, S.-J.; Humphry-Baker, R.; Yum, J.-H.; Moser, J. E.; Grätzel, M.; Park, N.-G., Lead Iodide Perovskite Sensitized All-Solid-State Submicron Thin Film Mesoscopic Solar Cell with Efficiency Exceeding 9%. *Sci. Rep.* **2012,** *2*, 591.

58. You, J.; Hong, Z.; Yang, Y.; Chen, Q.; Cai, M.; Song, T.-B.; Chen, C.-C.; Lu, S.; Liu, Y.; Zhou, H.; Yang, Y., Low-Temperature Solution-Processed Perovskite Solar Cells with High Efficiency and Flexibility. *ACS Nano* **2014,** *8*, 1674-1680.

59. You, J.; Meng, L.; Song, T.-B.; Guo, T.-F.; Yang, Y.; Chang, W.-H.; Hong, Z.; Chen, H.; Zhou, H.; Chen, Q.; Liu, Y.; De Marco, N.; Yang, Y., Improved Air Stability of Perovskite Solar Cells via Solution-Processed Metal Oxide Transport Layers. *Nat. Nanotechnol.* **2016,** *11*, 75-81.

60. Guo, Y.; Liu, C.; Inoue, K.; Harano, K.; Tanaka, H.; Nakamura, E., Enhancement in the Efficiency of an Organic-Inorganic Hybrid Solar Cell with a Doped P3HT Hole-Transporting Layer on a Void-Free Perovskite Active Layer. *J. Mater. Chem. A* **2014,** *2*, 13827-13830.

61. Wojciechowski, K.; Leijtens, T.; Siprova, S.; Schlueter, C.; Hörantner, M. T.; Wang, J. T.-W.; Li, C.-Z.; Jen, A. K. Y.; Lee, T.-L.; Snaith, H. J., C60 as an Efficient n-Type Compact Layer in Perovskite Solar Cells. *J. Phys. Chem. Lett.* **2015,** *6*, 2399-2405.

62. Kaltenbrunner, M.; Adam, G.; Glowacki, E. D.; Drack, M.; Schwodiauer, R.; Leonat, L.; Apaydin, D. H.; Groiss, H.; Scharber, M. C.; White, M. S.; Sariciftci, N. S.; Bauer, S., Flexible High Power-Per-Weight Perovskite Solar Cells with Chromium Oxide-Metal Contacts for Improved Stability in Air. *Nat. Mater.* **2015,** *14*, 1032-1039.

63. Ke, W.; Fang, G.; Wan, J.; Tao, H.; Liu, Q.; Xiong, L.; Qin, P.; Wang, J.; Lei, H.; Yang, G.; Qin, M.; Zhao, X.; Yan, Y., Efficient Hole-Blocking Layer-Free Planar Halide Perovskite Thin-Film Solar Cells. *Nat. Commun.* **2015,** *6*, 6700.

64. Li, Y.; Ye, S.; Sun, W.; Yan, W.; Li, Y.; Bian, Z.; Liu, Z.; Wang, S.; Huang, C., Hole-Conductor-Free Planar Perovskite Solar Cells with 16.0% Efficiency. *J. Mater. Chem. A* **2015,** *3*, 18389-18394.

65. Eperon, G. E.; Burlakov, V. M.; Docampo, P.; Goriely, A.; Snaith, H. J., Morphological Control for High Performance, Solution-Processed Planar Heterojunction Perovskite Solar Cells. *Adv. Funct. Mater.* **2014,** *24*, 151-157.

66. Zhou, Y.; Game, O. S.; Pang, S.; Padture, N. P., Microstructures of Organometal Trihalide Perovskites for Solar Cells: Their Evolution from Solutions and Characterization. *J. Phys. Chem. Lett.* **2015,** *6*, 4827-4839.

67. Xiao, M.; Huang, F.; Huang, W.; Dkhissi, Y.; Zhu, Y.; Etheridge, J.; Gray-Weale, A.; Bach, U.; Cheng, Y.-B.; Spiccia, L., A Fast Deposition-Crystallization Procedure for Highly Efficient Lead Iodide Perovskite Thin-Film Solar Cells. *Angew. Chem.* **2014,** *126*, 10056-10061.

68. Jeon, N. J.; Noh, J. H.; Kim, Y. C.; Yang, W. S.; Ryu, S.; Seok, S. I., Solvent Engineering for High-Performance Inorganic–Organic Hybrid Perovskite Solar Cells. *Nat. Mater.* **2014,** *13*, 897-903.

69. Zheng, Y. C.; Yang, S.; Chen, X.; Chen, Y.; Hou, Y.; Yang, H. G., Thermal-Induced Volmer–Weber Growth Behavior for Planar Heterojunction Perovskites Solar Cells. *Chem. Mater.* **2015,** *27*, 5116-5121.

70. Nie, W.; Tsai, H.; Asadpour, R.; Blancon, J.-C.; Neukirch, A. J.; Gupta, G.; Crochet, J. J.; Chhowalla, M.; Tretiak, S.; Alam, M. A.; Wang, H.-L.; Mohite, A. D., High-Efficiency Solution-Processed Perovskite Solar Cells with Millimeter-Scale Grains. *Science* **2015,** *347*, 522-525.

71. Patel, J. B.; Milot, R. L.; Wright, A. D.; Herz, L. M.; Johnston, M. B., Formation Dynamics of CH3NH3PbI3 Perovskite Following Two-Step Layer Deposition. *J. Phys. Chem. Lett.* **2016,** *7*, 96-102.

72. Burschka, J.; Pellet, N.; Moon, S.-J.; Humphry-Baker, R.; Gao, P.; Nazeeruddin, M. K.; Gratzel, M., Sequential Deposition as a Route to High-Performance Perovskite-Sensitized Solar Cells. *Nature* **2013,** *499*, 316-319.

73. Chen, Q.; Zhou, H.; Hong, Z.; Luo, S.; Duan, H.-S.; Wang, H.-H.; Liu, Y.; Li, G.; Yang, Y., Planar Heterojunction Perovskite Solar Cells via Vapor-Assisted Solution Process. *J. Am. Chem. Soc.* **2014,** *136*, 622-625.

74. Xiao, Z.; Dong, Q.; Bi, C.; Shao, Y.; Yuan, Y.; Huang, J., Solvent Annealing of Perovskite-Induced Crystal Growth for Photovoltaic-Device Efficiency Enhancement. *Adv. Mater.* **2014,** *26*, 6503-6509.

75. Zhao, T.; Williams, S. T.; Chueh, C.-C.; deQuilettes, D. W.; Liang, P.-W.; Ginger, D. S.; Jen, A. K. Y., Design Rules for the Broad Application of Fast (<1 s) Methylamine

Vapor Based, Hybrid Perovskite Post Deposition Treatments. *RSC Adv.* **2016,** *6*, 27475-27484.

76. Zhou, Z.; Wang, Z.; Zhou, Y.; Pang, S.; Wang, D.; Xu, H.; Liu, Z.; Padture, N. P.; Cui, G., Methylamine-Gas-Induced Defect-Healing Behavior of CH3NH3PbI3 Thin Films for Perovskite Solar Cells. *Angew. Chem., Int. Ed.* **2015,** *54*, 9705-9709.

77. Saliba, M.; Matsui, T.; Seo, J.-Y.; Domanski, K.; Correa-Baena, J.-P.; Nazeeruddin, M. K.; Zakeeruddin, S. M.; Tress, W.; Abate, A.; Hagfeldt, A.; Gratzel, M., Cesium-Containing Triple Cation Perovskite Solar Cells: Improved Stability, Reproducibility and High Efficiency. *Energy Environ. Sci.* **2016,** *9*, 1989-1997.

78. Burst, J. M.; Duenow, J. N.; Albin, D. S.; Colegrove, E.; Reese, M. O.; Aguiar, J. A.; Jiang, C. S.; Patel, M. K.; Al-Jassim, M. M.; Kuciauskas, D.; Swain, S.; Ablekim, T.; Lynn, K. G.; Metzger, W. K., CdTe Solar Cells With Open-Circuit Voltage Breaking the 1 V Barrier. *Nat. Energy* **2016,** *1*, 16015.

79. Snaith, H. J.; Abate, A.; Ball, J. M.; Eperon, G. E.; Leijtens, T.; Noel, N. K.; Stranks, S. D.; Wang, J. T.-W.; Wojciechowski, K.; Zhang, W., Anomalous Hysteresis in Perovskite Solar Cells. *J. Phys. Chem. Lett.* **2014,** *5*, 1511-1515.

80. Gottesman, R.; Haltzi, E.; Gouda, L.; Tirosh, S.; Bouhadana, Y.; Zaban, A.; Mosconi, E.; De Angelis, F., Extremely Slow Photoconductivity Response of CH3NH3PbI3 Perovskites Suggesting Structural Changes under Working Conditions. *J. Phys. Chem. Lett.* **2014,** *5*, 2662-2669.

81. Shao, Y.; Xiao, Z.; Bi, C.; Yuan, Y.; Huang, J., Origin and Elimination of Photocurrent Hysteresis by Fullerene Passivation in CH3NH3PbI3 Planar Heterojunction Solar Cells. *Nat. Commun.* **2014,** *5*, 5784.

82. Xiao, Z.; Yuan, Y.; Shao, Y.; Wang, Q.; Dong, Q.; Bi, C.; Sharma, P.; Gruverman, A.; Huang, J., Giant Switchable Photovoltaic Effect in Organometal Trihalide Perovskite Devices. *Nat. Mater.* **2014,** *14*, 193-198.

83. Bertoluzzi, L.; Sanchez, R. S.; Liu, L.; Lee, J.-W.; Mas-Marza, E.; Han, H.; Park, N.-G.; Mora-Sero, I.; Bisquert, J., Cooperative Kinetics of Depolarization in CH3NH3PbI3 Perovskite Solar Cells. *Energy Environ. Sci.* **2015,** *8*, 910-915.

84. Xu, J.; Buin, A.; Ip, A. H.; Li, W.; Voznyy, O.; Comin, R.; Yuan, M.; Jeon, S.; Ning, Z.; McDowell, J. J.; Kanjanaboos, P.; Sun, J.-P.; Lan, X.; Quan, L. N.; Kim, D. H.; Hill, I. G.; Maksymovych, P.; Sargent, E. H., Perovskite–Fullerene Hybrid Materials Suppress Hysteresis in Planar Diodes. *Nat. Commun.* **2015,** *6*, 7081.

85. Noel, N. K.; Abate, A.; Stranks, S. D.; Parrott, E. S.; Burlakov, V. M.; Goriely, A.; Snaith, H. J., Enhanced Photoluminescence and Solar Cell Performance via Lewis Base Passivation of Organic–Inorganic Lead Halide Perovskites. *ACS Nano* **2014,** *8*, 9815-9821.

86. Leijtens, T.; Hoke, E. T.; Grancini, G.; Slotcavage, D. J.; Eperon, G. E.; Ball, J. M.; De Bastiani, M.; Bowring, A. R.; Martino, N.; Wojciechowski, K.; McGehee, M. D.; Snaith, H. J.; Petrozza, A., Mapping Electric Field-Induced Switchable Poling and Structural Degradation in Hybrid Lead Halide Perovskite Thin Films. *Adv. Energy Mater.* **2015,** *5*, 1500962.

87. Deng, Y.; Xiao, Z.; Huang, J., Light-Induced Self-Poling Effect on Organometal Trihalide Perovskite Solar Cells for Increased Device Efficiency and Stability. *Adv. Energy Mater.* **2015,** *5*, 1500721.

88. Shao, Y.; Fang, Y.; Li, T.; Wang, Q.; Dong, Q.; Deng, Y.; Yuan, Y.; Wei, H.; Wang, M.; Gruverman, A.; Shield, J.; Huang, J., Grain Boundary Dominated Ion Migration in Polycrystalline Organic-Inorganic Halide Perovskite Films. *Energy Environ. Sci.* **2016,** *9*, 1752-1759.

89. Fu, X.; Jacobs, D. A.; Beck, F. J.; Duong, T.; Shen, H.; Catchpole, K. R.; White, T. P., Photoluminescence Study of Time- and Spatial-Dependent Light Induced Trap De-Activation in CH3NH3PbI3 Perovskite Films. *Phys. Chem. Chem. Phys.* **2016,** *18*, 22557-22564.

90. Galisteo-López, J. F.; Anaya, M.; Calvo, M. E.; Míguez, H., Environmental Effects on the Photophysics of Organic–Inorganic Halide Perovskites. *J. Phys. Chem. Lett.* **2015,** *6*, 2200-2205.

91. Tian, Y.; Peter, M.; Unger, E.; Abdellah, M.; Zheng, K.; Pullerits, T.; Yartsev, A.; Sundstrom, V.; Scheblykin, I. G., Mechanistic Insights into Perovskite Photoluminescence Enhancement: Light Curing with Oxygen can Boost Yield Thousandfold. *Phys. Chem. Chem. Phys.* **2015,** *17*, 24978-24987.

92. Leijtens, T.; Srimath Kandada, A. R.; Eperon, G. E.; Grancini, G.; D'Innocenzo, V.; Ball, J. M.; Stranks, S. D.; Snaith, H. J.; Petrozza, A., Modulating the Electron–Hole Interaction in a Hybrid Lead Halide Perovskite with an Electric Field. *J. Am. Chem. Soc.* **2015,** *137*, 15451-15459.

93. Park, N.-G., Perovskite Solar Cells: an Emerging Photovoltaic Technology. *Mater. Today* **2015,** *18*, 65-72.

94. Song, Z.; Watthage, S. C.; Phillips, A. B.; Heben, M. J., Pathways Toward High-Performance Perovskite Solar Cells: Review of Recent Advances in Organo-Metal Halide Perovskites for Photovoltaic Applications. *J. Photonics Energy* **2016,** *6*, 022001-022001.

95. Song, T.-B.; Chen, Q.; Zhou, H.; Jiang, C.; Wang, H.-H.; Yang, Y.; Liu, Y.; You, J.; Yang, Y., Perovskite Solar Cells: Film Formation and Properties. *J. Mater. Chem. A* **2015,** *3*, 9032-9050.

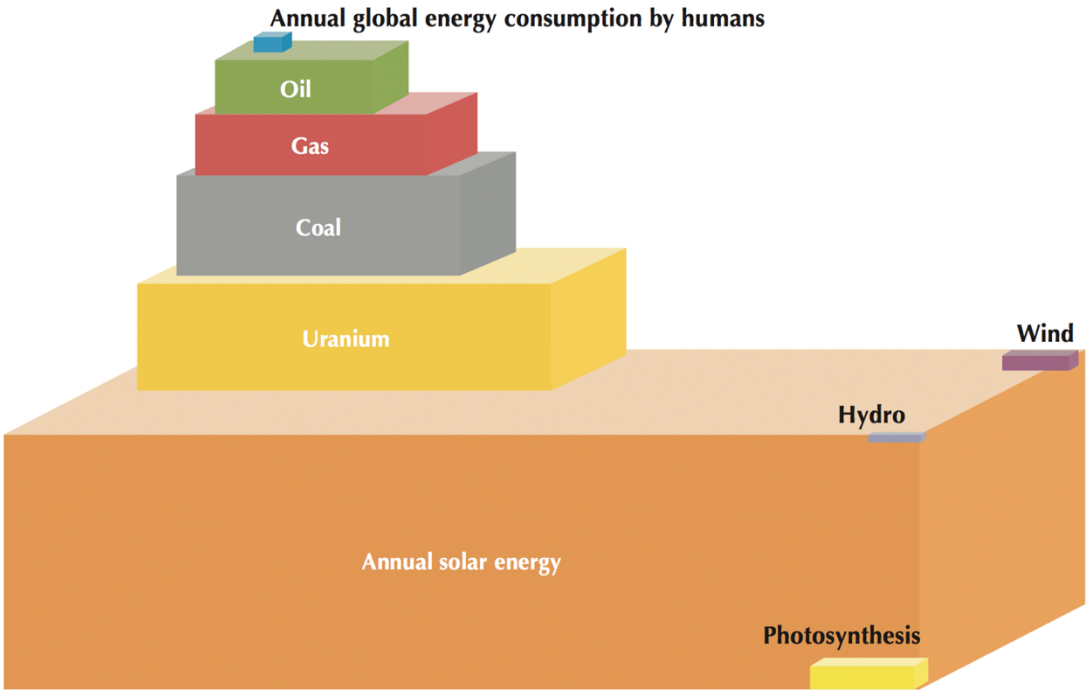

Figure 1.1. Schematic representing the total theoretical annual energy potential by resource compared to the global annual energy consumption (blue box at the top).[4] It is clear that solar energy is the largest source of energy on the planet by a large margin. (Reproduced with permission from © OECD/IEA 2008 Energy Technology Perspectives, IEA Publishing. License: www.iea.org/t&c, and National Petroleum Council, 2007, after Craig, Cunningham and Saigo)

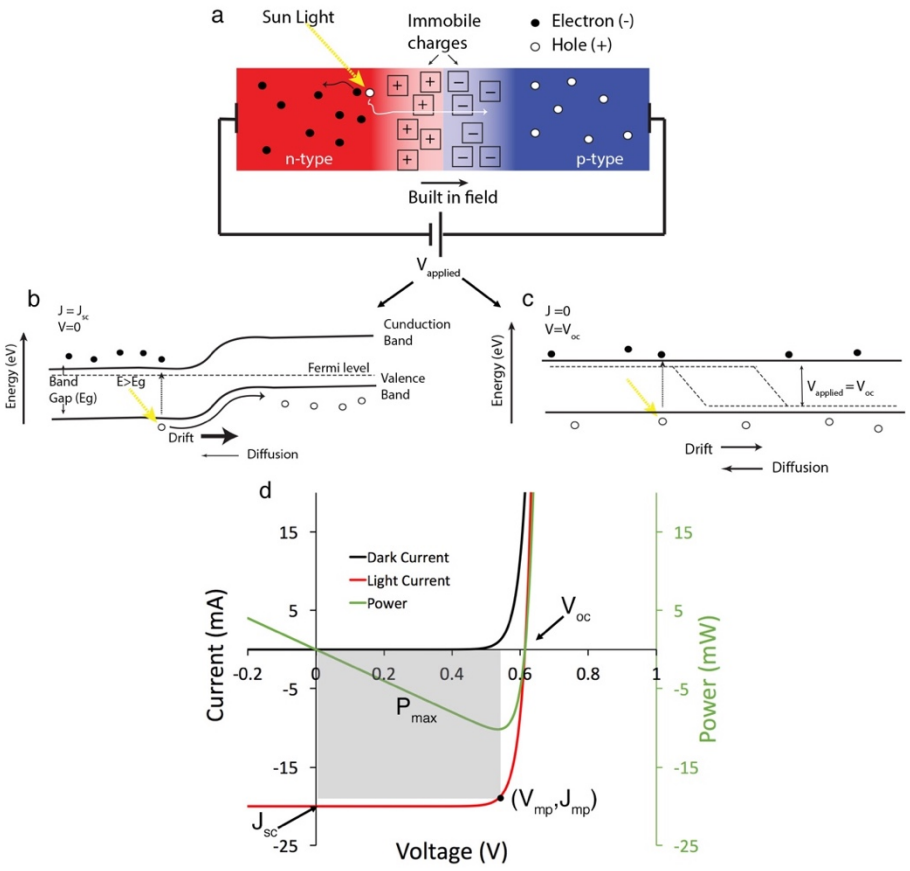

Figure 1.2. Photovoltaic working principles. a) Schematic of a general p-n junction. The positive p-type material is on the right and the negative n-type material on the left. The junction creates an internal electric field at the interface. Sunlight is absorbed in the semiconductor to create an electron and hole. The charges then separate at the junction due to drift through the internal field. Energy diagrams of a p-n junction with the material held at short circuit, b), or open circuit, c), conditions. d) JV curve of a general p-n junction in the dark (black) and under illumination (red). Important solar cell parameters are highlighted on the light current curve. The extracted power (green) is plotted as well. The grey box shows the maximum power area that defines the maximum power point, which is used to calculate the fill factor.

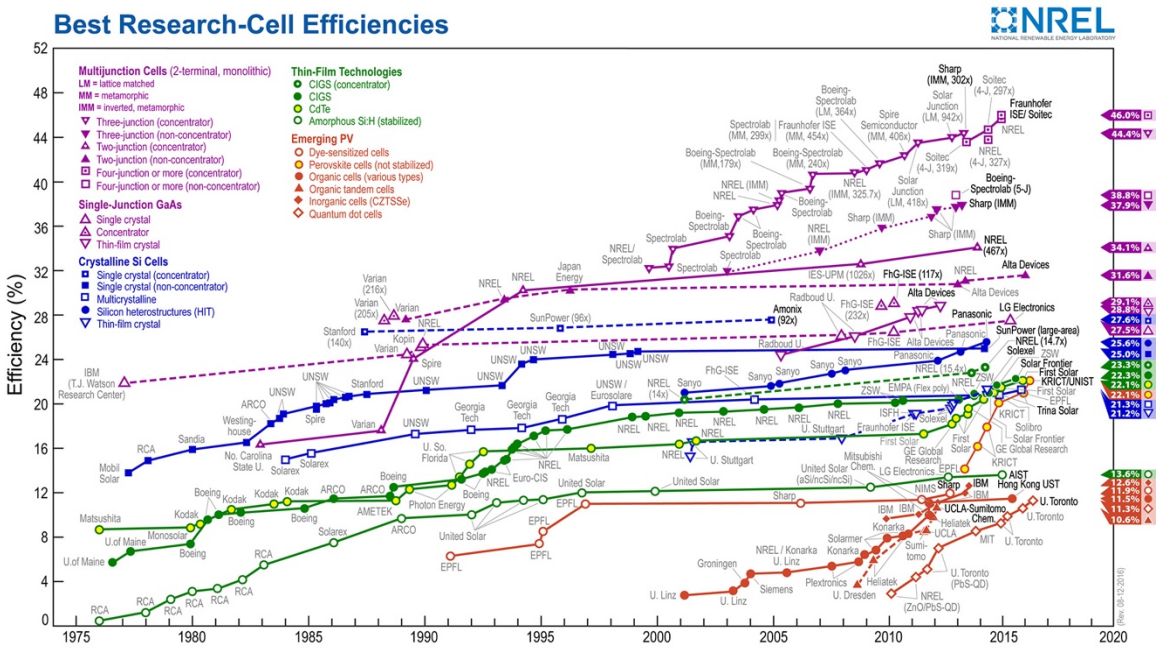

Figure 1.3. Graph of the highest certified research-cell efficiencies for all PV technologies since 1976.[15] Perovskite-based devices are represented by yellow-filled orange circles. (Best Research-Cell Efficiencies" is reprinted with permission by the National Renewable Energy Laboratory, http://www.nrel.gov/ncpv/images/efficiency_chart.jpg, Accessed October 26, 2016.)

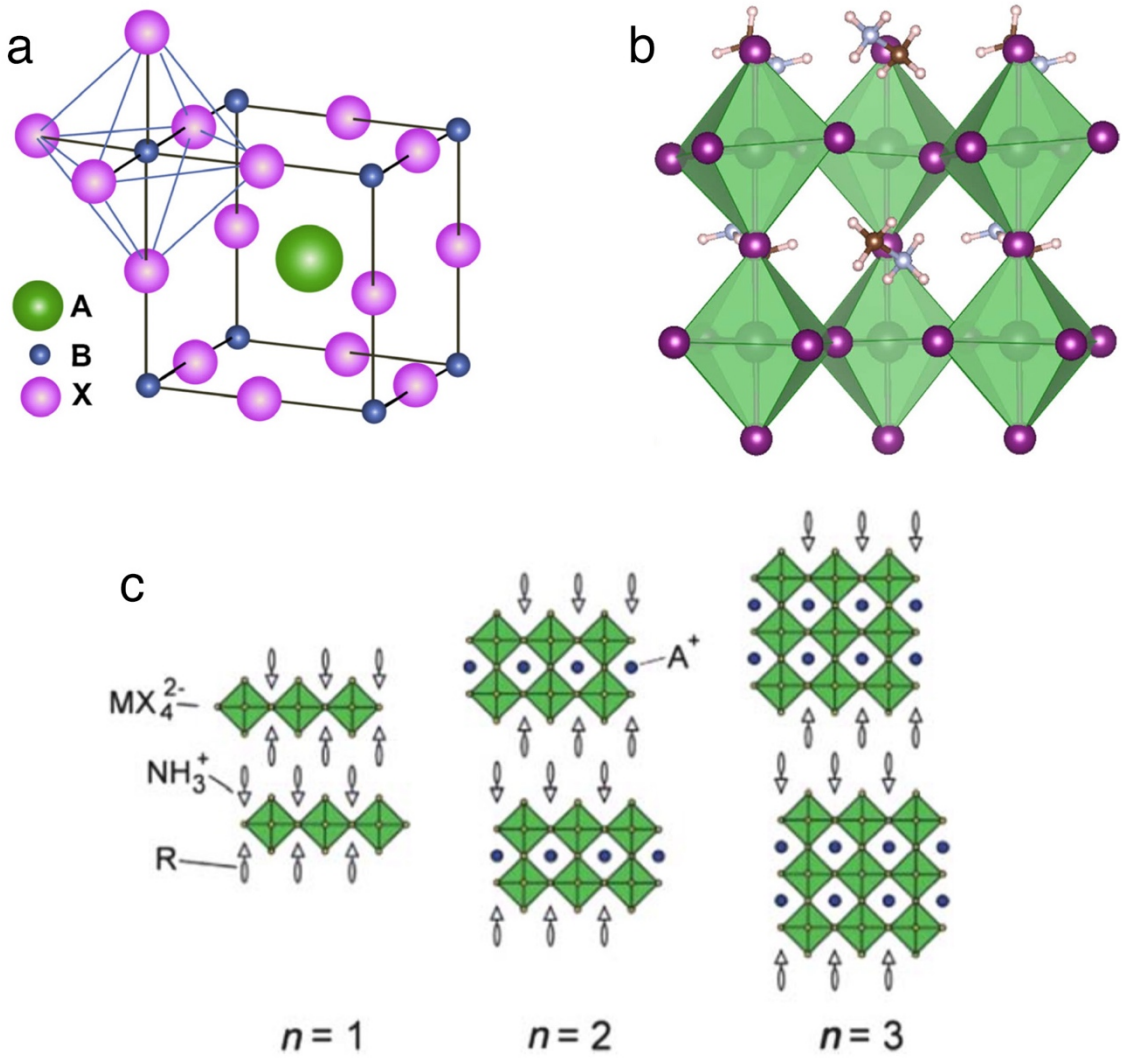

Figure 1.4. Perovskite crystal structure. a) General ABX_3 perovskite crystal structure.[93] (Reproduced in part from Ref 93 with permission of Elsevier) b) Tetragonal [110] $MAPbI_3$ in its relaxed state.[39] (Reproduced in part from Ref 39 with permission from Nature Publishing Group.) c) Formation of 2-D and mixed A-site cation Ruddlesden-Popper perovskite phase with substitution of a long alkylammonium ion.[29] (Reproduced in part from Ref 29 with permission of The Royal Society of Chemistry.)

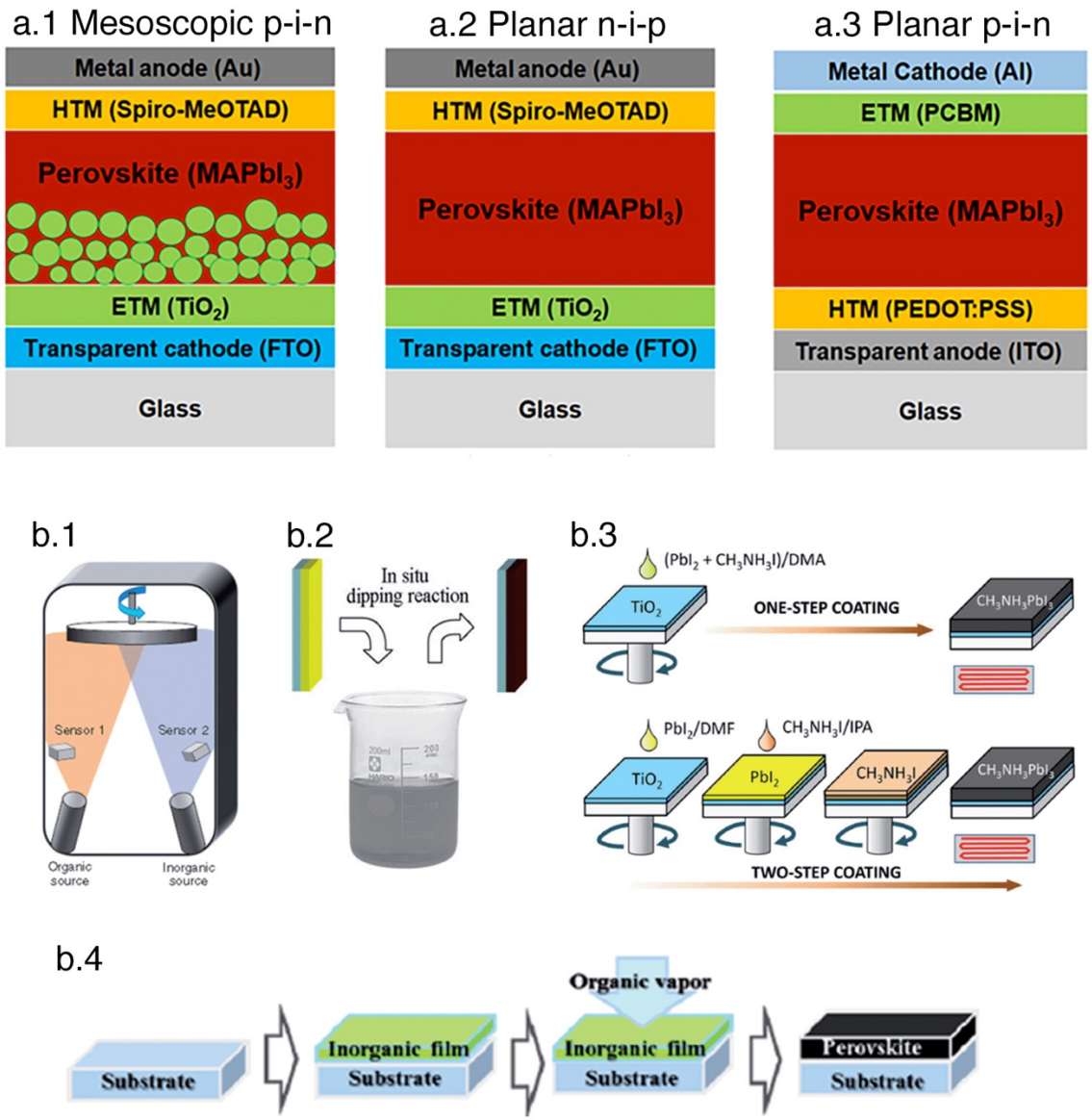

Figure 1.5. $MAPbI_3$ device architecture and fabrication techniques. a) Schematics of the major $MAPbI_3$ solar cell architecture: a1) mesoscopic n-i-p a2) planar n-i-p, a3) planar p-i-n.[94] (Reproduced in part from Ref 94 with permission of SPIE.) b) Schematic of the different deposition techniques of $MAPbI_3$: b1) evaporation, b2) 2-step solution conversion, b3) solution spin coating techniques for one and two step deposition, b4) 2-step vapor phase conversion.[95] (Reproduced in part from Ref 95 with permission of The Royal Society of Chemistry.)

CHAPTER 2

VOLTAGE-INDUCED TRANSIENTS IN METHYLAMMONIUM LEAD TRIIODIDE PROBED BY DYNAMIC PHOTOLUMINESCENCE SPECTROSCOPY

2.1 Motivation

The slow transient optoelectronic responses (STOR) of $MAPbI_3$ are severely limiting the potential of perovskite photovoltaics.[1] The effects of STOR have been documented in the form of hysteresis of illuminated current-voltage scans,[2-4] transients in photoconductivity,[4-6] effects in frequency-dependent measurements,[4, 7-9] illumination-dependent dielectric constant,[10] and a switchable photovoltaic effects.[11-13] The slow transient responses lead to rate-dependent results making it difficult to reliably report device efficiencies, repeat findings, and may also be related to performance decay over time even in inert environments.[6] Until the underlying mechanisms of these behaviors are fully understood, further device optimization will be a challenge. Theoretical and experimental results point to two leading hypotheses for the mechanism of these slow transient effects: 1) ion migration of charged shallow defects leading to native defect doping or build-up of space charge,[6, 11, 14-17] or 2) charge trapping in interfacial electronic defects.[2, 8] Previous studies have suggested that ferroelectric effects from methylammonium (MA^+) dipole alignment or lattice distortion may be an additional

factor,[4-5, 9, 18-21] but recent work has discounted long range ferroelectric effects at room temperature as a source of the slow transient response.[22-25] A majority of the experimental evidence supporting these leading theories come from electrical characterization methods on optimized PV devices, or in specific test structures designed to investigate a finding or hypothesis from an optimized PV device, but most experiments are not able to differentiate between the different mechanisms or account for multiple mechanisms occurring simultaneously. Furthermore, the strong sensitivities of $MAPbI_3$ thin film properties to a number of factors, including morphology,[26-29] fabrication conditions,[30-33] and testing environment[34-37] make it nearly impossible to compare results from different experiments. Therefore, it remains an open question whether the slow transient response arises from a single dominant mechanism in all samples, or whether different subsets of several mechanisms are active in any given type of sample or device structure. Clearly development of new and more universal testing platforms is necessary to deepen our understanding of this material system.

Photoluminescence (PL) is a powerful tool that has been essential to our current understanding of hybrid perovskite materials, elucidating properties such as chemical composition,[9, 38-39] nanomorphology,[29] lattice structure,[40] interfacial charge transfer,[8, 41-43] environmental sensitivity,[34-36] and charge carrier dynamics.[44-47] In most of these prior studies, the PL response was measured without electrical bias from films on glass, from partial device stacks without top contacts, or from complete device stacks through the transparent electrode in the open circuit state, meaning the measurements were all under steady state conditions. A few noted exceptions have measured the PL response under bias,[11, 24, 48] but still at steady state conditions. Based on the intrinsic sensitivity of the PL

response to the material's electronic, compositional, and structural state, time-resolved PL on the time scale of the electrical slow transients will be a valuable technique to gain insight to the mechanisms behind the slow transient effects. In this work, a lateral interdigitated electrode (IDE) device coupled with dynamic PL spectroscopy and microscopy as a platform was used to investigate the slow transient response to a step change in applied bias. We observed electric field-dependent slow transient optical responses in the forms of spatially and spectrally resolved PL quenching coupled with slow current transients. Analysis of these PL transient responses was capable of distinguishing between two simultaneous and independent phenomena; one reversible and the other irreversible within the experimental time scales. Direct correlation of the optical and electrical transient responses indicates that the observed reversible response is a result of charge trapping where as the irreversible response arises from defect ion migration under nominal electric fields.

2.2 Experimental Methods

2.2.1 Material synthesis

Methylammonium iodide (MAI) was synthesized by reacting methylamine (40 wt. % in water) with equimolar amounts of HI (57 wt. % in water) in ambient atmosphere at 0 ˚C for 2 h. The solution was dried in a roto-evaporator at 75 ˚C. The precipitate was washed three times with diethylether and dried at 50 ˚C in a vacuum oven. PbI_2 (99.9985% metals basis) was obtained from Alfa Aesar and used as received. The $MAPbI_3$ precursor solution was made by dissolving 1:3 PbI_2 and MAI in DMF at 60 ˚C overnight.

2.2.2 Device fabrication

The interdigitated gold electrodes on borofloat glass were provided by Vaporsens. The electrodes were cleaned by 30-s sonication in acetone, methanol, and isopropyl alcohol, respectively, followed by UV-ozone cleaning for 15 min. Clean electrodes were transferred to the spin coater under ambient conditions. The IDE surface was soaked with a drop of the $MAPbI_3$ precursor solution for 30 s before spinning at 4000 rpm for 15 s. The devices were immediately transferred to a hot plate and annealed at 120 ˚C for 30 min. The completed devices were then stored in a vacuum desiccator in the dark for at least 12 h before testing.

2.2.3 Device characterization

X-ray diffraction (XRD) was performed on the $MAPbI_3$ coated IDE in ambient atmosphere using a Panalytical X'Pert X-Ray Diffractometer. Current voltage sweeps were performed under a low flow of argon with a Keithley 236 source measure unit. The san rates for both dark and light measurements were 5 Vs^{-1}.

2.2.4 Dynamic photoluminescence spectroscopy

The devices were transferred to a custom designed chamber and placed on a Leica DMI4000 fluorescence microscope. The chamber was purged with a low flow of argon for 15 min in the dark followed by a 15-min light soak. A mercury lamp supplied the excitation light through a long pass optical filter to deliver 0.9 mW/cm^2 of 560 nm peak light through the bottom objective. The emitted light from the device was directed to either a high resolution charge-coupled device (CCD) camera for imaging or a Princeton

Instruments Acton PIXIS:400B spectrophotometer for spectroscopy. Voltage was applied by an external power supply by pulsing between short circuit (0V) and the desired bias level. The negative bias, the leads connecting to the device were switched. Current was measured three times per second by monitoring the voltage change across a 10 kΩ resistor using a SigZig data logger from Vaporsens.

For the spectroscopy studies, a single device was used for all experiments unless otherwise noted. Between each experiment, the analysis spot was moved to a new region followed by light soaking for 15 min before measurement. Thus, while the entire IDE experienced every applied voltage, the light excitation was limited to a different area for each experiment to maintain a common initial state across all measurements. The order of experiments was repeat followed by switch at the same voltage magnitude. The applied biases started with 1 V and increased to 20 V for each experiment. The PL was measured for 30 s to establish a baseline PL before any voltage was applied. The PL intensity from each recorded spectra was calculated by finding the peak maximum; therefore, any peak shifting was accounted for. Full spectra were recorded every 0.5 s and the PL intensity was calculated from the peak maximum at each spectrum.

A separate device, fabricated following identical procedures, was used for dynamic PL imaging results. The exposure time for each frame was 6 s. A minimum of four frames were recorded to show the PL stability prior to bias application, the response under bias was measured for 10 frames, and 4 to 5 frames were used to show the recovery after bias removal. A new area was chosen for each voltage magnitude, but the positive and negative measurements at a particular voltage magnitude used the same area. Each new area underwent a 15-min light soak prior to testing. The time between the positive

and negative voltage experiments was between 1 to 2 min.

2.3 Results and Discussion

The multifunctional testing platform used for this study is shown schematically in Figure 2.1a. The test structure consisted of a symmetric gold IDE device with 10 μm wide electrodes and 10 μm electrode gap distances on a glass substrate. $MAPbI_3$ was deposited in a 1-step spin coating technique directly onto the IDE test structure with no buffer layers. The $MAPbI_3$ showed fairly uniform coverage between the gold electrodes, as seen in the optical and SEM images in Figure 2.1b and c, respectively. XRD spectrum of a $MAPbI_3$ coated IDE device is seen in Figure 2.2a and shows successful formation of $MAPbI_3$ with only trace amount of PbI_2. The $MAPbI_3$ exhibited good Ohmic contact with the gold electrodes based on the linear and symmetric I-V curves as seen in Figure 2.2b. The PL responses were measured with an inverted fluorescence microscope equipped with a high-resolution camera and a spectrophotometer. The electrical bias was applied using a power supply with an inline ammeter for simultaneous current measurement. The applied biases used in this study were 1, 5, 10, and 20 V equating to nominal in-plane electric fields ranging from 1-20 $kVcm^{-1}$. Comparatively, planar vertically stacked solar cell devices with a typical maximum power point voltage of 0.75 V across a thickness of up to 500 nm would experience an electric field of 15 $kVcm^{-1}$ or higher. Thus, the applied fields used in this study are relevant to the planar vertically stacked devices. As depicted in Figure 2.1a, green light excitation and PL emission collection occurred through the upward-facing objective with a spot size of $5x10^{-3}$ cm^2. Therefore, excitation of and emission from the $MAPbI_3$ was limited to the material between the electrodes, isolating

the bias dependent response. The IDE device has a small electrode interface area minimizing contribution from electrode interface effects compared to planar vertically stacked devices. The prepatterned electrodes apply a more uniform and controllable electric field across the sample compared to vertically stacked devices, which vary with the $MAPbI_3$ thickness. The electrode symmetry of the IDE device enables reliable studies on the electrode polarity to investigate the reversibility of the responses. Furthermore, the measurements occur across multiple electrode pairs over a relatively large measurement area, which should average out micro-scale nonuniformities in the $MAPbI_3$ morphology for consistent spectroscopy measurements. Finally, the IDE provides a large and redundant sampling area to effectively monitor spatially dependent PL changes relative to the electrode polarity. Thus, this testing platform effectively isolates the intrinsic $MAPbI_3$ response.

Two types of experiments were performed at the four voltages (denoted by V) to fully investigate the reversibility of the responses: 1) *repeat* tests in which the applied voltage was repeatedly cycled between 0 and +V for four cycles, and 2) *switch* tests in which the electrode polarity was switched in the sequence 0, +V, 0, -V for two complete cycles yielding four decays and four recovery responses. The 0 V state indicates a short circuit condition. Figure 2.3a shows spatially averaged PL spectra measured before, during, and after the first application of all biases during the repeat tests. In the absence of bias, a stable PL emission with a sharp single peak centered at 775 nm was observed, which is in good agreement with what is reported in the literature. Upon the application of any bias, quenching of the PL relative to the bias magnitude was observed. When the bias was removed, the PL intensity recovered over time; however, the ultimate degree of

recovery was inversely related to the bias magnitude. Additionally, a slight blue shift of the PL peak (and appearance of a secondary peak at higher energy) was observed after applying 20 V bias, and only partially recovered when the bias was removed.

The dynamic PL response was monitored by tracking the PL intensity maximum of each spectrum to account for any slight shifts in the peak wavelength. The normalized dynamic PL response profiles are displayed in Figure 2.3b and yield several important qualitative observations. Starting with the 1 V experiments, in particular, the repeat test, a slow response was observed as a monotonic decay to a steady state value that was consistent across all cycles and fully recoverable to the initial prebias state. Thus, for a bias of 1 V, the slow transient is considered to be completely reversible. (Note: there is a difference in the relative quenching efficiency and noise level between the 1 V repeat and 1 V switch responses seen in this device and other similar experiments. The source of this variation is unknown and the subject of continued investigation, but it is important to note that the general trend of complete PL recovery after removal of the bias is still observed.) However, for both repeat and switch experiments at voltage magnitudes greater than 1 V, the PL response was dependent on the cycle number. In the first cycle at these larger biases, the response showed an overshoot behavior with fast PL quench to a minimum followed by a slow rise to the steady state value. When the bias was removed, the PL response only partially recovered within the experimental timescales and the magnitude of the recoveries were inversely related to the applied voltage magnitude, as previously highlighted in Figure 2.3a. Therefore, the initial response is considered to be at least partially irreversible. Alternatively, the second and subsequent cycles at these larger biases exhibited behaviors similar to the 1 V experiments with monotonic slow

decays to the steady state established during the first cycle, and were fully recoverable referenced to the beginning of the second cycle. Thus, under larger applied fields, there is clearly a unique interplay between distinctive reversible and irreversible processes.

The decay and recovery transients were quantified by graphical fitting to extract time constants, which are summarized in Figure 2.4. For the first responses of biases greater than 1 V, only the overshoot recovery (rise from the PL minimum to the steady state value) was fit with a single exponential function, and these time constants ($\tau_{PL,ir}$) are presented in the inset of Figure 2.4d. Alternatively, double exponential functions were capable of fitting the complete monotonic decay and recover transients, revealing both fast ($\tau_{1,PL}$) and slow ($\tau_{2,PL}$) responses.

Figure 2.4 reveals a stark difference between the dynamics of decay and recovery and displays both commonalities and distinctions between the repeat and switch experiments. First, Figure 2.4a reveals a negative relation between the $\tau_{1,PL}$ and the applied voltage. The time constants range from 1 s to below 0.5 s. It is noted that the sensor exposure time used in these experiments was 0.5 s, therefore, the calculated time constants are ultimately limited to near 0.5 s and any value well below this limit is an artifact from the graphical fitting procedure. Thus, the $\tau_{1,PL}$ values for the 20 V experiments are likely limited by the instrument response time. The $\tau_{1,PL}$ values also show negligible deviations between cycle-to-cycle and between switch and repeat experiments at a particular voltage (including values above the instrument's response time) suggesting the mechanism is fully reversible upon removal of the bias. This reversibility is supported by the constant and consistent recovery transients across voltage and cycle number for both switch and repeat experiments. In contrast, the slower $\tau_{2,PL}$

decay constants differ significantly between the switch and repeat experiments. For the repeat tests, $\tau_{2,PL}$ also shows a negative correlation with the applied voltage and little cycle-to-cycle deviation, but is an order of magnitude larger than $\tau_{1,PL}$ and well above the sensor exposure time. The negative correlation for $\tau_{2,PL}$ (repeat) was linear on a semi-log scale, implying an exponential dependence, with a slope of -0.11± 0.02. However, in the switch tests, the cycle-to-cycle scatter of $\tau_{2,PL}$ is large and increases both with bias magnitude and in a systematic manner with the cycle number. The systematic increase of the response times after switching the electrode polarity suggests a repeated irreversible process. Despite the differences between the switch and repeat decay behaviors, the $\tau_{2,PL}$ recover transients for both switch and repeat again show a constant and consistent value across voltage and cycle number. This suggests a reversible process, similar to that seen in the repeat experiments, occurs simultaneously with and independently of the proposed irreversible process. To quantify this irreversible process, the $\tau_{PL,ir}$ trend is analyzed. As presented in the inset of Figure 2.4c, the $\tau_{PL,ir}$ values range from 10 to 100 s and also exhibit a negative correlation with the applied voltage. However, the slope on a semi-log scale is best fit to -0.25, differentiating it from the reversible process.

In support of the PL transient responses, the simultaneously recorded dynamic current responses are presented in Figure 2.5. It is important to note that the PL and current transient responses show opposite sign (decrease/increase under bias respectively), and there was no clearly observable slow current transient decay above the noise threshold when the bias was removed, so only the transients in response to the application of a bias were analyzed. As seen in Figure 2.5, there are several qualitative similarities between the current and PL transients. First, the initial response to an applied

bias greater than 1 V exhibited a peak and recover to a steady state value (with exception in the 20 V repeat response, which is discussed later). Subsequent responses in the repeat experiments, as well as all of the 1 V responses, showed only a monotonic rise to the steady state value determined during the first response. Finally, the switch experiments showed systematic response variation upon switching the electrode polarity with biases above 1 V. The major qualitative difference between the current and PL transient responses is that the second switch response for 5 and 10 V biases also showed a peak and recover behavior similar to their first response. The subsequent responses in the switch experiments exhibited a monotonic increase, but not to any common steady state value. The responses were fit using a similar procedure as the PL response fitting: namely, the monotonic transients were fit with a double exponential function ($\tau_{1,I}$ and $\tau_{2,I}$), where as the nonmonotonic responses only fit the recover to steady state using a single exponential function ($\tau_{I,ir}$). Figure 2.5b presents the fitted time constants of the isolated current transients. The $\tau_{1,I}$ values appear to be mostly limited by the ammeter's sample rate (~0.25 s), but the $\tau_{2,I}$ values are well above that limitation with a similar magnitude to the $\tau_{2,PL}$ values (1-10 s for repeat and 10-100s for switch experiments). However, unlike the PL responses, there was no clear voltage dependence in the $\tau_{2,I}$. The only voltage dependence that was observed was for $\tau_{I,ir}$, which shows a similar voltage dependence as the $\tau_{PL,ir}$. It is unclear why there was no voltage dependence for $\tau_{2,I}$, however, we note that, unlike the PL measurements, current was collected from the whole IDE device. Thus, dark current transients outside of the illuminated area (0.16 cm^2) may mask details of behavior within the illuminated region ($5x10^{-3}$ cm^2) and make direct quantitative correlation between the current and PL responses beyond the scope of

this manuscript.

Dynamic PL imaging was used to further investigate the irreversibility and electrode polarity dependent PL responses. The dynamic response was recorded with time-lapse PL images on a separate test structure to monitor the response to 1, 5, 10, and 20 V applied biases. In all experiments, the initial observation directly after application of an applied bias was a fast and uniform decrease in image brightness, which recovered when the bias was removed. However, when biases greater than 1 V were applied, some irreversible, localized PL quenching was observed. The frames of the time-lapse movies of +10 V and -10 V applied biases are presented in Figure 2.6. As seen in the left column of Figure 2.6, the first application of +10 V induced the formation of darker areas near the centers of the interelectrode gaps that grew from the centers towards the negative electrodes. Based on the SEM images in Figure 2.1c, the $MAPbI_3$ grain sizes are on the order of a micron and the observed quenched areas are half of the gap distance wide, 5 μm, and roughly 10 μm long, so this quenched area encompasses several grains. Upon removal of the bias, the growth of the quenched areas stopped but did not disappear with time, signifying a stable state under zero applied bias. As seen in the right column of Figure 2.6, reversing the electrode polarity (-10 V) on the same sample did not reverse the quenching in the areas formed during the +10 V test. Instead, new quenched areas nucleated at the now positive electrode and grew back towards the negative electrodes. Thus, the PL microscopy studies were capable of spatially resolving the reversible (uniform darkening of the PL images) and irreversible (stable quenched areas) PL responses correlating to the spectroscopy studies.

The results presented above highlight the complexity of the optoelectronic

response of $MAPbI_3$ to an applied bias. The distinct reversible and irreversible responses signify that there are clearly multiple processes contributing to the slow transient responses. However, before these slow processes are analyzed, it is important to note the fast carrier dynamics that are expected to contribute to the magnitude of the PL and current response, but cannot be resolved with the techniques used in this study. Under an applied bias, the free photogenerated charge carriers in the $MAPbI_3$ film will be swept out through the electrodes resulting in fast PL quenching and a current spike, the rate of which is limited by the free carrier band-to-band recombination dynamics and drift velocities.[24, 48] In $MAPbI_3$, the free carrier lifetimes have an upper bound on the order of hundreds of nanoseconds[44-46] and the mobilities have a lower bound[49] on the order of 1 $cm^2V^{-1}s^{-1}$ leading to a transient time across the 10 μm gap of about 1 μs. This is clearly too fast to be resolved with the instrument response time (>0.5 s) and are therefore mixed with the $\tau_{1,PL/I}$ time constants. Thus, the full time dependent current and PL responses are broken down into three regions, as depicted in Figure 2.7: region I) steady state with no applied field, region II) fast (ns-μs time scales) free carrier response immediately after the field is applied, and region III) slow (0.5-100 s time scales) transient response under constant applied field. Region III, as discussed above, is further identified as either an irreversible or reversible response. Based on the following analyses, these responses are attributed to ion migration and charge trapping mechanisms, respectively.

The proposed relationship between ion migration and the resulting slow PL and current transients are depicted in Figure 2.7a. In a $MAPbI_3$ system, charged shallow defect ions, such as methylammonium and iodide interstitials (MA_i^+,/I_i^-) or vacancies (V_{MA}^-/V_I^+), are anticipated to have low formation energies[50-51] and low activation barriers

for migration[15-16] leading to potentially high concentrations of mobile ions. It is noted that details concerning defect formation, relative ratios of the various defect ions, and drift mobilities of the defect ions are still under debate and dependent on a number of experimental parameters outside of the scope of this manuscript. Under steady state conditions prior to the application of the field (region I), the distributions of charged defects are expected to be uniform. When bias is applied (region II), charge carriers are swept out through the electrodes and produce a spike in the current and rapid PL quenching. Under continued application of a sufficient bias (V > 1 V) (region III), mobile ions respond by drifting toward their respective electrodes to partially compensate the external field. This field compensation reduces free carrier separation leading to a slight increase in the PL and a decrease in the current. This response is similar to that seen in light emitting electrochemical cells (LEECs), which use mobile molecular ions in a polymer matrix to dynamically adjust the electric field for enhanced charge injection at the electrode interface and radiative recombination in the bulk of the film. In fact, the first current response of the 20 V repeat experiment (double overshoot and recover to steady state) is similar to reported LEEC responses under sufficiently high fields where the buildup of charges decreases the injection barrier leading to an increase in the current.[52] When the external field is removed, the PL recovers, but not to the initial steady state conditions, suggesting that any back diffusion of the mobile ions at room temperature is negligible.

The spatially-resolved dynamic quenching from the PL images in Figure 2.6 further support the irreversible ion migration mechanism as well as provide insight to the active mobile species. When the voltage is first applied (+10 V), the quenching nucleates

at the centers of the electrode gaps, and moves toward the negative electrodes, supporting the hypothesis that the quenching is a result of drifting of a charged species. The areas with the most noticeable changes are highlighted with yellow arrows in Figure 2.6. The fact that the quenching nucleates at the center is important because if the quenching was caused by the build up or depletion of a defect ion, it should start at the electrode interface and grow inward following the concentration profile. Rather, these results suggest that the quenching mechanism is more complex and might involve multiple ions of opposite charge separating to form distinct compositional zones starting at the centers of the electrode gaps. In this case, because the quenched areas grow toward the negative electrodes, the quenching is initiated in areas with high ratios of MA^+/I^- caused from drifting of either MA_i^+ and/or V_I^+ into the area. The stability of the quenched zones when the voltage is removed, and even when the electrode polarity is switched, signifies that the migration of the ions leads to a stable immobile state with decreased PL. Possible explanations for this immobile and stable quenched state include local stabilization of the shallow defect dopants leading to a decrease in the local radiative recombination lifetime, $\tau_{rad,p/n} = (R_{ec}*N_{D/A})^{-1}$, (where R_{ec} is the recombination coefficient and $N_{D/A}$ is the donor/acceptor doping concentration) assuming a constant nonradiative recombination lifetime,[53] local compositional changes leading to transformation of the shallow mobile defects to covalent immobile midgap recombination centers,[54] or compositional instability leading to degradation of the $MAPbI_3$ to PbI_2.[17] In fact, Leijtens et al. high-performance. characterized the growth of PbI_2 in part through the observation of a PL peak near ~600nm, which is attributed to highly defective PbI_2.[17] This is similar to the shoulder peak that appears after the application of a 20 V bias suggesting that a similar

process may be contributing to the irreversible PL quenching. When the electrode polarity is reversed, new quenched areas nucleate at the now positive electrode, and grow toward the negative electrode signifying that despite the proposed defect ion stabilization process, excess mobile ions still remain in the material. The continual formation and growth of these stable PL quenched areas when the electrode polarity is reversed explains why the switch experiments show a systematic change in the PL and current transient responses. The stable quenched areas likely have different defect ion mobilities so the ion migration is suppressed over time, explaining why not all switch responses show the peak/recover behavior expected following an ion migration as discussed above. Thus, there is strong evidence that the irreversible PL quenching behavior under sufficient applied bias is a result of ion migration, but the exact mechanism leading to the irreversible PL quenching still needs to be identified.

Based on the above analysis, the ion migration only occurs when the applied bias is above the threshold, 1 V, and when the electrode polarity is switched. Therefore, a charge trapping mechanism is used to explain the 1 V experiments and the second through fourth transients of the repeat experiments as depicted in Figure 2.7b. Surface and interface traps in $MAPbI_3$ films are commonly cited as a potential source of the transient response,[8, 55-57] but little is known about the atomistic or energetic details of these traps. In this system, the $MAPbI_3$ grains are on the order of 1 μm, compared to the 10 μm electrode gap distances, so there is significant surface and grain boundary interfacial area with potential trap states. Furthermore, no solvent annealing was performed on these samples, so bulk crystal defects are also likely present. Prior to the application of the applied voltage (region I), the system is in steady state with the excess

photogenerated charge carriers filling of the trap states to a steady state level. When the bias is applied (region II), the excess photogenerated charge carriers are swept through the electrodes producing the current spike and sharp PL quenching before the traps can respond. The fast sweeping of both electron and holes reduces the photocarrier population, which in turn, changes the trap dynamics. This leads to a slow emptying of the trap states, dependent on the trap energy and the emission rate from each trap, until a lower steady state value is reached. This slow trap emission process (region III) provides a decaying source of excess free charge carriers leading to the slow monotonic increase and decrease in the current and PL respectively. Furthermore, as the traps empty to the lower steady state value under the applied bias, there will be an increase in the concentration of empty traps, and therefore, an increasing probability of a nonradiative recombination pathway for excess photogenerated carriers as the system reaches steady state. When the electrical bias is removed, the traps will fill as the concentration of the photogenerated carriers and trap states reach steady state. Within this context, the existence of the two transients ($\tau_{1,PL}$ and $\tau_{2,PL}$) could be explained by multiple traps with a range of energy levels and trap emission rates.

The above qualitative analysis correlates well with the trends seen in the isolated responses, but relies on the assumption that these mechanisms are independent from each other. However, because the mechanisms dynamically adjust the effective electric field and the free charge carrier population, for an ion migration and charge trapping mechanism, respectively, they are each ultimately affected by each other. Furthermore, the two processes occur simultaneously when the bias is applied and each occur over similar timescales. This makes detailed quantitative analysis of either mechanism

extremely challenging and beyond the scope of this dissertation. Nevertheless, it is proposed that the IDE device used in this study was essential to differentiate these distinct processes. The 10 μm gap distances in the IDE device is much greater than the 500 nm thickness in the vertically stacked devices, which leads to longer ion transient times and larger spatial separation. This slowed the transient responses limited by the ion migration based on the increase in ion transient times across the larger distances, and therefore created greater distinction between the reversible and irreversible responses. The ability to differentiate between each distinct mechanism is critical to gain a deeper understanding of this material system. For example, in this system, a threshold for ion migration was found to be between 1 $kVcm^{-1}$ and 5 $kVcm^{-1}$, which is smaller than the electric fields used in optimized planar vertically stacked solar cell devices under working conditions (~15 $kVcm^{-1}$). While this threshold for migration is strongly dependent on materials composition and morphology, which will vary widely across the different fabrication techniques and between the IDE and vertically stacked planar devices, it supports the growing evidence that ion migration likely contributes to the slow transient, and therefore hysteretic, behavior commonly reported in even the highest performing perovskite solar cell devices.

2.4 References

1. Egger, D. A.; Edri, E.; Cahen, D.; Hodes, G., Perovskite Solar Cells: Do We Know What We Do Not Know? *J. Phys. Chem. Lett.* **2015,** *6*, 279-282.

2. Snaith, H. J.; Abate, A.; Ball, J. M.; Eperon, G. E.; Leijtens, T.; Noel, N. K.; Stranks, S. D.; Wang, J. T.-W.; Wojciechowski, K.; Zhang, W., Anomalous Hysteresis in Perovskite Solar Cells. *J. Phys. Chem. Lett.* **2014,** *5*, 1511-1515.

3. Unger, E. L.; Hoke, E. T.; Bailie, C. D.; Nguyen, W. H.; Bowring, A. R.; Heumuller, T.; Christoforo, M. G.; McGehee, M. D., Hysteresis and Transient Behavior

in Current-Voltage Measurements of Hybrid-Perovskite Absorber Solar Cells. *Energy Environ. Sci.* **2014,** *7*, 3690-3698.

4. Kim, H.-S.; Park, N.-G., Parameters Affecting I–V Hysteresis of CH3NH3PbI3 Perovskite Solar Cells: Effects of Perovskite Crystal Size and Mesoporous TiO2 Layer. *J. Phys. Chem. Lett.* **2014,** *5*, 2927-2934.

5. Gottesman, R.; Haltzi, E.; Gouda, L.; Tirosh, S.; Bouhadana, Y.; Zaban, A.; Mosconi, E.; De Angelis, F., Extremely Slow Photoconductivity Response of CH3NH3PbI3 Perovskites Suggesting Structural Changes under Working Conditions. *J. Phys. Chem. Lett.* **2014,** *5*, 2662-2669.

6. Tress, W.; Marinova, N.; Moehl, T.; Zakeeruddin, S. M.; Nazeeruddin, M. K.; Gratzel, M., Understanding the Rate-Dependent J-V Hysteresis, Slow Time Component, and Aging in CH3NH3PbI3 Perovskite Solar Cells: the Role of a Compensated Electric Field. *Energy Environ. Sci.* **2015,** *8*, 995-1004.

7. Gonzalez-Pedro, V.; Juarez-Perez, E. J.; Arsyad, W.-S.; Barea, E. M.; Fabregat-Santiago, F.; Mora-Sero, I.; Bisquert, J., General Working Principles of CH3NH3PbX3 Perovskite Solar Cells. *Nano Lett.* **2014,** *14*, 888-893.

8. Shao, Y.; Xiao, Z.; Bi, C.; Yuan, Y.; Huang, J., Origin and Elimination of Photocurrent Hysteresis by Fullerene Passivation in CH3NH3PbI3 Planar Heterojunction Solar Cells. *Nat. Commun.* **2014,** *5*, 5784.

9. Sanchez, R. S.; Gonzalez-Pedro, V.; Lee, J.-W.; Park, N.-G.; Kang, Y. S.; Mora-Sero, I.; Bisquert, J., Slow Dynamic Processes in Lead Halide Perovskite Solar Cells. Characteristic Times and Hysteresis. *J. Phys. Chem. Lett.* **2014,** *5*, 2357-2363.

10. Juarez-Perez, E. J.; Sanchez, R. S.; Badia, L.; Garcia-Belmonte, G.; Kang, Y. S.; Mora-Sero, I.; Bisquert, J., Photoinduced Giant Dielectric Constant in Lead Halide Perovskite Solar Cells. *J. Phys. Chem. Lett.* **2014,** *5*, 2390-2394.

11. Xiao, Z.; Yuan, Y.; Shao, Y.; Wang, Q.; Dong, Q.; Bi, C.; Sharma, P.; Gruverman, A.; Huang, J., Giant Switchable Photovoltaic Effect in Organometal Trihalide Perovskite Devices. *Nat. Mater.* **2014,** *14*, 193-198.

12. Deng, Y.; Xiao, Z.; Huang, J., Light-Induced Self-Poling Effect on Organometal Trihalide Perovskite Solar Cells for Increased Device Efficiency and Stability. *Adv. Energy Mater.* **2015,** *5*, 1500721.

13. Yuan, Y.; Chae, J.; Shao, Y.; Wang, Q.; Xiao, Z.; Centrone, A.; Huang, J., Photovoltaic Switching Mechanism in Lateral Structure Hybrid Perovskite Solar Cells. *Adv. Energy Mater.* **2015,** *5*, 1500615.

14. Zhao, Y.; Liang, C.; Zhang, H.; Li, D.; Tian, D.; Li, G.; Jing, X.; Zhang, W.; Xiao, W.; Liu, Q.; Zhang, F.; He, Z., Anomalously Large Interface Charge in Polarity-

Switchable Photovoltaic Devices: an Indication of Mobile Ions in Organic-Inorganic Halide Perovskites. *Energy Environ. Sci.* **2015,** *8*, 1256-1260.

15. Azpiroz, J. M.; Mosconi, E.; Bisquert, J.; De Angelis, F., Defect Migration in Methylammonium Lead Iodide and its Role in Perovskite Solar Cell Operation. *Energy Environ. Sci.* **2015,** *8*, 2118-2127.

16. Eames, C.; Frost, J. M.; Barnes, P. R. F.; O'Regan, B. C.; Walsh, A.; Islam, M. S., Ionic Transport in Hybrid Lead Iodide Perovskite Solar Cells. *Nat. Commun.* **2015,** *6*, 7497.

17. Leijtens, T.; Hoke, E. T.; Grancini, G.; Slotcavage, D. J.; Eperon, G. E.; Ball, J. M.; De Bastiani, M.; Bowring, A. R.; Martino, N.; Wojciechowski, K.; McGehee, M. D.; Snaith, H. J.; Petrozza, A., Mapping Electric Field-Induced Switchable Poling and Structural Degradation in Hybrid Lead Halide Perovskite Thin Films. *Adv. Energy Mater.* **2015,** *5*, 1500962.

18. Frost, J. M.; Butler, K. T.; Brivio, F.; Hendon, C. H.; van Schilfgaarde, M.; Walsh, A., Atomistic Origins of High-Performance in Hybrid Halide Perovskite Solar Cells. *Nano Lett.* **2014,** *14*, 2584-2590.

19. Wu, X.; Yu, H.; Li, L.; Wang, F.; Xu, H.; Zhao, N., Composition-Dependent Light-Induced Dipole Moment Change in Organometal Halide Perovskites. *J. Phys. Chem. C* **2015,** *119*, 1253-1259.

20. Bertoluzzi, L.; Sanchez, R. S.; Liu, L.; Lee, J.-W.; Mas-Marza, E.; Han, H.; Park, N.-G.; Mora-Sero, I.; Bisquert, J., Cooperative Kinetics of Depolarization in CH3NH3PbI3 Perovskite Solar Cells. *Energy Environ. Sci.* **2015,** *8*, 910-915.

21. Kutes, Y.; Ye, L.; Zhou, Y.; Pang, S.; Huey, B. D.; Padture, N. P., Direct Observation of Ferroelectric Domains in Solution-Processed CH3NH3PbI3 Perovskite Thin Films. *J. Phys. Chem. Lett.* **2014,** *5*, 3335-3339.

22. Leguy, A. M. A.; Frost, J. M.; McMahon, A. P.; Sakai, V. G.; Kockelmann, W.; Law, C.; Li, X.; Foglia, F.; Walsh, A.; O'Regan, B. C.; Nelson, J.; Cabral, J. T.; Barnes, P. R. F., The Dynamics of Methylammonium Ions in Hybrid Organic–Inorganic Perovskite Solar Cells. *Nat. Commun.* **2015,** *6*, 7124.

23. Fan, Z.; Xiao, J.; Sun, K.; Chen, L.; Hu, Y.; Ouyang, J.; Ong, K. P.; Zeng, K.; Wang, J., Ferroelectricity of CH3NH3PbI3 Perovskite. *J. Phys. Chem. Lett.* **2015,** *6*, 1155-1161.

24. Hsiao, Y.-C.; Wu, T.; Li, M.; Hu, B., Magneto-Optical Studies on Spin-Dependent Charge Recombination and Dissociation in Perovskite Solar Cells. *Adv. Mater.* **2015,** *27*, 2899-2906.

25. Grancini, G.; Srimath Kandada, A. R.; Frost, J. M.; Barker, A. J.; De Bastiani, M.; Gandini, M.; Marras, S.; Lanzani, G.; Walsh, A.; Petrozza, A., Role of Microstructure in

the Electron–Hole Interaction of Hybrid Lead Halide Perovskites. *Nat. Photonics* **2015,** *9*, 695-701.

26. Nie, W.; Tsai, H.; Asadpour, R.; Blancon, J.-C.; Neukirch, A. J.; Gupta, G.; Crochet, J. J.; Chhowalla, M.; Tretiak, S.; Alam, M. A.; Wang, H.-L.; Mohite, A. D., High-Efficiency Solution-Processed Perovskite Solar Cells with Millimeter-Scale Grains. *Science* **2015,** *347*, 522-525.

27. Eperon, G. E.; Burlakov, V. M.; Docampo, P.; Goriely, A.; Snaith, H. J., Morphological Control for High Performance, Solution-Processed Planar Heterojunction Perovskite Solar Cells. *Adv. Funct. Mater.* **2014,** *24*, 151-157.

28. Im, J.-H.; Kim, H.-S.; Park, N.-G., Morphology-Photovoltaic Property Correlation in Perovskite Solar Cells: One-Step Versus Two-Step Deposition of CH3NH3PbI3. *APL Mater.* **2014,** *2*, 081510.

29. Zhu, F.; Men, L.; Guo, Y.; Zhu, Q.; Bhattacharjee, U.; Goodwin, P. M.; Petrich, J. W.; Smith, E. A.; Vela, J., Shape Evolution and Single Particle Luminescence of Organometal Halide Perovskite Nanocrystals. *ACS Nano* **2015,** *9*, 2948-2959.

30. Fu, F.; Kranz, L.; Yoon, S.; Löckinger, J.; Jäger, T.; Perrenoud, J.; Feurer, T.; Gretener, C.; Buecheler, S.; Tiwari, A. N., Controlled Growth of PbI2 Nanoplates for Rapid Preparation of CH3NH3PbI3 in Planar Perovskite Solar Cells. *Phys. Status Solidi A* **2015,** *212*, 2708-2717.

31. You, J.; Yang, Y.; Hong, Z.; Song, T.-B.; Meng, L.; Liu, Y.; Jiang, C.; Zhou, H.; Chang, W.-H.; Li, G.; Yang, Y., Moisture Assisted Perovskite Film Growth for High Performance Solar Cells. *Appl. Phys. Lett.* **2014,** *105*, 183902.

32. Bi, C.; Wang, Q.; Shao, Y.; Yuan, Y.; Xiao, Z.; Huang, J., Non-Wetting Surface-Driven High-Aspect-Ratio Crystalline Grain Growth for Efficient Hybrid Perovskite Solar Cells. *Nat. Commun.* **2015,** *6*, 7747.

33. Gao, H.; Bao, C.; Li, F.; Yu, T.; Yang, J.; Zhu, W.; Zhou, X.; Fu, G.; Zou, Z., Nucleation and Crystal Growth of Organic–Inorganic Lead Halide Perovskites under Different Relative Humidity. *ACS Appl. Mater. Interfaces* **2015,** *7*, 9110-9117.

34. Tian, Y.; Merdasa, A.; Unger, E.; Abdellah, M.; Zheng, K.; McKibbin, S.; Mikkelsen, A.; Pullerits, T.; Yartsev, A.; Sundström, V.; Scheblykin, I. G., Enhanced Organo-Metal Halide Perovskite Photoluminescence from Nanosized Defect-Free Crystallites and Emitting Sites. *J. Phys. Chem. Lett.* **2015,** *6*, 4171-4177.

35. Galisteo-López, J. F.; Anaya, M.; Calvo, M. E.; Míguez, H., Environmental Effects on the Photophysics of Organic–Inorganic Halide Perovskites. *J. Phys. Chem. Lett.* **2015,** *6*, 2200-2205.

36. Tian, Y.; Peter, M.; Unger, E.; Abdellah, M.; Zheng, K.; Pullerits, T.; Yartsev, A.; Sundstrom, V.; Scheblykin, I. G., Mechanistic Insights into Perovskite

Photoluminescence Enhancement: Light Curing with Oxygen can Boost Yield Thousandfold. *Phys. Chem. Chem. Phys.* **2015,** *17*, 24978-24987.

37. Christians, J. A.; Miranda Herrera, P. A.; Kamat, P. V., Transformation of the Excited State and Photovoltaic Efficiency of CH3NH3PbI3 Perovskite upon Controlled Exposure to Humidified Air. *J. Am. Chem. Soc.* **2015,** *137*, 1530-1538.

38. Eperon, G. E.; Stranks, S. D.; Menelaou, C.; Johnston, M. B.; Herz, L. M.; Snaith, H. J., Formamidinium Lead Trihalide: a Broadly Tunable Perovskite for Efficient Planar Heterojunction Solar Cells. *Energy Environ. Sci.* **2014,** *7*, 982-988.

39. Pellet, N.; Gao, P.; Gregori, G.; Yang, T.-Y.; Nazeeruddin, M. K.; Maier, J.; Grätzel, M., Mixed-Organic-Cation Perovskite Photovoltaics for Enhanced Solar-Light Harvesting. *Angew. Chem., Int. Ed.* **2014,** *53*, 3151-3157.

40. Kong, W.; Ye, Z.; Qi, Z.; Zhang, B.; Wang, M.; Rahimi-Iman, A.; Wu, H., Characterization of an Abnormal Photoluminescence Behavior Upon Crystal-Phase Transition of Perovskite CH3NH3PbI3. *Phys. Chem. Chem. Phys.* **2015,** *17*, 16405-16411.

41. Docampo, P.; Ball, J. M.; Darwich, M.; Eperon, G. E.; Snaith, H. J., Efficient Organometal Trihalide Perovskite Planar-Heterojunction Solar Cells on Flexible Polymer Substrates. *Nat. Commun.* **2013,** *4*, 2761.

42. Abrusci, A.; Stranks, S. D.; Docampo, P.; Yip, H.-L.; Jen, A. K. Y.; Snaith, H. J., High-Performance Perovskite-Polymer Hybrid Solar Cells via Electronic Coupling with Fullerene Monolayers. *Nano Lett.* **2013,** *13*, 3124-3128.

43. Roiati, V.; Colella, S.; Lerario, G.; De Marco, L.; Rizzo, A.; Listorti, A.; Gigli, G., Investigating Charge Dynamics in Halide Perovskite-Sensitized Mesostructured Solar Cells. *Energy Environ. Sci.* **2014,** *7*, 1889-1894.

44. Stranks, S. D.; Eperon, G. E.; Grancini, G.; Menelaou, C.; Alcocer, M. J.; Leijtens, T.; Herz, L. M.; Petrozza, A.; Snaith, H. J., Electron-Hole Diffusion Lengths Exceeding 1 Micrometer in an Organometal Trihalide Perovskite Absorber. *Science* **2013,** *342*, 341-4.

45. Xing, G.; Mathews, N.; Sun, S.; Lim, S. S.; Lam, Y. M.; Gratzel, M.; Mhaisalkar, S.; Sum, T. C., Long-Range Balanced Electron- and Hole-Transport Lengths in Organic-Inorganic CH3NH3PbI3. *Science* **2013,** *342*, 344-7.

46. Shi, D.; Adinolfi, V.; Comin, R.; Yuan, M.; Alarousu, E.; Buin, A.; Chen, Y.; Hoogland, S.; Rothenberger, A.; Katsiev, K.; Losovyj, Y.; Zhang, X.; Dowben, P. A.; Mohammed, O. F.; Sargent, E. H.; Bakr, O. M., Low Trap-State Density and Long Carrier Diffusion in Organolead Trihalide Perovskite Single Crystals. *Science* **2015,** *347*, 519-522.

47. Stranks, S. D.; Burlakov, V. M.; Leijtens, T.; Ball, J. M.; Goriely, A.; Snaith, H. J., Recombination Kinetics in Organic-Inorganic Perovskites: Excitons, Free Charge, and Subgap States. *Phys. Rev. Appl.* **2014,** *2*, 034007.

48. Tvingstedt, K.; Malinkiewicz, O.; Baumann, A.; Deibel, C.; Snaith, H. J.; Dyakonov, V.; Bolink, H. J., Radiative Efficiency of Lead Iodide Based Perovskite Solar Cells. *Sci. Rep.* **2014,** *4*, 6071.

49. Wehrenfennig, C.; Eperon, G. E.; Johnston, M. B.; Snaith, H. J.; Herz, L. M., High Charge Carrier Mobilities and Lifetimes in Organolead Trihalide Perovskites. *Adv. Mater.* **2014,** *26*, 1584-1589.

50. Buin, A.; Pietsch, P.; Xu, J.; Voznyy, O.; Ip, A. H.; Comin, R.; Sargent, E. H., Materials Processing Routes to Trap-Free Halide Perovskites. *Nano Lett.* **2014,** *14*, 6281-6286.

51. Yin, W.-J.; Shi, T.; Yan, Y., Unusual Defect Physics in CH3NH3PbI3 Perovskite Solar Cell Absorber. *Appl. Phys. Lett.* **2014,** *104*, 063903.

52. deMello, J. C.; Tessler, N.; Graham, S. C.; Friend, R. H., Ionic Space-Charge Effects in Polymer Light-Emitting Diodes. *Phys. Rev. B* **1998,** *57*, 12951-12963.

53. Sze, S. M.; Ng, K. K., *Physics of Semiconductor Devices*, 3rd ed.; John Wiley & Sons, Inc.: Hoboken, New Jersey, 2007.

54. Agiorgousis, M. L.; Sun, Y.-Y.; Zeng, H.; Zhang, S., Strong Covalency-Induced Recombination Centers in Perovskite Solar Cell Material CH3NH3PbI3. *J. Am. Chem. Soc.* **2014,** *136*, 14570-14575.

55. Noel, N. K.; Abate, A.; Stranks, S. D.; Parrott, E. S.; Burlakov, V. M.; Goriely, A.; Snaith, H. J., Enhanced Photoluminescence and Solar Cell Performance via Lewis Base Passivation of Organic–Inorganic Lead Halide Perovskites. *ACS Nano* **2014,** *8*, 9815-9821.

56. van Reenen, S.; Kemerink, M.; Snaith, H. J., Modeling Anomalous Hysteresis in Perovskite Solar Cells. *J. Phys. Chem. Lett.* **2015,** *6*, 3808-3814.

57. Xu, J.; Buin, A.; Ip, A. H.; Li, W.; Voznyy, O.; Comin, R.; Yuan, M.; Jeon, S.; Ning, Z.; McDowell, J. J.; Kanjanaboos, P.; Sun, J.-P.; Lan, X.; Quan, L. N.; Kim, D. H.; Hill, I. G.; Maksymovych, P.; Sargent, E. H., Perovskite–Fullerene Hybrid Materials Suppress Hysteresis in Planar Diodes. *Nat. Commun.* **2015,** *6*, 7081.

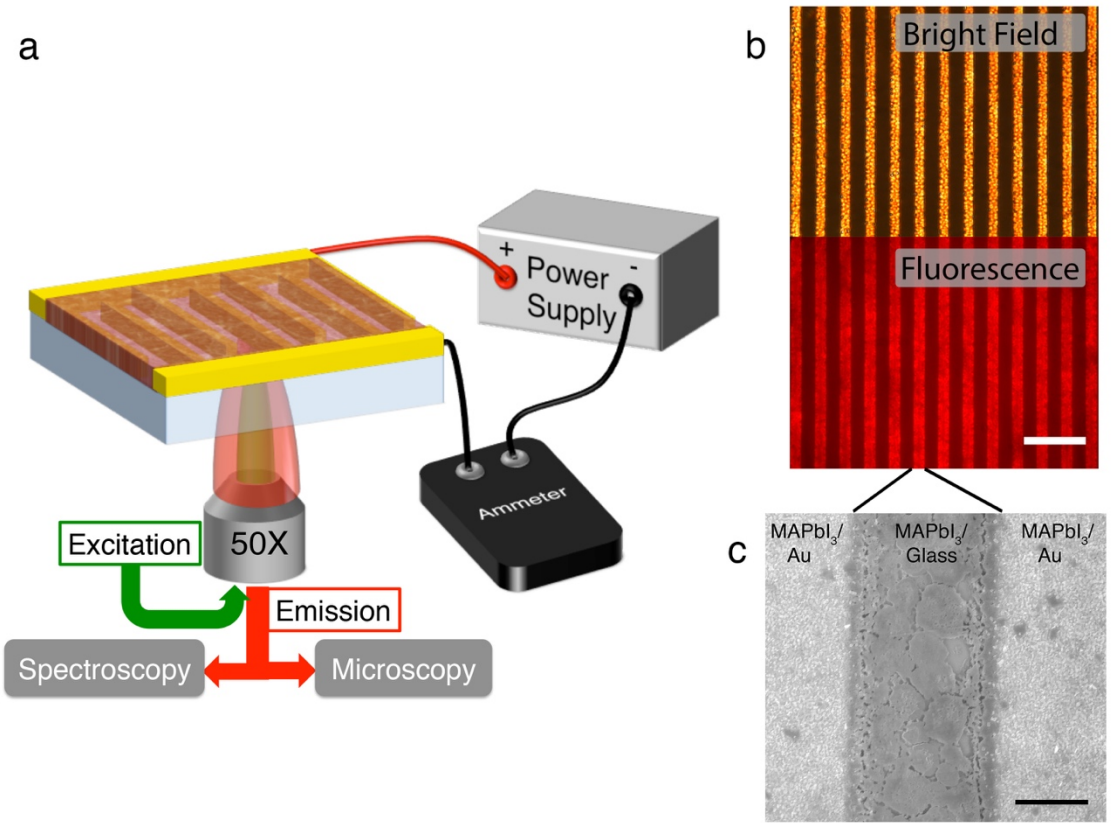

Figure 2.1. IDE device architecture. a) Schematic of the testing platform used for the PL and current response to an applied electrical bias. b) Optical microscope images of the full collected area in bright field mode (top*)* and fluorescence mode (bottom*)*. The scale bar is 50 µm. c) SEM image of the IDE device with $MAPbI_3$ showing good gap filling between the electrodes. Scale bar is 5µm. (Reprinted with permission from Jacobs, D. L.; Scarpulla, M. A.; Wang, C.; Bunes, B. R.; Zang, L., Voltage-Induced Transients in Methylammonium Lead Triiodide Probed by Dynamic Photoluminescence Spectroscopy. *J. Phys. Chem. C* **2016,** *120*, 7893-7902. Copyright (2016) American Chemical Society.)

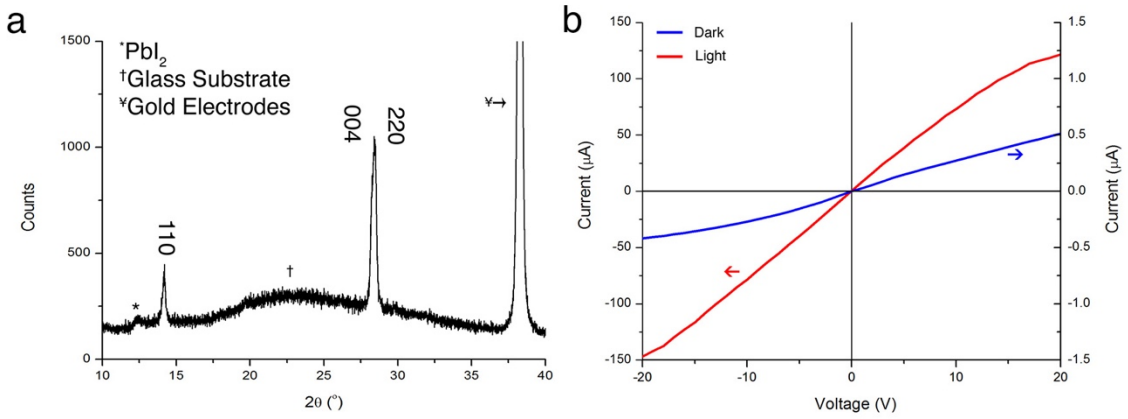

Figure 2.2. Characterization of the MAPbI3 film. a) XRD spectrum with the identified peaks labeled. b) Current voltage curves of $MAPbI_3$ coated IDE devices. For the photocurrent measurements, the entire IDE area was illuminated.

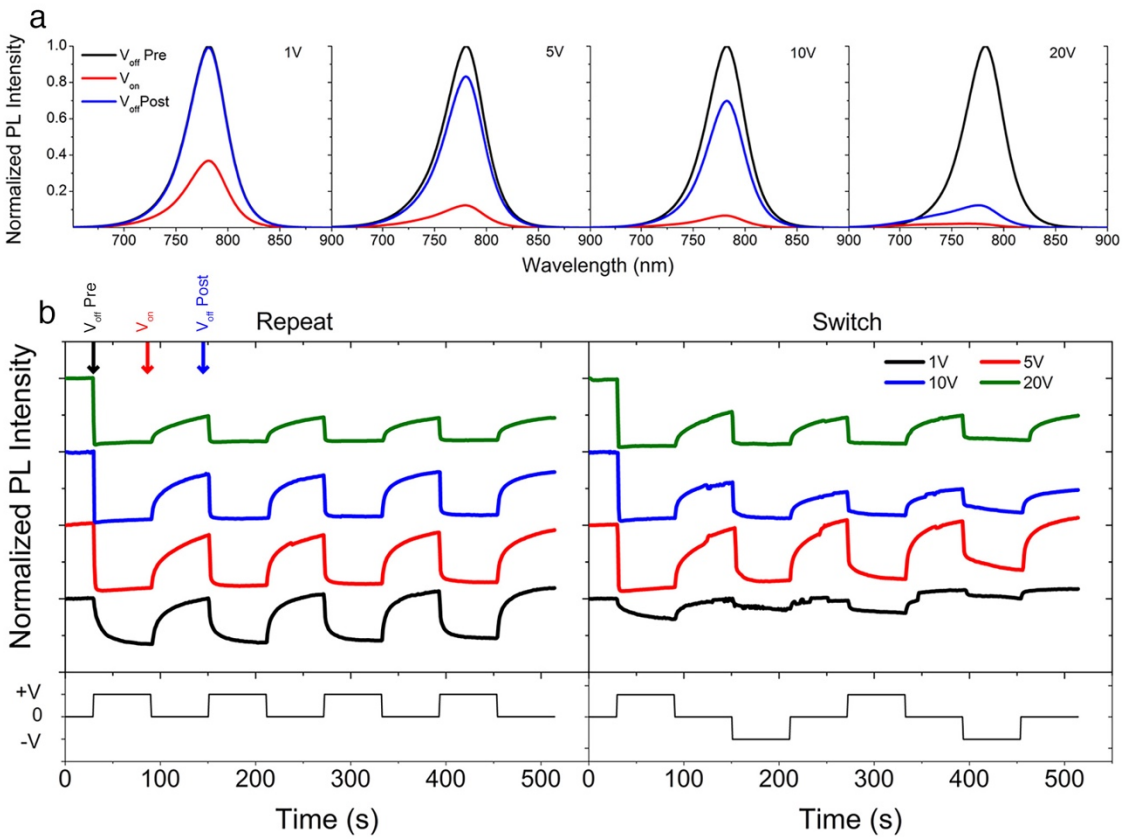

Figure 2.3. Summary of the PL results. Individual PL spectra taken from the time resolved PL repeat experiment before, during, and after (black, red, and blue lines respectively) the application of a 1, 5, 10 and 20 V bias. The isolated spectra frames correspond to the times represented by the matching color arrows seen in the time profiles in Figure 1b. The spectra at each voltage are normalized to the peak maximum of the prebias curve (black). b) Time resolved profile of the PL response to the applied bias for both repeat (left) and switch (right) experiments. The intensity represents the maximum peak value, which is normalized to the initial value and offset vertically to aid comparisons. The graphs below the PL response profiles represent the applied electrode polarity, where +V is the direction of the first applied voltage and the –V represents the polarity when the leads to the test structure were switched. (Reprinted with permission from Jacobs, D. L.; Scarpulla, M. A.; Wang, C.; Bunes, B. R.; Zang, L., Voltage-Induced Transients in Methylammonium Lead Triiodide Probed by Dynamic Photoluminescence Spectroscopy. *J. Phys. Chem. C* **2016,** *120*, 7893-7902. Copyright (2016) American Chemical Society.)

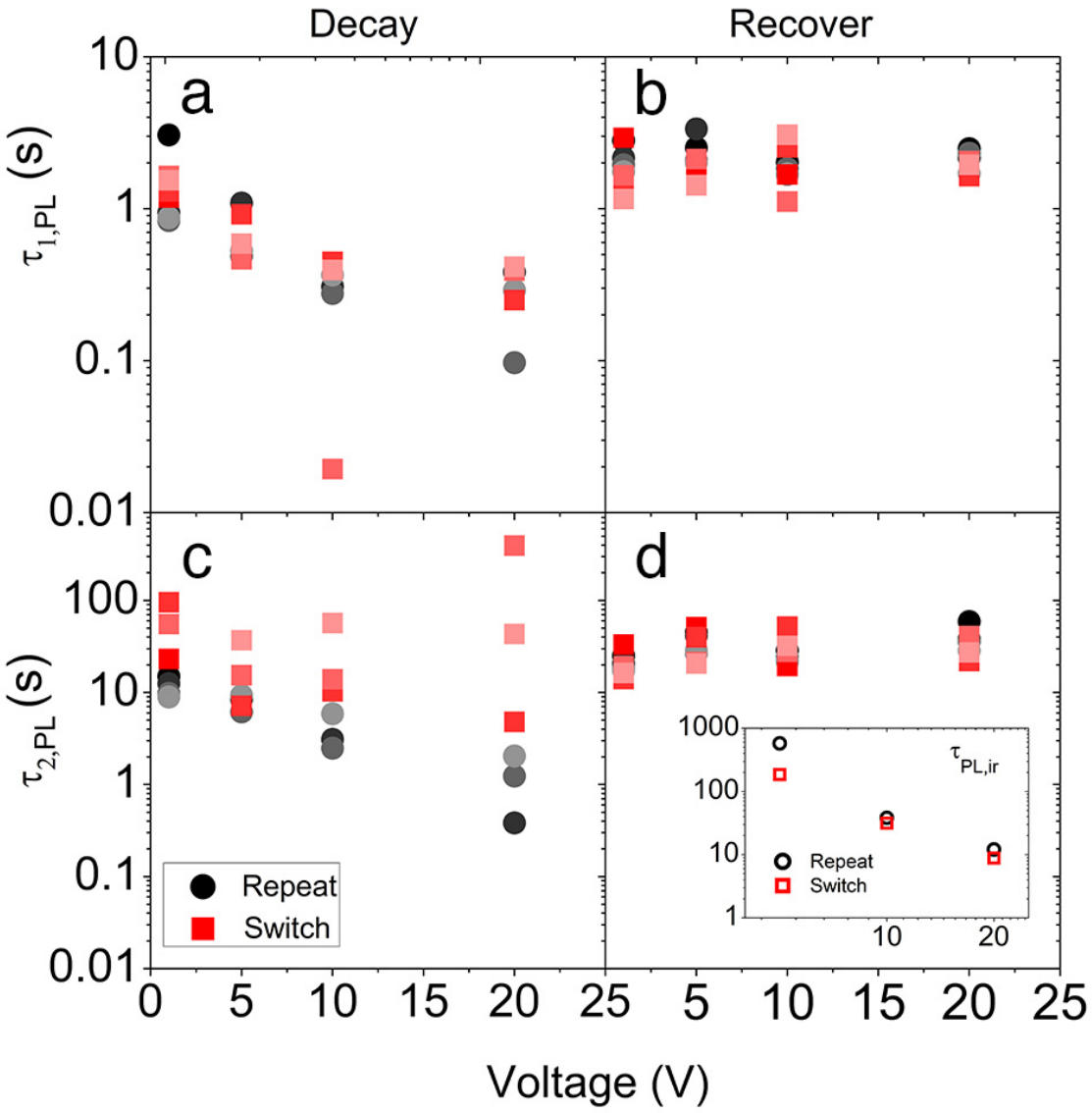

Figure 2.4. Graphs of the fitted time constants: fast $\tau_{1,PL}$ (a,b) and slow $\tau_{2,PL}$ (c,d) time constants from the isolated decay (a,c) and recover (b,d) response at each voltage. Both repeat (black circle) and switch (red square) are shown. The response number is identified with decreasing color saturation of the red or black symbols. The grey dotted line represents the sensor exposure time. The inset in d) summarizes the over shoot recovery response to an application of a bias greater than 1 V. (Reprinted with permission from Jacobs, D. L.; Scarpulla, M. A.; Wang, C.; Bunes, B. R.; Zang, L., Voltage-Induced Transients in Methylammonium Lead Triiodide Probed by Dynamic Photoluminescence Spectroscopy. *J. Phys. Chem. C* **2016,** *120*, 7893-7902. Copyright (2016) American Chemical Society.)

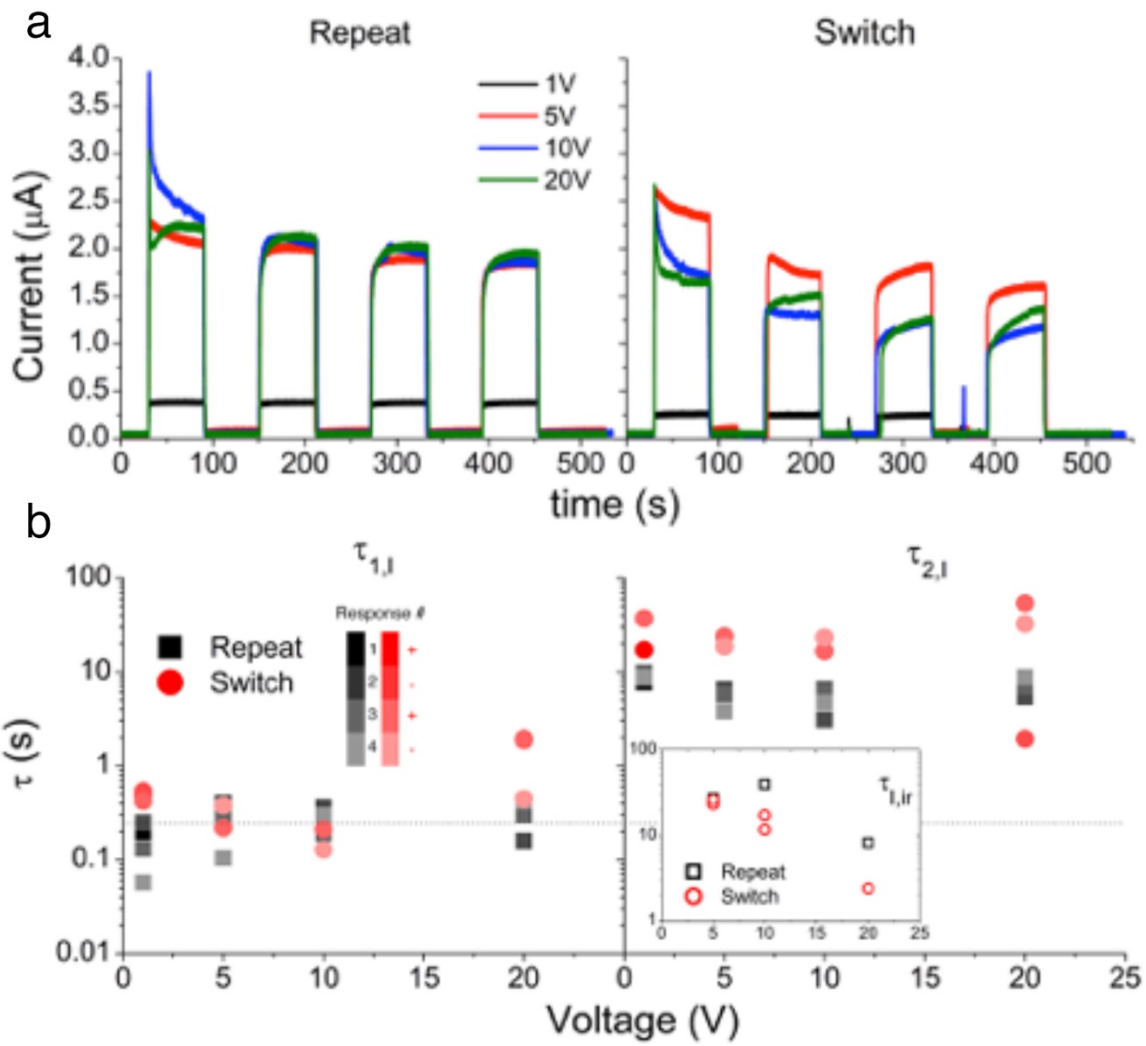

Figure 2.5. Current response. a) Time resolved current response profile for repeat (left) and switch (right) experiments. b) Summary of the fitted time constants for the current transient responses. The left panel represents the fast ($\tau_{1,I}$) responses and the right panel represents the slow ($\tau_{2,I}$) responses. The inset in the right panel shows the recovery from the current spike to steady state. The dotted line represents the sampling rate for the ammeter. Black squares represent the repeat experiments and red circles represent the switch experiments. The decrease in symbol color saturation represents an increase in the response number. (Reprinted with permission from Jacobs, D. L.; Scarpulla, M. A.; Wang, C.; Bunes, B. R.; Zang, L., Voltage-Induced Transients in Methylammonium Lead Triiodide Probed by Dynamic Photoluminescence Spectroscopy. *J. Phys. Chem. C* **2016,** *120*, 7893-7902. Copyright (2016) American Chemical Society.)

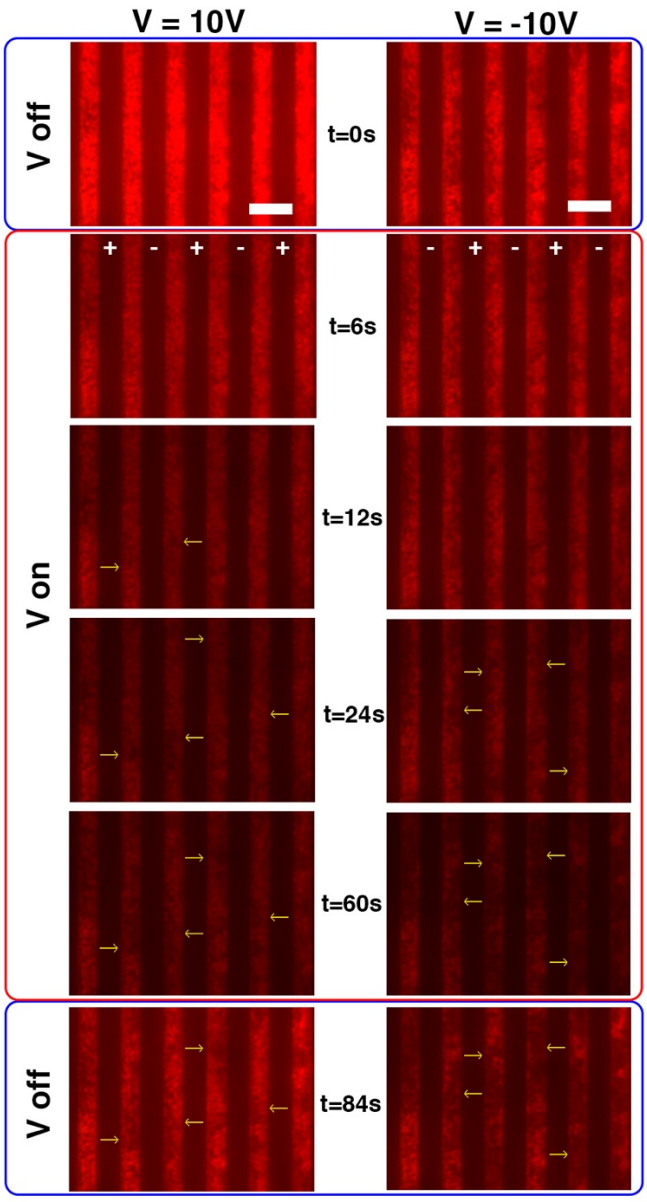

Figure 2.6. PL microscopy images showing the spatial dependent PL response to +10 V (left panel) and -10 V biases (right panel). The images are cropped from frames taken from Supporting Movie 1 (+10 V) and Supporting Movie 2 (-10 V). The listed time values represent the time from when the bias was applied with 0s being the frame directly before the application of the bias. Yellow arrows indicate the areas with the most notable changes in PL. The electrode polarity is labeled on the frame at t=6 s when the bias is applied. The scale bars are both 20 μm. (Reprinted with permission from Jacobs, D. L.; Scarpulla, M. A.; Wang, C.; Bunes, B. R.; Zang, L., Voltage-Induced Transients in Methylammonium Lead Triiodide Probed by Dynamic Photoluminescence Spectroscopy. *J. Phys. Chem. C* **2016,** *120*, 7893-7902. Copyright (2016) American Chemical Society.)

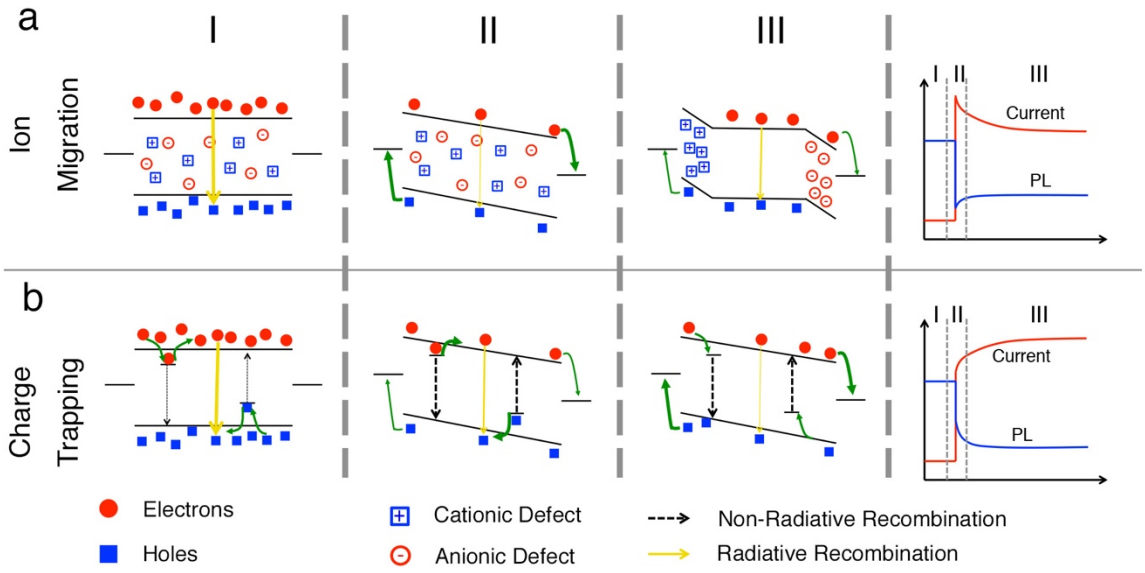

Figure 2.7. Schematic representation of the proposed mechanisms, a) defect ion migration b) charge trapping, at different stages. (I) equilibrium with the light excitation, (II) immediately after the voltage is applied, and (III) the slow transient response to the steady state conditions. The far right column shows the expected current and PL responses correlating to regions I, II, and III. (Reprinted with permission from Jacobs, D. L.; Scarpulla, M. A.; Wang, C.; Bunes, B. R.; Zang, L., Voltage-Induced Transients in Methylammonium Lead Triiodide Probed by Dynamic Photoluminescence Spectroscopy. *J. Phys. Chem. C* **2016,** *120*, 7893-7902. Copyright (2016) American Chemical Society.)

CHAPTER 3

THERMALLY INDUCED RECRYSTALLIZATION OF $MAPBI_3$ PEROVSKITE UNDER METHYLAMINE ATMOSPHERE: AN APPROACH TO FABRICATING LARGE UNIFORM CRYSTALLINE GRAINS

3.1 Motivation

Hybrid organic-inorganic photovoltaic devices, particularly those based on methylammonium lead triiodide ($MAPbI_3$), have shown unprecedented performance enhancement in less than a decade, with the most recent record efficiencies above 20%.[1] However, controlling the deposition and crystallization of $MAPbI_3$ has been a significant challenge in reproducibly fabricating high-efficiency devices. Early devices were typically fabricated from a simple 1-step spin coating deposition followed by thermal annealing to recrystallize the film. However, these films suffered from large and non-uniform grains due to the fast crystal growth kinetics during the annealing step, which also leads to the formation of significant pinhole area that limit device performance.[2] Major breakthroughs in $MAPbI_3$-based solar cells have stemmed from new deposition techniques capable of forming large area, uniform, smooth, and pin hole-free thin films. Such techniques include the 2-step deposition methods,[3-4] anti-solvent methods,[5-6] and the hot casting method.[7] The common underlying mechanism behind the enhanced surface

coverage from these techniques is based on increasing the nucleation kinetics during crystallization, which results in small uniform grains across the substrate.[8] However, this comes at the cost of increased grain boundary area, which can also limit the photovoltaic performance. While there have been several techniques developed to increase the grain size through traditional post deposition techniques, such as thermal or solvent annealing, the resulting grains are still typically limited to the micron scale or less.[9-10] The hot casting technique developed by Nie et al. has reported ultra large grains up to the millimeter scale,[7] however, subsequent detailed studies of this method suggest that these domains are not single crystals, rather the large area domains are compositions of smaller crystal grains formed in a Volmer-Weber thin film growth process.[11-12]

Among the many promising physical properties of organo-metallic hybrid perovskite materials, the reported room temperature solid to liquid phase transition under methylamine (MA) gas atmosphere is particularly unique. Zhou et al. first reported the phenomenon and found that short exposure of a $MAPbI_3$ thin film to MA gas at room temperature causes an immediate color change from dark brown to completely transparent, and when removed from the MA atmosphere, the process quickly reversed.[13] The morphology of the MA treated films show ultra smooth surfaces across the entire sample with enhanced crystallinity leading to improved photovoltaic performance. However, the grain sizes may actually decrease by up to an order of magnitude after exposure to MA.[14] The interaction between MA and $MAPbI_3$ is believed to be a result of polar MA molecules disrupting the ionic bonding of the Pb-I lattice causing a collapse of the crystal structure and forming a $MAPbI_3$•xMA liquid phase, with x being estimated at ~3.5.[13] When the film is removed from the MA atmosphere, the complex formation

quickly reverses as the gas molecules are expelled and $MAPbI_3$ is recrystallized. Compared to a solvent phase crystallization process, which requires the liquid solvent molecules to evaporate before crystallization can occur, the gas phase MA molecules are expelled from the film uniformly and at a much faster rate. This effectively quenches molecular transport, and thereby crystal growth, leading to formation of fine grained thin films dominated by a nucleation process.[8] Thus, techniques to fabricate large area single crystal grains uniformly across the surface remains a significant barrier to further improving device performance.

3.2 Thermal-Induced Recrystallization Under Methylamine Atmosphere

In this work, the above reported gas phase annealing process was further investigated at elevated temperatures, 25˚C - 100˚C, as shown in Figure 3.1. It was found that above 55˚C, the liquid phase of $MAPbI_3$ under MA atmosphere becomes unstable, and starts transitioning back to the solid state. At 100˚C, no liquid intermediate phase exists. This liquid-solid phase transition at higher temperatures, as illustrated in the one-dimensional (1-D) phase diagram (Figure 3.1), is similar to the inverse temperature crystallization phenomenon as observed in solution phase for many of the organo-metallic halide perovskites. For example, $MAPbI_3$ can precipitate out of a heated solution in γ-butyrolacetone, which can be used to rapidly grow large single crystals through controlled heating of the solution.[15] Following a similar approach, high-quality and uniform large area thin films of $MAPbI_3$ with large, highly crystalline grains were formed from the thermal-induced recrystallization under methylamine atmosphere (TIRMA) process introduced herein.

3.2.1 Experimental methods

3.2.1.1 Material synthesis

Methylammonium iodide (MAI) was synthesized by reacting methylamine (40 wt. % in water) with equimolar amounts of HI (57 wt. % in water) in ambient atmosphere at 0 ˚C for 2 h. The solution was dried in a roto-evaporator at 75 ˚C. The precipitate was washed three times with diethyl ether and dried at 50 ˚C in a vacuum oven. PbI_2 (99.9985% metals basis) was obtained from Alfa Aesar and used as received. The $MAPbI_3$ precursor solution was made by dissolving PbI_2 and MAI in DMF at 60 ˚C overnight.

3.2.1.2 $MAPbI_3$ film fabrication

1”x1” glass slides were cleaned by ultrasonicating for 15 min in detergent, deionized water, acetone, methanol, and isopropanol, respectively. The slides were blown dry under a stream of N_2 and UVO cleaned for 30 min. 100 µL of the $MAPbI_3$ precursor solution was dropcast onto the cleaned slides and spun at 1000 rpm for 10 s followed by 3000 rpm for 30 s in air. 400 µL of chlorobenzene was dripped onto the spinning substrates 10 s after the start of the 3000 rpm spin stage. The films were then annealed at 100˚C for 20 min under a dark petri dish and cooled to room temperature in a desiccator.

3.2.1.3 Methylamine annealing experiments (Figure 3.1)

The $MAPbI_3$ films were loaded into the sample chamber on a preheated hotplate. The chamber was purged with nitrogen for 5 min. The methylamine (MA) was introduced by routing the nitrogen carrier gas through the headspace of a 100 mL two-necked round bottom flask with 5mL of a 33 wt% MA solution in ethanol. The sample

was left under flowing MA atmosphere and the corresponding temperature for 1 min. The chamber was then purged with nitrogen for 2 min before the samples were removed and cooled to room temperature.

3.2.1.4 TIRMA process

The as-deposited $MAPbI_3$ films were loaded into the sample chamber at room temperature and purged with nitrogen for 5 min. Flowing MA atmosphere was introduced as described in the above section. After 30 s of MA exposure at room temperature, the chamber was placed onto the preheated hot plate at 100˚C. When the $MAPbI_3$ film completely crystallized (~2 min) the chamber was purged with nitrogen for 2 min while still on the hotplate. Then the chamber was removed from the hotplate and allowed to cool to room temperature before removing the samples and storing in a vacuum desiccator.

3.2.1.5 MA_{RT} film fabrication

Roughly 5 mL of 33 wt% MA in ethanol was added to a 60 mL vial. The samples were taped to the underside of a vial cap. The cap with the sample was quickly placed onto the vial, held for about 1 s, and quickly removed to air. The samples were stored in a vacuum desiccator.

3.2.1.6 Characterization

SEM images were taken with a FEI NovaNano 630 HRSEM. Photoluminescence measurements were taken under flowing Argon on a Leica DMI4000 fluorescence

microscope. The excitation light was supplied by a mercury lamp through a long pass optical filter to deliver 560 nm peak light and emission spectrum was collected with a Acton PIXIS:400B spectrophotometer. XRD spectrum were measured in air with a Bruker D2 Phaser XRD. 2θ scans were measured from 10˚ to 60˚ with 0.02˚ steps for a total scan time of 10 min. Optical absorption measurements were taken in air with a Lambda 950 UV-Vis with a 150 mm integrating sphere module. The absolute transmission (%T) and reflection (%R) were measured, and the absorption (%A) was then calculated as %A = 100-(%T+%R).

3.2.2 Results and discussion

$MAPbI_3$ films were prepared in air on glass substrates via a 1-step spin coating with antisolvent drip technique.[6] The experimental path of the TIRMA process related to changes in the substrate temperature and the gas atmosphere is shown on the 2-D phase diagram in Figure 3.2a. Figure 3.2b shows snapshots of the $MAPbI_3$ films during TIRMA treatment. Samples were loaded into a sealed homemade chamber at room temperature and purged with nitrogen for 5 min. MA gas was introduced by routing the nitrogen flow to a sealed 100 mL flask containing 5 mL of a 33 wt% solution of MA in ethanol to carry the headspace gas to the sample chamber. After being exposed to MA, the opaque dark brown $MAPbI_3$ film was immediately transitioned into the transparent colorless liquid state of $MAPbI_3$•xMA. After 30 s under constant MA atmosphere, the chamber was placed on a hot plate preheated to 100˚C. Upon heating, the film began to recrystallize, initially from the edges, followed by massive growth throughout the film until complete recrystallization occurred. When the recrystallization was complete, the system was

switched back to the nitrogen atmosphere and kept on the hot plate for 2 min. Finally, the chamber was removed from the hotplate and cooled to room temperature. No structural or morphology change of the $MAPbI_3$ film was observed during the nitrogen purge or the cooling steps.

The TIRMA process resulted in exceptional film coverage and film quality as summarized in Figure 3.3. The grain sizes of the TIRMA treated samples increased by about 2 orders of magnitude compared with the pristine film (Figure 3.3a) with an average grain size of the TIRMA treated film estimated to be about 15 μm (Figure 3.3b). The SEM image of the TIRMA treated sample in Figure 3.3b shows a highly crystalline morphology with crystal twin boundaries clearly observed. The sample showed uniform morphology across the surface and no significant pin-holing was observed as evidenced by the cross-sectional SEM image (Figure 3.3c). The enhanced crystallinity of the film is supported by X-ray diffraction (XRD) studies. As seen in Figure 3.3d, the pristine $MAPbI_3$ film showed mostly (110) lattice orientation in addition to several minority orientations. However, the TIRMA treated samples showed an increase in the peak intensity by over 2 orders of magnitude with strong preferred lattice orientation only in the (110) direction. The full width half max (FWHM) of the (110) reflection at 14˚ decreased 36% from 0.106˚ to 0.068˚, signifying a significant increase in grain size. To further show the improved crystallinity and phase purity of the TIRMA treated samples, photoluminescence (PL) spectral measurement was performed for the $MAPbI_3$ film before and after TIRMA treatment (Figure 3.3e). The TIRMA treated sample showed a 10 nm blue shift of the PL peak from 785 to 775, and a decrease in the FWHM from 74 nm to 46 nm, indicating a reduction of low lying bulk and grain boundary defects.[9, 14, 16]

This PL peak shift is accompanied with a blue shift of the absorption band edge seen in the absorption spectrum in Figure 3.3e. The absorption band edge shifts from 1.59 eV for the pristine film to 1.62 eV for the TIRMA treated sample, which converts to about a 15 nm shift, similar to the PL shifting. The absorption spectra in Figure 3.3e show a decrease in the overall absorption after TIRMA treatment. This correlates with the apparent increase in transmission during the TIRMA process visible in Figure 3.2b, which is attributed to the significant change in grain size. The pristine film contains grain sizes on the order of the wavelength of visible light, and should therefore be more efficient in scattering the light within the film, resulting in an increase in the optical path length. In comparison, the TIRMA treated films have grains over an order of magnitude larger than the wavelength of incident light, which should decrease light scattering, and therefore, the path length of light within the film.

For comparison, the fast annealing technique in MA vapor at room temperature (MA_{RT}) used in previously reported studies[13,14] was performed and characterized. In short, the as-deposited film was brought into the headspace of a vial containing the MA solution at room temperature for a short amount of time (~ 1 s), and rapidly brought back into air. Such MA_{RT} treated film was characterized using UV-vis absorption and PL spectra, SEM imaging, and XRD. The MA_{RT} treatment did not result in any significant change in grain size compared to the pristine sample, but did cause observable morphology change with the MA_{RT} film showing less defined and distinct grain boundaries. This implies that MA_{RT} treatment helps healing the grain boundary defects. The XRD measurement supports this with a drastic increase (2 orders of magnitude) in the peak intensity and much more uniform crystal orientation compared to the pristine

film. The FWHM was calculated to be 0.093˚ for the MA_{RT} film, similar to the pristine, which supports the observation of no significant change in grain size. The UV-Vis absorption and PL spectra also show a similar trend to the TIRMA films, with the PL showing a decrease in FWHM to 48.5 nm and a blue shift in the absorption band edge to about 1.6 eV. While the MA_{RT} film shows significant improvement in the film quality compared to the pristine films, it is less than what is achieved with the TIRMA treatment regarding the grain size and crystallinity.

The unprecedented enhancement in crystallinity of the TIRMA treated $MAPbI_3$ film is proposed to be a result of the slow growth controlled crystallization as opposed to the fast nucleation driven process. Figure 3.4 shows a schematic of the proposed mechanism of the TIRMA process. When the $MAPbI_3$ is exposed to the MA gas at room temperature, the colorless liquid phase $MAPbI_3$•xMA is immediately formed. When the chamber is put on the hot plate, a vertical temperature gradient is created up through the $MAPbI_3$ film. As the substrate temperature reaches the critical temperature (>55˚C), the colorless liquid phase begins to show a darker yellow color as seen in Figure 3.2b at 60 s. This yellow color can also be seen in images in Figure 3.1, particularly at 55˚C, 65˚C, and 75˚C samples. This yellow film is proposed to be an intermediate phase, $MAPbI_3$•*(x-y)*MA, resulted from the partial expulsion of MA molecules from the room temperature equilibrium state $MAPbI_3$•xMA. The equilibrium molar ratio *(x-y)* depends on the temperature, and more work is needed to characterize this intermediate state. When the substrate temperature rises above the critical temperature, continued expulsion of MA molecules leads to supersaturation, causing $MAPbI_3$ to nucleate on the surface. By maintaining a constant elevated temperature throughout the process, the $MAPbI_3$ nuclei

grow by continuous expulsion of MA. Such phase growth process can be considered as a typical case of cellular precipitation, $\gamma \rightarrow \alpha + \beta$, where the γ represents the liquid phase of $MAPbI_3$•*(x-y)*MA, α represents the solid precipitate of $MAPbI_3$, and β is the gas phase of MA. As the whole system remains in the MA atmosphere, the α and β are in equilibrium, meaning precipitation of $MAPbI_3$ and release of MA gas occur simultaneously at the expense of the original supersaturated phase of $MAPbI_3$•*(x-y)*MA. The diffusion distance remained short and unchanged during the phase growth process as seen from the approximately constant moving rate of the recrystallization front. Because the precipitation of $MAPbI_3$ is driven by expulsion of MA gas, the phase transition occurs at higher temperature, reverse to the other cellular precipitation processes, which are usually triggered by decreasing temperatures.

3.3 Spatial, Spectral, and Time Resolved Mapping of Large $MAPbI_3$ Crystal Grains

Spatially resolved PL response of thin films can give important information about the charge carrier dynamics of the material. Particularly, it is important to understand the role of the crystal grain and the grain boundary in $MAPbI_3$ thin films where potential losses are occurring. Confocal microscopy is an effective tool to understand the spatially resolved mechanisms of the PL response. Confocal microscopy works by tightly focusing an excitation beam onto the sample. The emission from the focused spot is then collected through the same objective, passes through a dichroic mirror, and finally passes through a pinhole before hitting the detector. A schematic of a confocal system is shown in Figure 3.5a. The main difference between a confocal microscope and a normal fluorescence

microscope is the pin hole, which acts to block off axis emission and effectively focuses the collection area to a very small and thin section of the material, as seen in in Figure 3.5b. By scanning the sample relative to the laser (or vice versa), detailed mapping of the PL response can be achieved. Confocal microscopy has been used to study the PL response of $MAPbI_3$ with small grained thin films to reveal important inter-grain processes.[17] For example, $MAPbI_3$ shows surprisingly non-uniform PL, and is expected to be a result of nonuniform distribution of defects between grains due to the fast crystallization deposition technique used. Under extended illumination, the films become more uniform due to migration of defect ions across grain boundaries leading to defect deactivation and an increase in PL. However, there has not been much research to understand the intra-grain PL response, largely because the grain sizes are typically on the order of the magnitude of diffraction limited focusing. This presents a unique opportunity to study intra-grain PL dynamics using the large grains from the TIRMA technique.

3.3.1 Experimental methods

3.3.1.1 Film fabrication

TIRMA treated $MAPbI_3$ films were fabricated on thin glass cover slips using the methods described in section 3.2.1.

3.3.1.2 Confocal mapping

A home-built confocal microscope was used for PL imaging. The film samples were loaded face up on to the sample stage. The excitation source was a 405 nm pulsed-

laser with a pulse width of 50 ps and a repetition rate between 2.5 MHz and 40 MHz. The laser was focused on the sample with an oil immersion objective with high numerical aperture (NA=1.4, 100x). Emission from the sample was filtered with a 488 LP filter, split with a 50/50 beam splitter, and focused on an avalanche photo diode (APD) for intensity and time resolved mapping and a monochrometer for spectrally resolved mapping. The system can be configured to scan the piezo scanner or the scanning mirror 2 (SM2). Piezo scanning is done with an Asylum AFM stage. The optional simultaneous AFM measurement was done with an Asylum AFM head and a silicon tip in tapping mode. SM2 was scanned by controlling the voltage of the SM2 mirror with a home built labview program. For high resolution AFM and confocal intensity images, scans are typically 288 by 288 pixel resolution. For hyperspectral or time resolved mapping, the resolution is limited to 64 by 64 pixel resolution to maintain sufficient collection time, about 0.1 s.

3.3.2 Results and discussion

3.3.2.1 Confocal/AFM mapping

The confocal microscope system is seen in Figure 3.5. The system can be run in two main modes: piezo scanning or laser scanning. In piezo scanning, the sample is scanned relative to the laser spot via piezo scanning stage. In this case, the laser remains stationary and excitation and collection remains on axis. This is also enables simultaneous AFM scanning to image the topography of the sample. Figure 3.6 shows the AFM and confocal microscopy images obtained on a single crystal grain. From Figure 3.6a and b, it is seen that the PL response is not uniform throughout the crystal grain.

Rather, the PL is strongest near the grain boundary. However, at the grain boundary, the PL abruptly decreases. This suggests that the grain boundary has significant nonradiative trapping centers.

To further understand the spatially resolved PL response, the spectral and time resolved images are analyzed. The spectral and time resolved mapping images are show in Figure 3.6c and e, respectively. Selected pixel spectra to represent different areas from of the crystal were plotted in Figure 3.6d, and the corresponding areas are marked on each image in Figure 3.6. Pixels 1, 2, and 3 represent the bulk crystal grain with low emission intensity, bulk crystal grain with high emission intensity, and grain boundary areas, respectively. For the spectrally resolved response, the peak wavelength was calculated through a Gaussian fit and mapped in Figure 3.6c. It is seen that the large grain has a fairly uniform response, but the grain boundary generally shows a red-shifted emission. Furthermore, it is noted that areas with higher emission intensity also show a red-shifted emission. The redshifted emission actually approaches the far field response seen in Figure 3.3c, and may be the result of local concentrations of shallow level defect states.[16] However, more experiments will be needed to understand the spectral shifting in the PL response

For the time resolved response, the PL decay was normalized and fit with a double exponential equation of the form:

$$I = A_1 exp\left(-\frac{t}{\tau_1}\right) + A_2 exp\left(-\frac{t}{\tau_2}\right) \quad [3.1]$$

where $\tau_{1/2}$ is the fast and slow decay time constant and $A_{1/2}$ is the fitting factor. For

mapping the time resolved response, the average τ was calculated by $\tau_{avg}=\alpha_1*\tau_1+\alpha_2*\tau_2$, where $\alpha_i = A_i*(A_1+A_2)^{-1}$. As seen in Figure 3.6e, the bulk grain area with lower emission intensity exhibited a longer τ_{avg} (~35ns) compared to the areas of high emission intensity and the grain boundary (~10-20 ns). Looking at the selected pixel decays in Figure 3.6f, pixel area 2 and 3, representing higher emission and grain boundary areas, respectively, show a clear biexponential decay with a strong fast initial decay followed by the slow decay. In pixel 1, however, the decay shows no significant initial fast decay component, leading to a monoexponential decay and longer τ_{avg}. Two proposed mechanisms may account for the differences in PL decay dynamics across the crystal grain areas. The first is that the fast decay component is the result of defects resulting in nonradiative recombination, or mediated trap state recombination. This is supported by the red shifted emission at the locations with the more prominent biexponential response. The second mechanism is that under low excitation intensity, $MAPbI_3$ is known to exhibit monoexponential decay as a result of the high concentration of shallow defects, which results in monomolecular recombination.[18] Under higher excitation intensities, the decay transitions into a biexponential decay as the trap states are filled and bimolecular recombination becomes the dominant recombination pathway. In this case, the low emission intensity in the bulk crystal grain would be the result of a local increase in trapping defects, and the areas with high emission intensity represent lower defect densities and therefore higher PL yield. However, this does not explain the blue shifted emission in the crystal grain. More work will be necessary to further explore these proposed mechanisms

3.3.2.2 SM2 laser scanning microscopy

Laser scanning confocal microcopy uses scanning galvanic mirrors to scan the excitation and collection area on the sample while the sample remains constant. Laser scanning in confocal microscopy relies on 4*f* optics as depicted in Figure 3.5b. In these systems, a scanning mirror and the back focal plane of the objective is separated by 2 identical lenses separated by the sums of their focal length, *f*: hence, 4*f*. The scanning mirror then changes the angle through the lenses, which changes the focus area laterally along the sample. As seen in Figure 3.5a, the confocal system used in these experiments utilizes a coupled double 4*f* configuration with two scanning mirrors: one in the excitation path (SM1), and one in the emission path (SM2). Scanning with SM1 scans the excitation spot along across the sample and the collected emission remains on axis, as described above. Alternatively, scanning SM2 changes the collection angle of the emitted light, which effectively changes the collection area on the sample, but maintains a constant excitation spot. This theoretically enables direct mapping of the free carrier diffusion length. Figure 3.7 shows the SM2 scanned image of the same crystal grain in Figure 3.6, focused close to (but not at) the center of the, grain near pixel 1. The SM2 scanned images shows an emission cone, that effectively represents the diffusion length of the crystal grain. By taking a cross section of the image, the peak can be fit. A Gaussian function showed relatively good fitting with a standard deviation of 1.5 μm and a FWHM of 3.4 μm. However, the peak also shows excellent fitting with a Lorenzian function with a FWHM of 2.8 μm. Since the SM2 scanning is hypothesized to directly image the diffusion length of charge carriers, the distribution should be Gaussian. Thus, the Lorenzian line shape suggests that there may be additional factors to consider in order

to understand these images. For instance, this method maps the lateral diffusion of the charge carriers, but surface recombination in the thin films would need to be accounted for to accurately model this system.

Based on Figures 3.6 and 3.7, rough estimates of the carrier life time and diffusion lengths (L_D) can be used to calculate the diffusion coefficient (D) through the relation:

$$D = \frac{L_D^2}{\tau} \qquad [3.2]$$

were L_D is estimated as the standard deviation (σ=1.5 μm) from the Gaussian fit of the SM2 PL peak, and τ is estimated to be a representative average lifetime in the area near pixel 1 of Figure 3.6e (τ~35 ns). This gives a diffusion coefficient of about 0.65 cm^2s^{-1}. This can be used to calculate the mobility, μ, through the Einstein relation:

$$\frac{D}{\mu} = \frac{kT}{q} \qquad [3.3]$$

where D is the diffusion coefficient, k is boltzman's constant, T is the temperature, and q is the elementary charge. This give an estimate of the mobility of μ = 25 $cm^2V^{-1}s^{-1}$. This value is relatively high for $MAPbI_3$ thin film samples and may be indicative of the high quality of the crystallized grain,[19] but still smaller than those measured for single crystal samples.[20-21] However, it is noted that this is a rough estimate based on preliminary data and further studies are needed to confirm this value.

3.4 Summary

In conclusion, a liquid-solid phase transition of $MAPbI_3 \bullet xMA$ into $MAPbI_3$ at elevated temperatures was revealed under constant MA gas atmosphere. This phenomenon was used to directly crystallize $MAPbI_3$ thin film with crystal grains on the order of tens of micrometers. The resultant film showed significantly enhanced crystallinity and reduced bulk crystal defects. This TIRMA process can be interpreted as a typical cellular precipitation, which allows for kinetic control (via temperature) of the phase growth in order to form large uniform crystalline domains. The films thus formed also afford complete and compact coverage across the substrate. Confocal microscopy experiments were performed and showed evidence of grain boundary-induced recombination of the TIRMA-treated large crystal grains, but strong nonuniform PL near to the grain boundaries. Using confocal piezo scanning and SM2 laser scanning, the charge carrier mobility was estimated to be around 25 $cm^2V^{-1}s^{-1}$ based on the preliminary and estimated charge carrier diffusion lengths and lifetimes. Future studies to control the nucleation and growth kinetics through more precise control of temperature and MA concentration, along with appropriate surface modification of the substrate is anticipated to further increase the size and quality of crystal grains and the uniformness of the film, which combined will facilitate the fabrication of high-efficiency photovoltaic devices.

3.5 References

1. Saliba, M.; Matsui, T.; Seo, J.-Y.; Domanski, K.; Correa-Baena, J.-P.; Nazeeruddin, M. K.; Zakeeruddin, S. M.; Tress, W.; Abate, A.; Hagfeldt, A.; Gratzel, M., Cesium-Containing Triple Cation Perovskite Solar Cells: Improved Stability, Reproducibility and High Efficiency. *Energy Environ. Sci.* **2016,** *9*, 1989-1997.

2. Eperon, G. E.; Burlakov, V. M.; Docampo, P.; Goriely, A.; Snaith, H. J., Morphological Control for High Performance, Solution-Processed Planar Heterojunction Perovskite Solar Cells. *Adv. Funct. Mater.* **2014,** *24*, 151-157.

3. Chen, Q.; Zhou, H.; Hong, Z.; Luo, S.; Duan, H. S.; Wang, H. H.; Liu, Y.; Li, G.; Yang, Y., Planar Heterojunction Perovskite Solar Cells via Vapor-Assisted Solution Process. *J. Am. Chem. Soc.* **2014,** *136*, 622-5.

4. Burschka, J.; Pellet, N.; Moon, S. J.; Humphry-Baker, R.; Gao, P.; Nazeeruddin, M. K.; Gratzel, M., Sequential Deposition as a Route to High-Performance Perovskite-Sensitized Solar Cells. *Nature* **2013,** *499*, 316-9.

5. Jeon, N. J.; Noh, J. H.; Kim, Y. C.; Yang, W. S.; Ryu, S.; Seok, S. I., Solvent Engineering for High-Performance Inorganic–Organic Hybrid Perovskite Solar Cells. *Nat. Mater.* **2014,** *13*, 897-903.

6. Xiao, M.; Huang, F.; Huang, W.; Dkhissi, Y.; Zhu, Y.; Etheridge, J.; Gray-Weale, A.; Bach, U.; Cheng, Y.-B.; Spiccia, L., A Fast Deposition-Crystallization Procedure for Highly Efficient Lead Iodide Perovskite Thin-Film Solar Cells. *Angew. Chem.* **2014,** *126*, 10056-10061.

7. Nie, W.; Tsai, H.; Asadpour, R.; Blancon, J.-C.; Neukirch, A. J.; Gupta, G.; Crochet, J. J.; Chhowalla, M.; Tretiak, S.; Alam, M. A.; Wang, H.-L.; Mohite, A. D., High-Efficiency Solution-Processed Perovskite Solar Cells with Millimeter-Scale Grains. *Science* **2015,** *347*, 522-525.

8. Zhou, Y.; Game, O. S.; Pang, S.; Padture, N. P., Microstructures of Organometal Trihalide Perovskites for Solar Cells: Their Evolution from Solutions and Characterization. *J. Phys. Chem. Lett.* **2015,** *6*, 4827-4839.

9. Bi, C.; Wang, Q.; Shao, Y.; Yuan, Y.; Xiao, Z.; Huang, J., Non-Wetting Surface-Driven High-Aspect-Ratio Crystalline Grain Growth for Efficient Hybrid Perovskite Solar Cells. *Nat. Commun.* **2015,** *6*, 7747.

10. Xiao, Z.; Dong, Q.; Bi, C.; Shao, Y.; Yuan, Y.; Huang, J., Solvent Annealing of Perovskite-Induced Crystal Growth for Photovoltaic-Device Efficiency Enhancement. *Adv. Mater.* **2014,** *26*, 6503-6509.

11. Zheng, Y. C.; Yang, S.; Chen, X.; Chen, Y.; Hou, Y.; Yang, H. G., Thermal-Induced Volmer–Weber Growth Behavior for Planar Heterojunction Perovskites Solar Cells. *Chem. Mater.* **2015,** *27*, 5116-5121.

12. Deng, Y.; Peng, E.; Shao, Y.; Xiao, Z.; Dong, Q.; Huang, J., Scalable Fabrication of Efficient Organolead Trihalide Perovskite Solar Cells with Doctor-Bladed Active Layers. *Energy Environ. Sci.* **2015,** *8*, 1544-1550.

13. Zhou, Z.; Wang, Z.; Zhou, Y.; Pang, S.; Wang, D.; Xu, H.; Liu, Z.; Padture, N. P.; Cui, G., Methylamine-Gas-Induced Defect-Healing Behavior of CH3NH3PbI3 Thin Films for Perovskite Solar Cells. *Angew. Chem., Int. Ed.* **2015,** *54*, 9705-9709.

14. Zhao, T.; Williams, S. T.; Chueh, C.-C.; deQuilettes, D. W.; Liang, P.-W.; Ginger, D. S.; Jen, A. K. Y., Design Rules for the Broad Application of Fast (<1 s) Methylamine Vapor Based, Hybrid Perovskite Post Deposition Treatments. *RSC Adv.* **2016,** *6*, 27475-27484.

15. Saidaminov, M. I.; Abdelhady, A. L.; Murali, B.; Alarousu, E.; Burlakov, V. M.; Peng, W.; Dursun, I.; Wang, L.; He, Y.; Maculan, G.; Goriely, A.; Wu, T.; Mohammed, O. F.; Bakr, O. M., High-Quality Bulk Hybrid Perovskite Single Crystals Within Minutes by Inverse Temperature Crystallization. *Nat. Commun.* **2015,** *6*, 7586.

16. Shao, Y.; Xiao, Z.; Bi, C.; Yuan, Y.; Huang, J., Origin and Elimination of Photocurrent Hysteresis by Fullerene Passivation in CH3NH3PbI3 Planar Heterojunction Solar Cells. *Nat. Commun.* **2014,** *5*, 5784.

17. deQuilettes, D. W.; Zhang, W.; Burlakov, V. M.; Graham, D. J.; Leijtens, T.; Osherov, A.; Bulović, V.; Snaith, H. J.; Ginger, D. S.; Stranks, S. D., Photo-Induced Halide Redistribution in Organic–Inorganic Perovskite Films. *Nat. Commun.* **2016,** *7*, 11683.

18. Stranks, S. D.; Burlakov, V. M.; Leijtens, T.; Ball, J. M.; Goriely, A.; Snaith, H. J., Recombination Kinetics in Organic-Inorganic Perovskites: Excitons, Free Charge, and Subgap States. *Phys. Rev. Appl.* **2014,** *2*, 034007.

19. Motta, C.; El-Mellouhi, F.; Sanvito, S., Charge Carrier Mobility in Hybrid Halide Perovskites. *Sci. Rep.* **2015,** *5*, 12746.

20. Lian, Z.; Yan, Q.; Gao, T.; Ding, J.; Lv, Q.; Ning, C.; Li, Q.; Sun, J.-l., Perovskite CH3NH3PbI3(Cl) Single Crystals: Rapid Solution Growth, Unparalleled Crystalline Quality, and Low Trap Density toward 108 cm–3. *J. Am. Chem. Soc.* **2016,** *138*, 9409-9412.

21. Shi, D.; Adinolfi, V.; Comin, R.; Yuan, M.; Alarousu, E.; Buin, A.; Chen, Y.; Hoogland, S.; Rothenberger, A.; Katsiev, K.; Losovyj, Y.; Zhang, X.; Dowben, P. A.; Mohammed, O. F.; Sargent, E. H.; Bakr, O. M., Low Trap-State Density and Long Carrier Diffusion in Organolead Trihalide Perovskite Single Crystals. *Science* **2015,** *347*, 519-522.

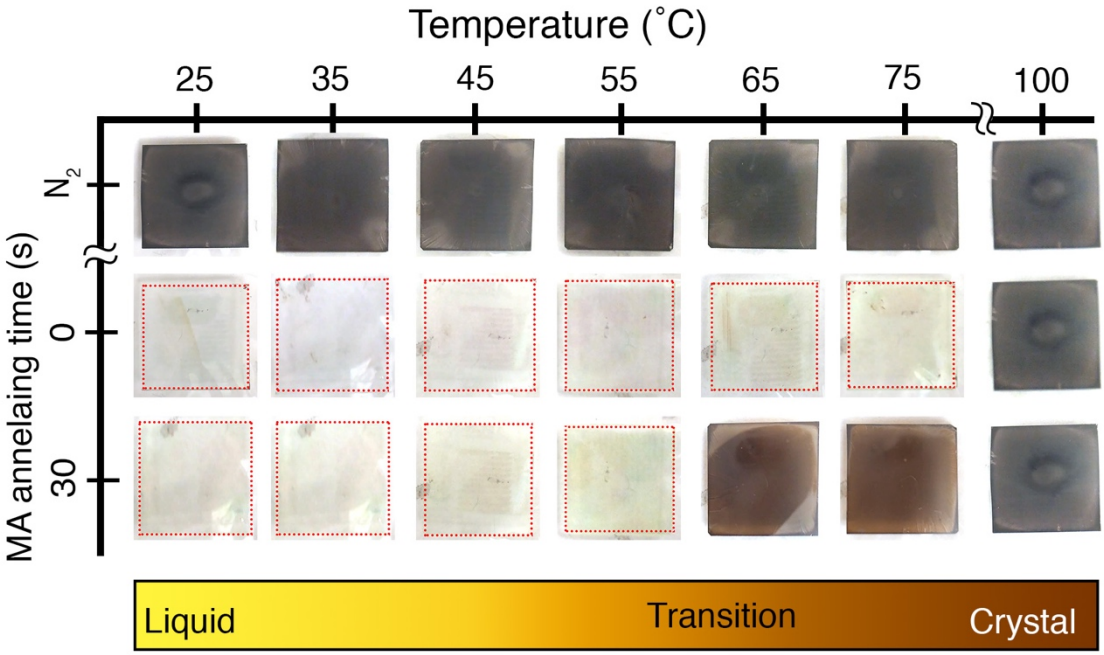

Figure 3.1. Temperature dependent annealing under MA gas atmosphere. Shown here are the images of seven $MAPbI_3$ coated glass substrates exposed to nitrogen or MA atmosphere maintained at a constant temperature. All images in a column represent the same sample at a constant temperature at different times throughout the experiment. Top Row: Images of the as deposited film after five minutes under flowing nitrogen atmosphere at the corresponding temperature. Middle Row: Image of the films immediately after exposure to MA atmosphere. Bottom Row: Images of the samples after 30 seconds under continual flowing MA atmosphere. The schematic at the bottom shows the proposed 1-D phase diagram of $MAPbI_3$ under a constant MA atmosphere. (Reproduced from Jacobs, D. L.; Zang, L., Thermally Induced Recrystallization of MAPbI3 Perovskite Under Methylamine Atmosphere: An Approach to Fabricating Large Uniform Crystalline Grains. *Chem. Commun.* **2016,** *52*, 10743-10746. Copyright (2016) the Royal Society of Chemistry.)

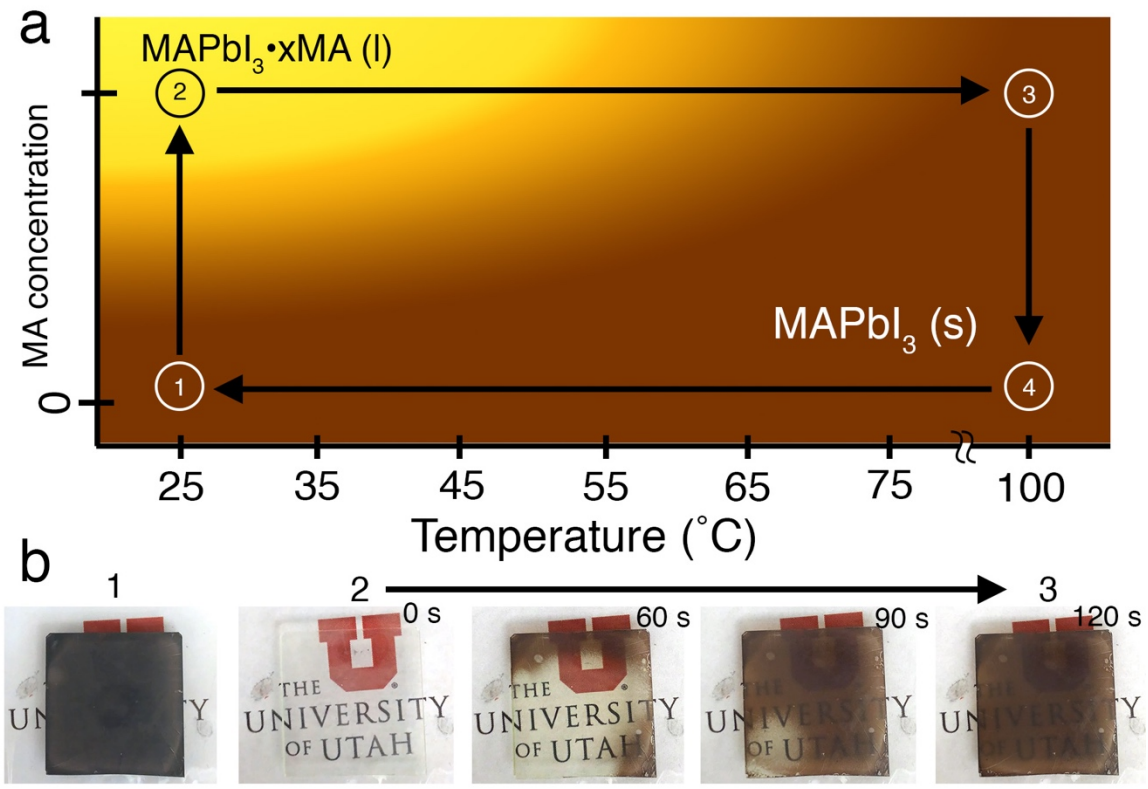

Figure 3.2. Experimental procedure of the TIRMA process. a) Proposed 2-D phase diagram showing the experimental path of TIRMA. b) in situ images of $MAPbI_3$ thin films during the TIRMA process. The $MAPbI_3$ film as prepared in ambient air (25˚C) was an opaque dark brown color (State 1). Immediately after exposure to MA atmosphere at room temperature, the film transformed to a colorless liquid state (State 2). The film (after exposed to MA for 30 s) was heated up to 100˚C, and during the 120 s heating it started to recrystallize, eventually forming the crystalline phase with a semitransparent brown color (State 3). After complete recrystallization, the MA atmosphere was purged with nitrogen for 2 min at 100˚C (State 4) followed by cooling to room temperature to form the final state. No significant difference after State 3 through the final state was found regarding either structure or morphology. (Reproduced from Jacobs, D. L.; Zang, L., Thermally Induced Recrystallization of MAPbI3 Perovskite Under Methylamine Atmosphere: An Approach to Fabricating Large Uniform Crystalline Grains. *Chem. Commun.* **2016,** *52*, 10743-10746. Copyright (2016) the Royal Society of Chemistry.)

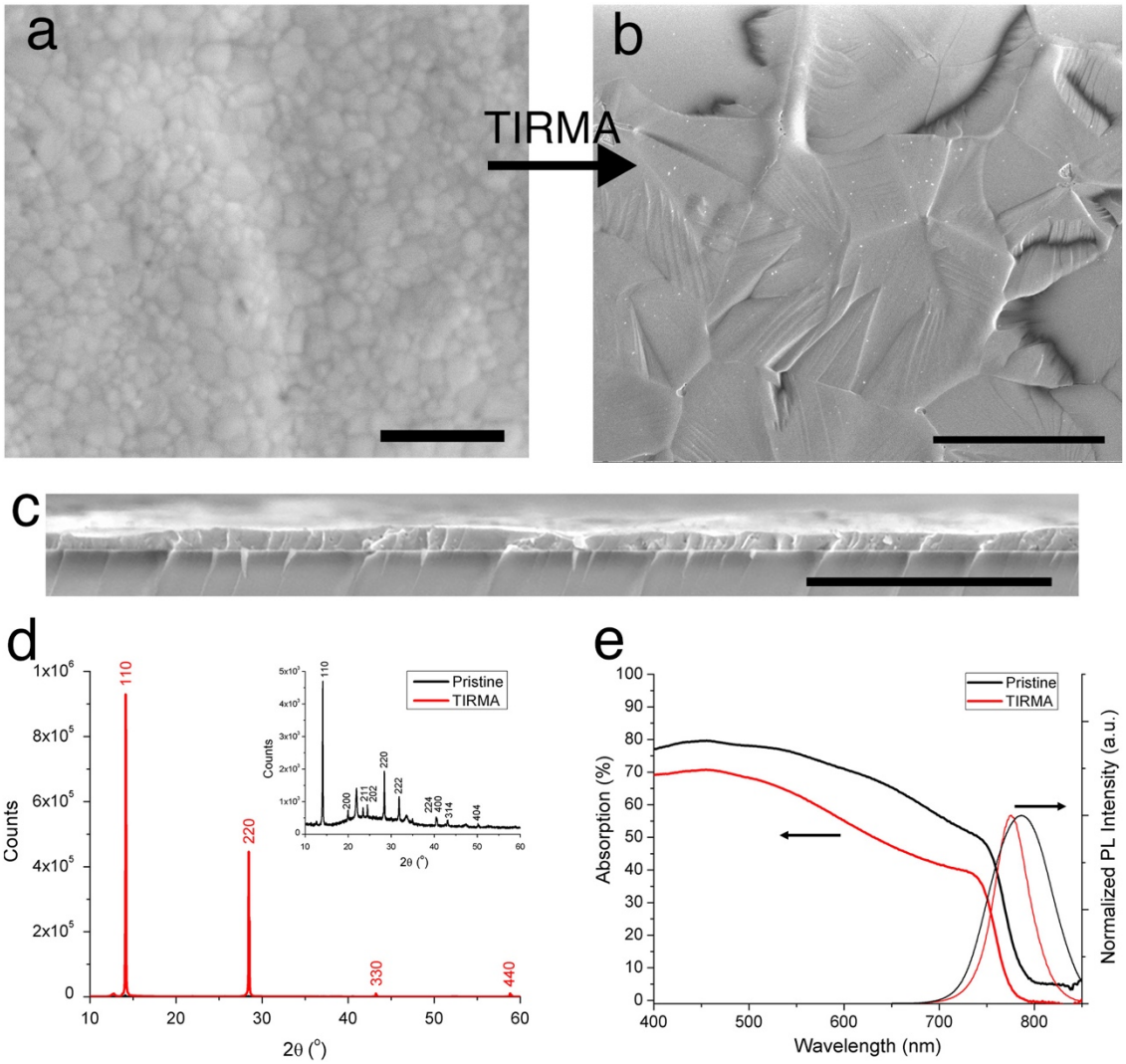

Figure 3.3. Results of the TIRMA process. SEM image of a) pristine and b) TIRMA treated $MAPbI_3$ showing the formation of large crystalline grains (scale bars are 1 µm and 20 µm, respectively). c) Cross sectional SEM image of TIRMA treated film (scale bar is 3 µm). d) XRD spectra of a pristine and a TIRMA treated $MAPbI_3$ film. The inset shows the isolated pristine $MAPbI_3$ film spectrum for comparison. e) Absolute absorption and normalized photoluminescence spectra of a pristine and a TIRMA treated $MAPbI_3$ film. (Adapted from Jacobs, D. L.; Zang, L., Thermally Induced Recrystallization of MAPbI3 Perovskite Under Methylamine Atmosphere: An Approach to Fabricating Large Uniform Crystalline Grains. *Chem. Commun.* **2016,** *52*, 10743-10746. Copyright (2016) the Royal Society of Chemistry.)

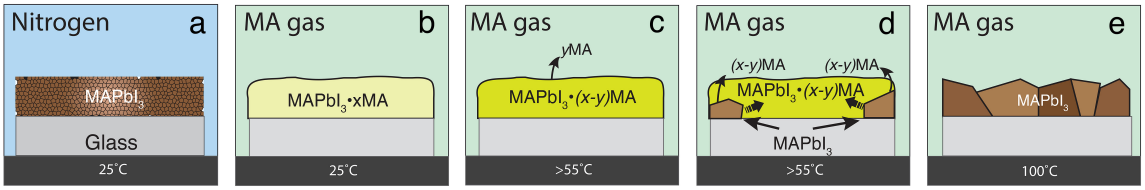

Figure 3.4. Schematic of proposed TIRMA mechanism leading to large crystalline grain film. a) As deposited $MAPbI_3$ film under nitrogen at room temperature. b) Exposure to MA at room temperature leading to $MAPbI_3$•*x*MA liquid phase. c) Increasing substrate temperature leading to partial expulsion of MA molecules. d) Nucleation of $MAPbI_3$ at the film edge followed by crystal growth via cellular precipitation as more MA molecules are expulsed from the film. e) Stable crystalline phase reached when all excessive MA molecules are released from the film. (Reproduced from Jacobs, D. L.; Zang, L., Thermally Induced Recrystallization of MAPbI3 Perovskite Under Methylamine Atmosphere: An Approach to Fabricating Large Uniform Crystalline Grains. *Chem. Commun.* **2016,** *52*, 10743-10746. Copyright (2016) the Royal Society of Chemistry.)

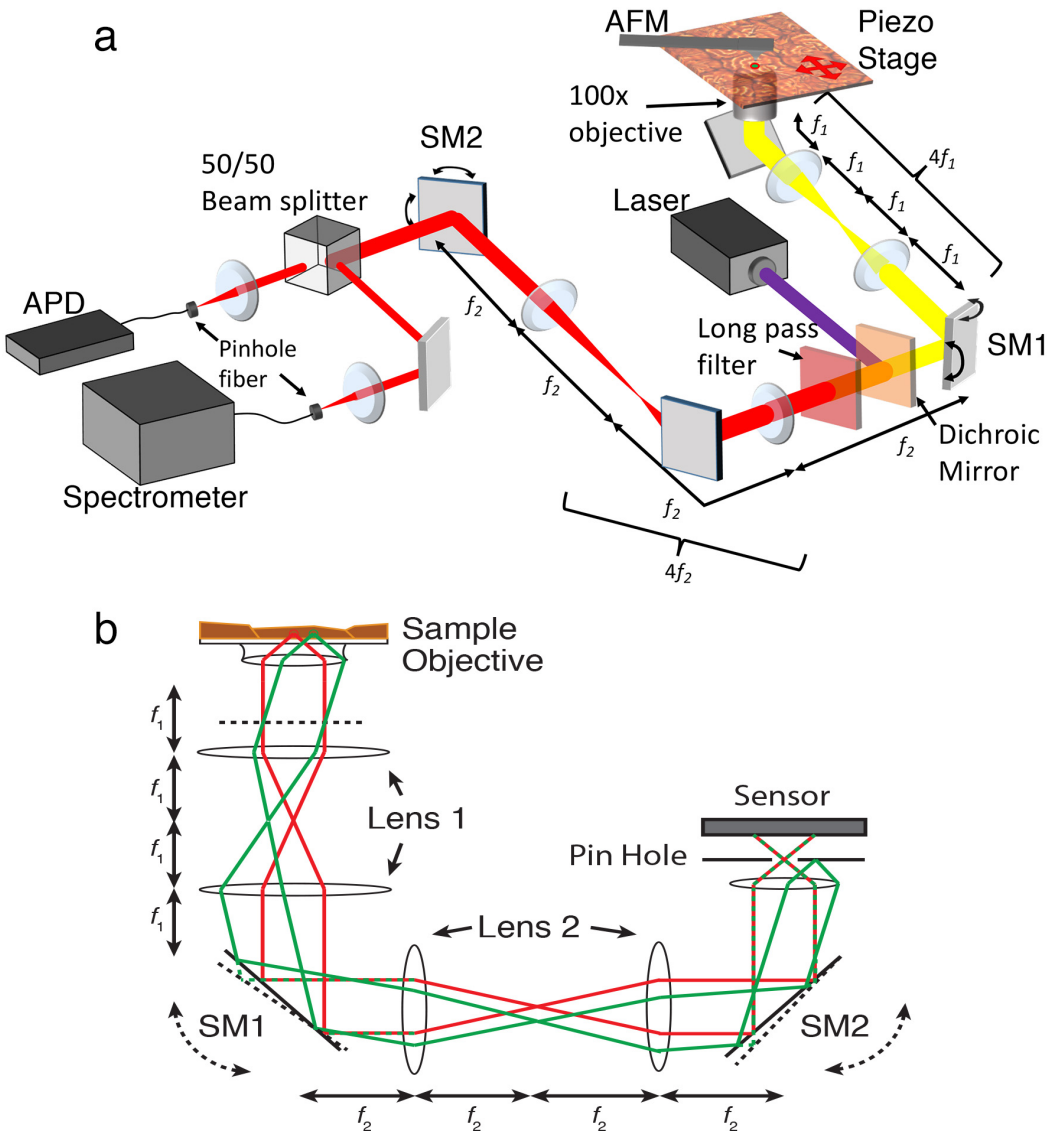

Figure 3.5. Schematic of confocal microscopy system with dual laser scanning capabilities. b) Schematic of the mechanism of confocal microscopy with two coupled 4*f* systems as depicted in Figure 3.6a. Red lines represents on-axis focusing where as green light represents off axis focusing. Dotted lines represent the off-axis correction by scanning SM1 or SM2. It is noted that, as seen in a), SM1 is in the excitation and collection path, whereas SM2 is only in the collection path, thus scanning SM2 only changes the collection focus area while the excitation remains on-axis.

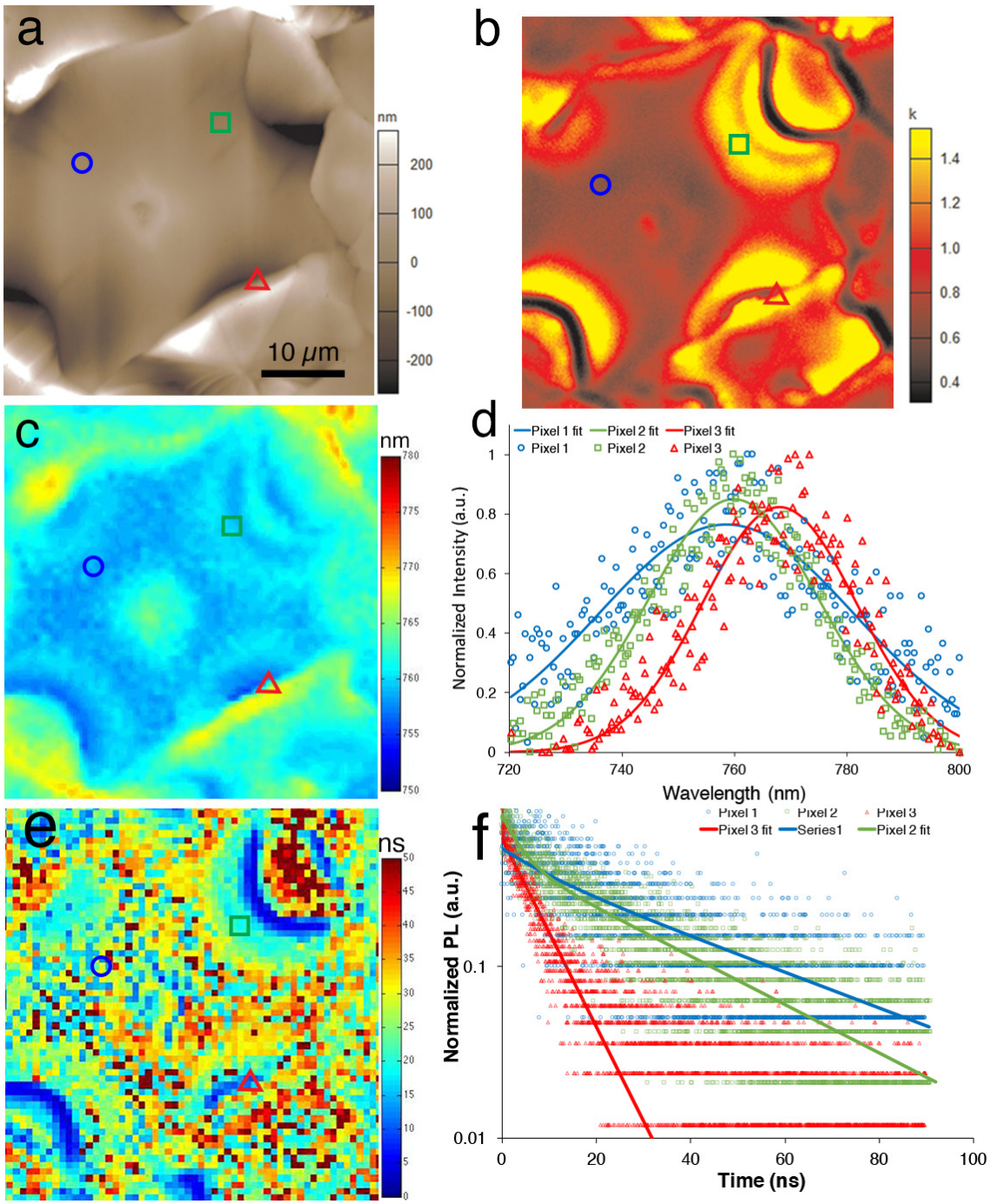

Figure 3.6. Confocal PL and AFM mapping results. a) High resolution AFM height image. b) High-resolution confocal PL image. c) Spectrally resolved confocal image showing the peak wavelength position. d) Time resolved time constant τ_2.

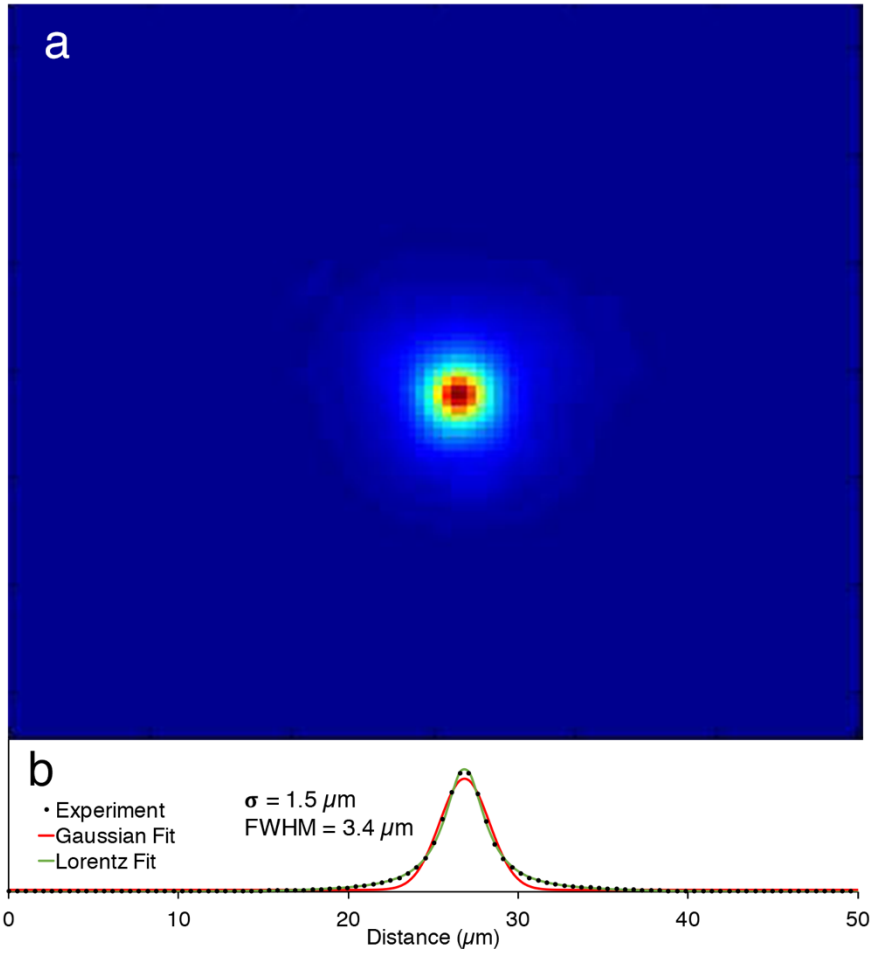

Figure 3.7. Confocal SM2scanned image of the same crystal grain in Figure 3.7. The excitation laser spot was focused near the middle of the crystal grain. b) Horizontal cross section of the PL emission spot (black circles) and the corresponding Gaussian (red) and Lorenzian (green) peak fits. The Gaussian fitting parameters, σ and the FWHM, are shown.

CHAPTER 4

COMPOSITIONAL AND MOPHOLOGICAL DEPENDENT SLOW TRANSEINT OPTOELECTRONIC RESPONSE OF $MAPBI_3$

4.1 Motivation

The intrinsic slow transient optoelectronic response (STOR) exhibited in $MAPbI_3$ thin films is a complex response that is dependent on the material's intrinsic defects. However, the strong ionic bonding of $MAPbI_3$ and the low enthalpy of formation leads to unique defect chemistry, which can drastically influence the optoelectronic response. The complex defect physics presents a challenge to bridge the theoretical understanding of defect formation and the experimentally observed response. There are two main defect-related mechanisms that are hypothesized to play a role in the STOR: migration of charged defect ions, and deep level trapping states in the bulk or at the gain surface/interface. The strong sensitivities of $MAPbI_3$ formation to several extrinsic factors, such as precursor composition and deposition technique, offers an extraordinary rage for defect engineering that can be potentially used as a tool to effectively probe the role of defect on the STOR. While theoretical calculations have shown that Schottky defects may actually be independent of precursor composition changes,[1-2] there is strong experimental evidence that composition can significantly change the defect properties of

the film. For example, a $MAPbI_3$ film can be tuned from n-type to p-type simply by changing the precursor solution composition ratio of PbI_2/MAI from 0.3 to 1.7, respectively.[3-4] In this case, low formation energy defects such as iodide vacancies (V_I) are expected to be n-type dopants, whereas MA and lead vacancies (V_{MA} and V_{Pb}) and iodide interstitials (I_i) are expected to be p-type compensating dopants.[4-5] Even small changes in the PbI_2/MAI precursor ratio of 5-10% can result in significant differences in the transient electronic response based on changes in the concentration and type of mobile shallow defects present.[6] Simplified understandings of defect formation reactions can give insight to the types of defects that may form across composition ranges.[6] For example, in stoichiometric samples, the low energy of formation for Schottky defects are expected to produce high concentrations of V_I, V_{MA}, and V_{Pb}. However, in PbI_2-rich and MAI-poor precursor samples, V_I and V_{MA} are expected to increase while V_{Pb} and Iodide interstitials (I_i) should be reduced, resulting in further n-type doping. Coincidentally, both V_I and V_{MA} are also expected to be mobile at room temperature, which may increase the ionic migration-related STOR.[7-9] Alternatively, PbI_2-poor and MAI-rich samples are expected to have an increase in V_{Pb} and I_i as well as V_I. Notice that for both reactions, V_I is formed, making it a consistent defect type across compositions resulting in a base level n-type doping. That being said, in MAI-excess samples, the increase in V_{Pb} and I_i should partially compensate the n-type doping. While I_i defects are anticipated to have similar ion migration effects as V_{MA} and V_I,[9-10] V_{Pb} is calculated to be immobile. Therefore, MAI-excess should show a decrease in the ion migration-dependent STOR. The formation of other defects with higher formation energies and deep-level trapping states must also be considered to fully analyze the STOR. For example, it was calculated that V_I

may not be stable, and degrade to form Pb-Pb covalent dimers with deep level trapping states. Similarly, Iodide trimers in areas with V_{Pb} or excess I_i may form resulting in mid-gap trapping centers.[11] Thus, this may lead MAI-excess to have higher concentrations of immobile deep-level trapping centers.

In addition to changing the composition of the $MAPbI_3$ films, postdeposition treatments have been shown to be important in controlling the defect levels, particularly surface and interface trapping centers. Larger grain sizes are hypothesized to have reduced ionic migration due to the expected grain boundary dominated ionic migration pathway.[10] Solvent annealing has been proposed as a route to decrease the bulk crystal defects through increased atomic and molecular reorientation leading to higher crystallinity and larger grain sizes.[12-13] Similarly, the thermal-induced recrystallization under methylamine atmosphere, introduced in Chapter 3, is a novel approach to understand how increasing crystallinity and grain size can affect the STOR.[14] Thus, increasing the crystallinity and grain size of the $MAPbI_3$ sample through TIRMA processing is anticipated to be a method to reduce the STOR.

Experimental studies to understand the effect of the film composition on the device performance has been studied and published.[6, 15] However, a major setback in these studies is the fact that the device architecture and deposition techniques are generally different across most studies. This leaves a large question as to the role of extrinsic factors that may also contribute to the different responses. Therefore, this study aims to use the platform developed in Chapter 1 as a standard platform to understand the role of composition and morphology on the STOR of $MAPbI_3$.

4.2 Experimental Methods

4.2.1 Materials preparation

Methylammonium iodide (MAI) was synthesized by reacting methylamine (40 wt. % in water) with equimolar amounts of HI (57 wt. % in water) in ambient atmosphere at 0 ˚C for 2 h. The solution was dried in a roto-evaporator at 75 ˚C. The precipitate was washed three times with diethylether and dried at 50 ˚C in a vacuum oven. PbI_2 (99.9985% metals basis) was obtained from Alfa Aesar and used as received. The $MAPbI_3$ precursor solution was made by dissolving MAI and PbI_2 in DMF at MAI:PbI_2 ratios of 0.65, 1.0 and 1.35 at 60˚C overnight.

4.2.2 Device fabrication

The interdigitated gold electrodes with 20μm electrode gap widths, 20 μm electrode widths, and 60 nm thick electrodes were deposited on 10 nm titanium adhesion layer on borofloat glass. The electrodes were cleaned by 30-s sonication in acetone, methanol, and isopropyl alcohol, respectively, followed by UV-ozone cleaning for 15 min. Clean electrodes were transferred to the spin coater under ambient conditions. 15 μL of the $MAPbI_3$ solution was spun onto the IDE at 1000 rpm for 10 s followed by 3000 rpm for 30 s. 50 μL of chlorobenze was dripped onto the spinning substrate 10 s after the start of the 3000 rpm spin cycle. The devices were immediately transferred to a hot plate and annealed at 100 ˚C for 20 min. The completed devices were then stored in a vacuum desiccator in the dark for at least 12 h before testing. For the TIRMA treated samples, the as deposited $MAPbI_3$ coated electrodes films were loaded into the sample chamber at room temperature and purged with nitrogen for 5 min. Methylamine gas (MA) was

introduced by routing the nitrogen carrier gas through the headspace of a 100 mL two-necked round bottom flask with 5mL of a 33 wt% MA solution in ethanol. After 30 s of MA exposure at room temperature, the chamber was placed onto the preheated hot plate at 100˚C. When the $MAPbI_3$ film completely crystallized (~2 min) the chamber was purged with nitrogen for 2 min while still on the hotplate. Then the chamber was removed from the hotplate and allowed to cool to room temperature before removing the samples and storing in a vacuum desiccator.

4.2.3 STOR characterization

Optical measurements were done with a Leica fluorescence microscope and the electrical characterization was done in situ with a Keithley 6485 piccoammeter controlled through a homemade labview program. Devices were placed in a homemade chamber under Argon flow and purged for 15 min in the dark. 560 nm excitation light (mercury lamp filtered through a band pass filter) was turned on under 0 applied voltage and the PL response to steady state was recorded for 10 min. The electric field dependent response was recorded under an applied bias for 100 s, followed by monitoring the recovery response at 0 V for another 100 s. Each measurement was performed on a separate untested area of the same IDE device.

4.3 Results and Discussion

4.3.1 Compositional dependence

4.3.1.1 Identifying compositional dependent STOR trends

For each composition tested, 12 measurements were taken across 3 devices, normalized, and averaged for comparison. Figure 4.1a shows a representative SEM image of the $MAPbI_3$ films deposited across the IDE electrodes. Figure 4.1b-c shows the averaged optoelectronic response for each composition. Figure 4.1b shows the PL response to light excitation with no electrical bias, where the light is turned on at t = 0s. Figure 4.1c shows the electric field dependent PL response to a 1 $V\mu m^{-1}$ electrical bias. The voltage is turned on at t=0 s and turned off at t = 100 s. Figure 4.1d shows the corresponding current measurements with the left panel showing the response to the applied voltage, and the right panel is rescaled to show the low current recovery after the bias was removed. It is clear from Figure 4.1 that the change in precursor composition results in a significant change in the STOR. Beginning with Figure 4.1b, which shows the PL response toward steady state under no applied field, the response varies from a very small change in PL over time (0.65), to a significant decay (1.0), to a significant increase in PL (1.35) with increasing MAI concentration. In Figure 4.1c, the general PL response to electrical bias is also strongly dependent on the precursor composition. The 0.65 samples show a fast PL decay under the electrical bias, which increases slowly over time, followed by a fast recover to a steady state. The 1.0 samples showed a unique decay-peak-decay response under bias, followed by a nominal recovery when the bias was removed. The 1.35 samples showed a monotonic slow decay under applied bias, followed by a slower PL recovery rise toward a steady state value. The corresponding current

measurements give some more insight into the compositional-dependent STOR variations. Interestingly, despite the significantly different PL responses to the applied bias across compositions, all of the current transients to the applied bias show a similar decay, albeit with different rates and slightly different decay magnitudes. The current recovery after the applied bias was removed was slightly more telling. All samples showed a negative current when the bias was removed. The 0.65 samples showed a small and stable negative current. Alternatively, the 1.0 sample showed a larger negative current that slowly decayed over time. Finally, the 1.35 sample showed a strong negative current, but a very fast decay toward zero.

From Figure 4.1, some qualitative observations can be made to understand the role of precursor composition. First, the 0.65 samples showed the most stable and fastest transient responses across all measurements. It is proposed that this is partially attributed to the formation of excess PbI_2 on the surface of the small crystal grains. The PbI_2 acts as a natural passivation layer for $MAPbI_3$ potentially reducing surface trapping.[15] Furthermore, in PbI_2 excess samples, the V_{Pb} and I_i defects should be suppressed and therefore have a smaller concentration of deep level trapping defects.[11] However, at this composition, there should still be excess mobile V_{MA} and V_I defects in the film. The slow increase in the PL and the decay in the current under the applied bias, as well as the steady negative current after the bias was removed, suggest that there is slow ion migration, but it might be relatively small compared to the other compositions. While it is known that PbI_2 can also exhibit halide ion conduction, the PbI_2 layer is expected to slow V_{MA} migration.

Alternatively, the MAI excess 1.35 samples show very different responses. The

response to light soaking results in a slow increase in the PL. This is proposed to be a result of the increased concentrations of V_{Pb} and V_I degrading into the stable covalent trapping states.[11] Therefore, the increase in PL is the result of slow trap filling and/or trap deactivation under light.[16-17] Increase in trapping states at this composition is expected to lead to the observed slower monotonic transient response to the application and removal of the electrical bias. However, the weak recovery of the PL after the bias is removed suggests that there might also be significant degradation, and/or significant ion migration leading to the formation of an internal electrical field. The current response showing the decay in current after applying the bias, as well as the negative current after the removal of the bias, is evidence of fast ion migration. However, it has also been shown experimentally that migration of MA-defects can enhance the degradation kinetics. Theoretically, the MA_i interstitial defect is not expected to have a low formation energy or high mobility,[8-9] but there is experimental evidence that MA does in fact migrate and lead to degradation to PbI_2.[18] Thus, for 1.35 samples, it is proposed that the increased trapping centers and migration of MA_i leads to the slower transient responses and overall degradation of the PL and possibly $MAPbI_3$ material itself.

Finally, the 1.0 samples show the greatest variability in responses. The effect of light soaking results in a strong PL decrease over time. The reason for a PL decrease is not known, as most $MAPbI_3$ samples in the literature show an increase in the PL over time.[16] However, stoichiometric samples are expected to show significant Schottky defects, leading to high concentrations of V_{MA}, V_{Pb}, and V_I.[1-2, 19] Thus, it may be that the light excitation, or subsequent heating, results in increased concentrations of defects due to the low enthalpy of formation for Schottky defects. Under the applied bias, the unique

decay-peak-decay, or "humped," response may be the result of complex interplay between ion migration, leading to field compensation, possible defect deactivation due to migration of defects throughout the sample, or degradation. When the bias was removed, the lack of significant PL recovery suggests that the sample may have degraded, but the stronger and stable negative current suggests that migration of V_{MA} did contribute to the response. The large variability in the response to light and electrical bias makes it challenging to draw conclusions at this point in the study.

4.3.1.2 Light intensity dependence

To further understand the role of compositional changes on the STOR, the experiments were repeated across a range of light intensities with a constant electric field of 1 $V\mu m^{-1}$ as seen in Figure 4.2. The excitation intensity was varied to span an order of magnitude from about 100$mWcm^{-2}$ to 1000 $mWcm^{-2}$. For comparison, simulated AM1.5 sunlight has a power of 100 $mWcm^{-2}$, so this light range represents intensities above operating solar cells. It is noted that all of the above mentioned experiments in this chapter have been done at a light intensity of 300 mW/cm^{-2}. The effect of light intensity on the already complex STOR response across compositions adds further complexity to the analysis that will need more follow up and supplementary experiments to fully understand. However, there are some notable qualitative trends that suggest important correlations to the mechanisms proposed above. Starting with PbI_2 excess 0.65 samples, the light intensity has little to no effect on the light soaking response, supporting the hypothesis of low trapping defects as a result of a PbI_2 passivation layer and low concentrations of Pb-based deep level defects. (It is noted that for all composition tests,

the first response (lowest light intensity) was typically an outlier for the light soaking studies. This is anticipated to be a result of the testing procedure where all studies were done on different areas of the same IDE. While the main mechanisms described in this and the above sections are proposed to be light dependent, there might be some small unforeseen dark current response that slightly alters subsequent measurements.) For the response to the applied voltage, increasing light intensity showed general increase in the rate of PL rise. This PL rise under bias is anticipated to be from field compensation due to drifting V_I or V_{MA} defects. Thus, the increase in the light intensity leads to a decrease of the activation energy of the hopping-limited defect migration. Interestingly, the "humped" response originally only seen in the 1.0 samples in Figure 4.1, is also observed in the 0.65 samples, particularly at the lowest two light intensities. Increasing the light intensity seemingly shifted this feature toward earlier times until the maximum light intensity showed only a minimum and recover response. This light intensity-dependent rate of this unique feature suggests that it is a result of ion migration, but more experiments will be needed to confirm this hypothesis.

For the MAI-excess 1.35 samples, the response showed more significant light intensity dependence. For example, the light soaking showed a strong dependence on light intensity, with the rate of PL rise increasing with increasing light intensity. This correlates well with the proposed mechanism of trap filling/deactivation leading to the PL rise, and thus the increased light intensity increases the trapping/deactivation rate. This is supported in the electrical bias response as seen as a reduction of the PL increase under bias, expected to be from ion migration, and transition into a single slow monotonic decay representative of a trapping mechanism.

The stoichiometric 1.0 samples again show the largest variability across light excitations. In the light soaking experiments, the 1.0 samples showed significant variation in light intensity. This is proposed to be the result of light-dependent defect formation and activation leading to the change in PL quenching. The electrical bias response again showed a prominent "humped" feature under applied bias. Similar to the 0.65 samples, this feature was pushed to shorter times with increasing light intensity, supporting the hypothesis that it is a result of ion migration. Furthermore, with increasing light intensity, the final PL response after recover under no applied bias showed a decreasing trend, further suggesting that higher light intensities either increase the defect densities, or decrease the activation energy for migration.

4.3.1.3 Electric field dependence

Finally, the STOR was further probed by changing the electric field strength under a constant light intensity of 300 mW/cm^{-2} across a range from 0.1 $V\mu m^{-1}$ to 2 $V\mu m^{-1}$ as seen in Figure 4.3. Similar to the light intensity dependent studies, these studies give a wealth of information, but further studies and supplementary experiments will be required fully understand this system. However, there are clear qualitative trends that give crucial insight into the working mechanisms that will be used to correlate the composition dependence to the observed STOR.

First, it is noted that across all compositions, the light soaking did not show significant deviation across measurements. This is significant as it further supports the proposed light-dependent mechanisms in the previous section. Since the transient responses to the light soaking tests do not deviate across measurements, and have been

described above, only the electrical bias dependent response will be discussed further.

In the PbI_2-excess 0.65 sample, PL decay under bias is strongly dependent on the applied electric field strength. Interestingly, there is no PL response to the weak applied field of 0.1 $V\mu m^{-1}$ despite having a measurable current response (not shown). One explanation for this is that the PL response under bias relies on the assumption that the free carrier life time of the $MAPbI_3$ thin film is longer than the drift time of the carriers under the applied electric field. This suggests that in the 0.65 sample, the potential passivating layer of PbI_2 may reduce the charge carrier life time, or the charge carrier mobility. This will be investigated further in future studies. At biases lager than 0.1 $V\mu m^{-1}$, there is a clear PL response. At 0.5 $V\mu m^{-1}$, the unique "humped" PL response feature again appears. The rate of this feature is increased with increasing voltage. Furthermore, the rate of the PL rise after the minimum under the bias is also increased with increasing field strength. These observations further support the proposed ion migration mechanism present in these samples under an applied bias.

For the MAI excess 1.35 sample, there was a clear PL response for all applied biases. This suggests that at this composition, either the mobility of free charge carriers, or the life time of the charge carriers is enhanced relative to the 0.65 sample. Increasing the applied bias further increases the magnitude of the PL quench under bias. Also, above 1 $V\mu m^{-1}$, the PL response transitions from a monotonic decay, to a minimum-rise response, suggesting that ion migration is occurring at the higher biases. The PL recover dynamics showed a trend of a slow PL rise, which is explained with a defect trapping mechanism. However, the PL response for the 0.1 $V\mu m^{-1}$ exhibits a much faster decay and recover. This might suggest that there is an electrical bias-dependent defect

activation process above 0.1 $V\mu m^{-1}$ that leads to the strong trapping response at higher applied biases.

Again, the stoichiometric 1.0 samples showed the largest variability across the compositions. Similar to the 0.65 sample, the 0.1 $V\mu m^{-1}$ did not show any PL response. At larger biases, the unique PL hump feature appeared, and like the 0.65 sample, showed a strong dependence on the applied field strength. Most notably, however, at fields larger than 1 $V\mu m^{-1}$, the PL rise was significantly more significant and approaching the initial PL value before the bias was applied. Even more interesting, when the bias was removed, the PL actually increased to above the initial value and then slowly decayed. The reason behind this response is still under investigation, but one potential hypothesis is that ion migration may be leading to degradation to PbI_2, which acts to passivate surface traps. Either way, the general observed trends further support the proposed mechanism in the previous sections of ion migration under the applied electrical bias.

4.3.2 Morphological dependence

$MAPbI_3$ was deposited onto IDEs and processed with the TIRMA treatment as described in Chapter 3. Figure 4.4a shows an SEM image of the device showing the large grains around 10-20 μm in size and uniform deposition across the device. The grains are on the same scale as the electrode gap distances, which is in sticking difference to the as-deposited films where charge carrier transport occurred across significant lengths of grain boundary. Thus, these studies should give a better insight to the bulk crystal grain response and not limited by grain boundaries.

Figure 4.4b-d shows the STOR response of the TIMRA treated samples, with

Figure 4.4b showing the PL response to the light soaking at zero applied bias, Figure 4.4c showing the PL response to the applied voltage, and Figure 4.4d showing the corresponding current response to the applied bias. The TIRMA films show features similar, as well as contrasting to the as-deposited samples discussed above. For example, the PL response to light soaking of the TIRMA samples showed a similar response to the stoichiometric 1.0 as-deposited samples: a decrease in the PL toward a steady state value. In Figure 4.4c, there is a small PL response to the weakest applied field of 0.05 $V\mu m^{-1}$, which suggests an improvement in either the charge carrier lifetime or the charge carrier mobility. At larger applied fields, the PL response showed a very fast transient response to a stable value. The corresponding current response to the applied bias in Figure 4.4d also shows a much more stable value with the final current value decaying to at most about 75% of the peak value for the largest applied bias, compared to over 50% decay for the as-deposited samples. However, significant differences with the TIRMA sample is seen in the recovery response when the bias was removed. At biases greater than 0.05 $V\mu m^{-1}$, the normalized PL quickly jumped to a value larger than 1 and then quickly decayed back toward 1. This is similar to what was observed in the as-deposited films at large biases, but unlike those responses, the TIRMA samples did not show a steady and significant increase in the PL under the bias. The corresponding current response when the bias was removed showed an increasing stable negative current, suggesting that the larger bias is able to induce an ion migration mechanism even in the large highly crystalline grains. However, the exact mechanism of the PL increase is not understood from these initial studies. Overall, the TIRMA samples did show a more stabilized response with faster transients as expected for the higher crystallinity and reduced grain

boundary area films.

4.4 Summary

The STOR was monitored across changes to the $MAPbI_3$ composition and morphology. By tuning the precursor ratio of MAI:PbI_2 around 1.0, the defect properties were controlled. The optoelectronic response on the IDE devices was monitored to light and electrical biases. Distinct STOR trends were observed for each composition supporting the hypothesis that the defect formation can be controlled with precursor solution composition. The STOR was further probed by testing the excitation light intensity dependence and electric field strength dependence. Based on these studies, important quantitative correlations to STOR mechanisms were made. For example, it is proposed that PbI_2-excess compositions result in faster and more stable responses due to the formation of PbI_2 surface passivation and a reduction of Pb-based deep level trapping centers. Alternatively, MAI-excess samples showed slower transient responses and irreversible responses that are proposed to be the result of increased concentrations of deep-level defect trapping centers and MA-based ion migration leading to degradation. Finally, the stoichiometric samples showed the most variability in the responses that is proposed to be the result of low formation energy Schottky defects that lead to an even more complex STOR response. By using the novel TIRMA annealing technique introduced in Chapter 3, the STOR was significantly reduced and exhibited unique responses not seen in the as deposited samples. Thus, the increased crystallinity and reduced grain boundary area should be an effective approach to reducing the STOR in $MAPbI_3$-based devices. Overall, the IDE devices represent a very effective platform to

study and probe the underlying mechanism of the STOR in $MAPbI_3$.

4.5 References

1. Ming, W.; Chen, S.; Du, M.-H., Chemical Instability Leads to Unusual Chemical-Potential-Independent Defect Formation and Diffusion in Perovskite Solar Cell Material CH3NH3PbI3. *J. Mater. Chem. A* **2016,** *4*, 16975-16981.

2. Yang, J.-H.; Yin, W.-J.; Park, J.-S.; Wei, S.-H., Self-Regulation of Charged Defect Compensation and Formation Energy Pinning in Semiconductors. *Sci. Rep.* **2015,** *5*, 16977.

3. Wang, Q.; Shao, Y.; Xie, H.; Lyu, L.; Liu, X.; Gao, Y.; Huang, J., Qualifying Composition Dependent P and N Self-Doping in CH3NH3PbI3. *Appl. Phys. Lett.* **2014,** *105*, 163508.

4. Yin, W.-J.; Shi, T.; Yan, Y., Unusual Defect Physics in CH3NH3PbI3 Perovskite Solar Cell Absorber. *Appl. Phys. Lett.* **2014,** *104*, 063903.

5. Buin, A.; Pietsch, P.; Xu, J.; Voznyy, O.; Ip, A. H.; Comin, R.; Sargent, E. H., Materials Processing Routes to Trap-Free Halide Perovskites. *Nano Lett.* **2014,** *14*, 6281-6286.

6. Yu, H.; Lu, H.; Xie, F.; Zhou, S.; Zhao, N., Native Defect-Induced Hysteresis Behavior in Organolead Iodide Perovskite Solar Cells. *Adv. Funct. Mater.* **2016,** *26*, 1411-1419.

7. Leguy, A. M. A.; Frost, J. M.; McMahon, A. P.; Sakai, V. G.; Kockelmann, W.; Law, C.; Li, X.; Foglia, F.; Walsh, A.; O'Regan, B. C.; Nelson, J.; Cabral, J. T.; Barnes, P. R. F., The Dynamics of Methylammonium Ions in Hybrid Organic–Inorganic Perovskite Solar Cells. *Nat. Commun.* **2015,** *6*, 7124.

8. Eames, C.; Frost, J. M.; Barnes, P. R. F.; O'Regan, B. C.; Walsh, A.; Islam, M. S., Ionic Transport in Hybrid Lead Iodide Perovskite Solar Cells. *Nat. Commun.* **2015,** *6*, 7497.

9. Azpiroz, J. M.; Mosconi, E.; Bisquert, J.; De Angelis, F., Defect Migration in Methylammonium Lead Iodide and its Role in Perovskite Solar Cell Operation. *Energy Environ. Sci.* **2015,** *8*, 2118-2127.

10. Shao, Y.; Fang, Y.; Li, T.; Wang, Q.; Dong, Q.; Deng, Y.; Yuan, Y.; Wei, H.; Wang, M.; Gruverman, A.; Shield, J.; Huang, J., Grain Boundary Dominated Ion Migration in Polycrystalline Organic-Inorganic Halide Perovskite Films. *Energy Environ. Sci.* **2016,** *9*, 1752-1759.

11. Agiorgousis, M. L.; Sun, Y.-Y.; Zeng, H.; Zhang, S., Strong Covalency-Induced Recombination Centers in Perovskite Solar Cell Material CH3NH3PbI3. *J. Am. Chem. Soc.* **2014,** *136*, 14570-14575.

12. Xiao, Z.; Dong, Q.; Bi, C.; Shao, Y.; Yuan, Y.; Huang, J., Solvent Annealing of Perovskite-Induced Crystal Growth for Photovoltaic-Device Efficiency Enhancement. *Adv. Mater.* **2014,** *26*, 6503-6509.

13. Nie, W.; Tsai, H.; Asadpour, R.; Blancon, J.-C.; Neukirch, A. J.; Gupta, G.; Crochet, J. J.; Chhowalla, M.; Tretiak, S.; Alam, M. A.; Wang, H.-L.; Mohite, A. D., High-Efficiency Solution-Processed Perovskite Solar Cells with Millimeter-Scale Grains. *Science* **2015,** *347*, 522-525.

14. Jacobs, D. L.; Zang, L., Thermally Induced Recrystallization of MAPbI3 Perovskite Under Methylamine Atmosphere: An Approach to Fabricating Large Uniform Crystalline Grains. *Chem. Commun.* **2016,** *52*, 10743-10746.

15. Chen, Q.; Zhou, H.; Song, T.-B.; Luo, S.; Hong, Z.; Duan, H.-S.; Dou, L.; Liu, Y.; Yang, Y., Controllable Self-Induced Passivation of Hybrid Lead Iodide Perovskites toward High Performance Solar Cells. *Nano Lett.* **2014,** *14*, 4158-4163.

16. Fu, X.; Jacobs, D. A.; Beck, F. J.; Duong, T.; Shen, H.; Catchpole, K. R.; White, T. P., Photoluminescence Study of Time- and Spatial-Dependent Light Induced Trap De-Activation in CH3NH3PbI3 Perovskite Films. *Phys. Chem. Chem. Phys.* **2016,** *18*, 22557-22564.

17. Tian, Y.; Peter, M.; Unger, E.; Abdellah, M.; Zheng, K.; Pullerits, T.; Yartsev, A.; Sundstrom, V.; Scheblykin, I. G., Mechanistic Insights into Perovskite Photoluminescence Enhancement: Light Curing with Oxygen can Boost Yield Thousandfold. *Phys. Chem. Chem. Phys.* **2015,** *17*, 24978-24987.

18. Leijtens, T.; Hoke, E. T.; Grancini, G.; Slotcavage, D. J.; Eperon, G. E.; Ball, J. M.; De Bastiani, M.; Bowring, A. R.; Martino, N.; Wojciechowski, K.; McGehee, M. D.; Snaith, H. J.; Petrozza, A., Mapping Electric Field-Induced Switchable Poling and Structural Degradation in Hybrid Lead Halide Perovskite Thin Films. *Adv. Energy Mater.* **2015,** *5*, 1500962.

19. Walsh, A.; Scanlon, D. O.; Chen, S.; Gong, X. G.; Wei, S.-H., Self-Regulation Mechanism for Charged Point Defects in Hybrid Halide Perovskites. *Angew. Chem., Int. Ed.* **2015,** *54*, 1791-1794.

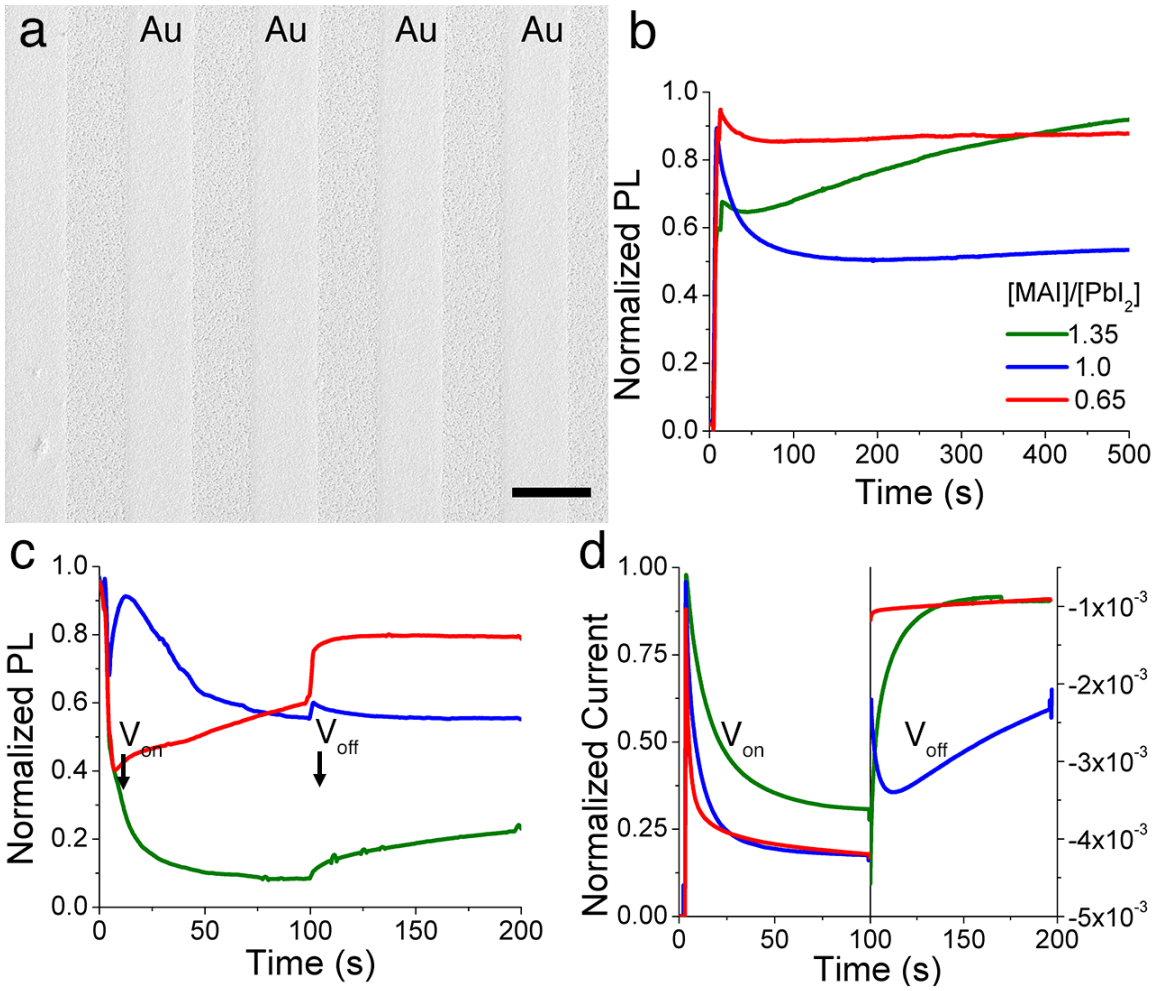

Figure 4.1. Compositional dependent STOR trends. a) SEM image of 1.0 sample representative of the devices used for the compositional dependent studies. Scale bar is 20 μm. b) Normalized PL response to light excitation during light soaking studies under zero applied bias. c) Normalized PL response to the application of a 1 $V\mu m^{-1}$ electric field under constant illumination. The bias is turned on about 5 s and turned off at about 100 s. d) Normalized current response to the application of an applied bias. The left column shows the current when the bias is applied, and the right column shows the recovery after the bias is removed. The right column is rescaled to the right axis. The red, blue, and green line color represents a [MAI]/[PbI_2] precursor ratio of 0.65, 1.0, and 1.35, respectively.

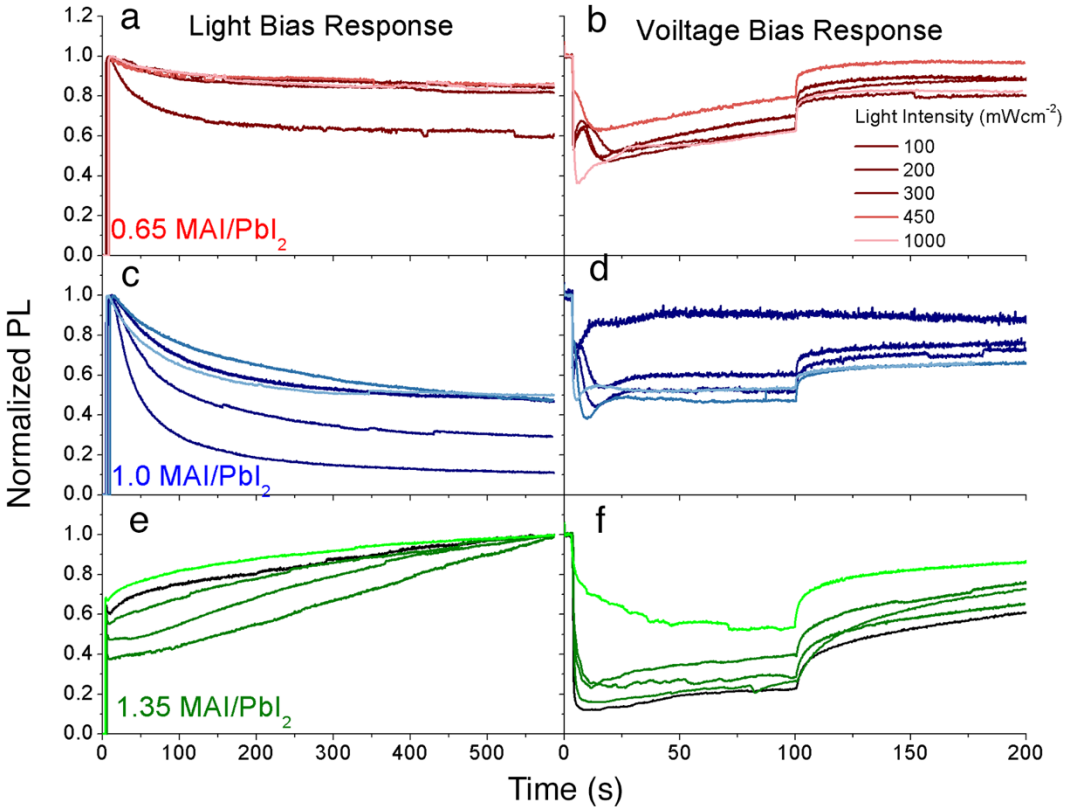

Figure 4.2. Light intensity-dependent measurements of the STOR across $MAPbI_3$ compositions. Light intensities range from 100 to 1000 $mWcm^{-2}$ represented as increasing color brightness. Normalized PL response to light soaking experiments (a, c, e) and application of an electrical bias (b, d, f) of $MAPbI_3$ films with precursor composition ratios of [MAI]/[PbI_2] equal to 0.65 (a-b, red lines), 1.0 (c-d, blue lines), and 1.35 (e-f, blue lines).

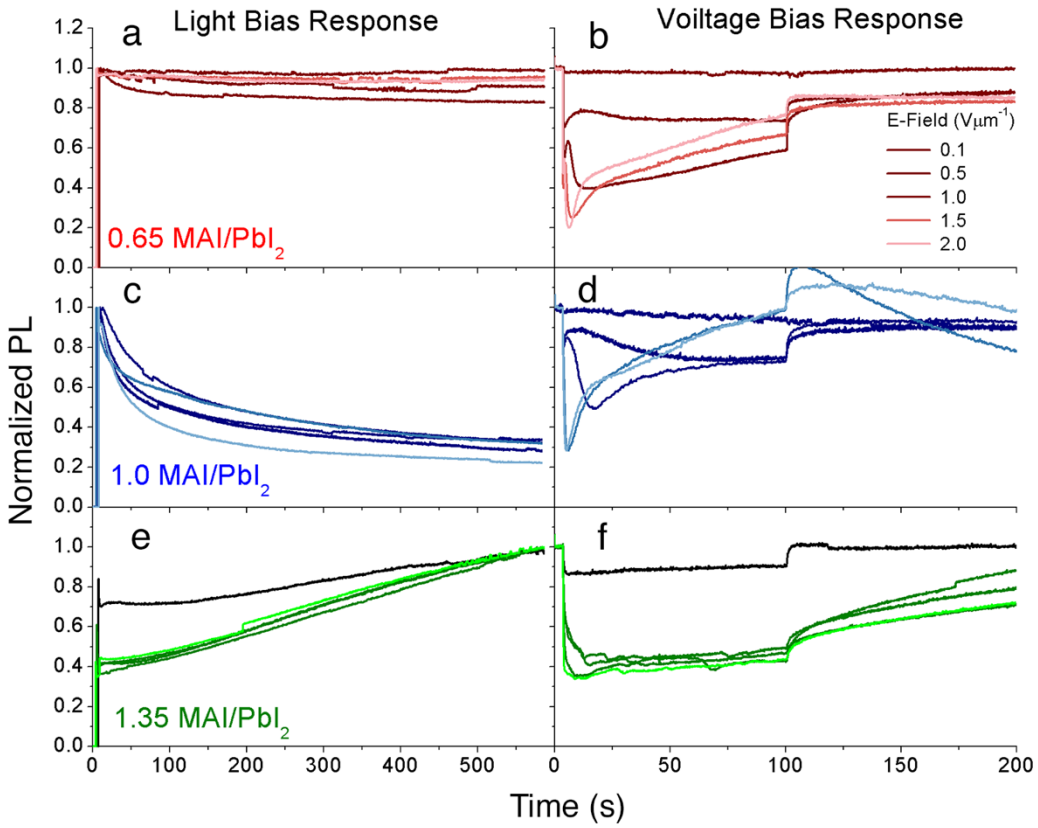

Figure 4.3. Electrical bias-dependent measurements of the STOR across $MAPbI_3$ compositions. Applied electric field strengths range from 100 to 1000 $mWcm^{-2}$ represented as increasing color brightness. Normalized PL response to light soaking experiments (a, c, e) and application of an electrical bias (b, d, f) of $MAPbI_3$ films with precursor composition ratios of [MAI]/[PbI_2] equal to 0.65 (a-b, red lines), 1.0 (c-d, blue lines), and 1.35 (e-f, blue lines).

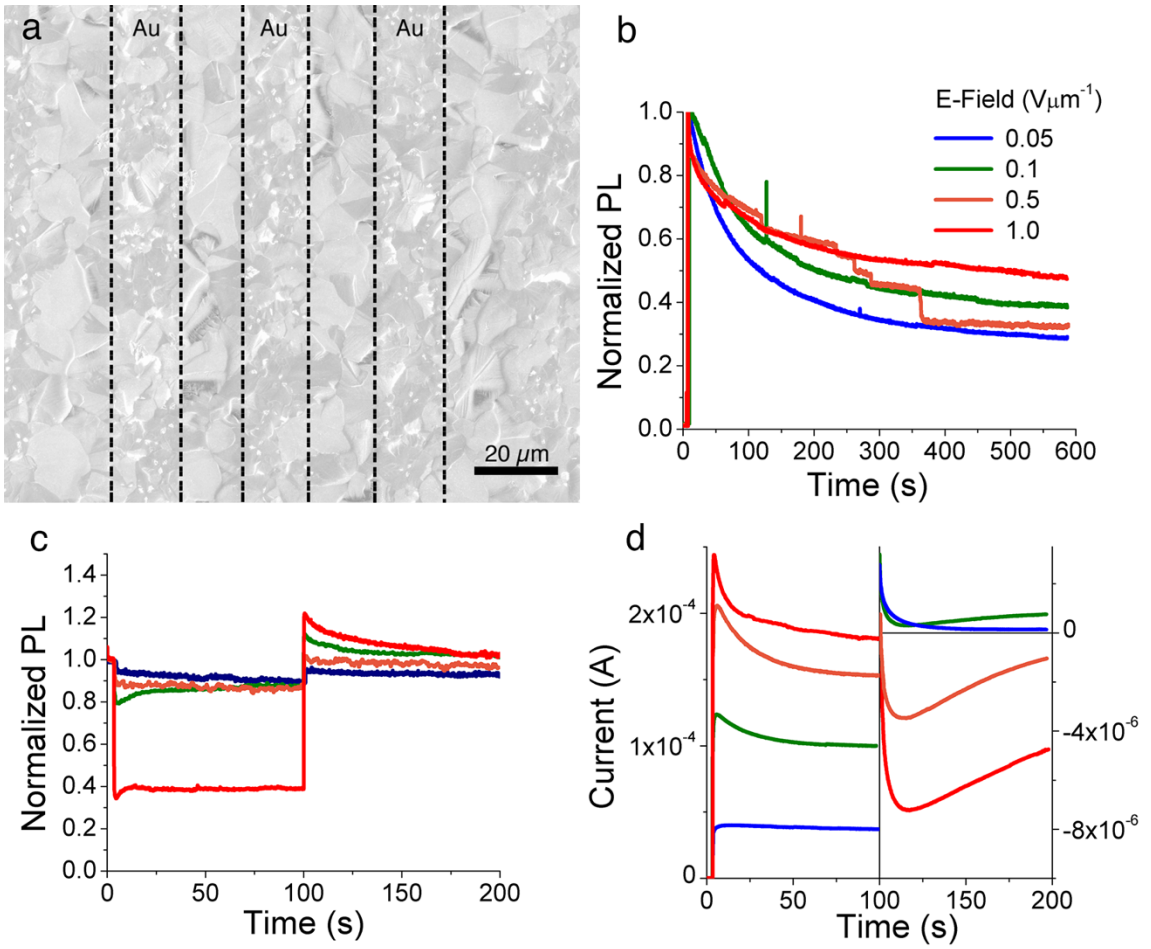

Figure 4.4. STOR measurement of TIMRA treated film. a) SEM image of the TIRMA treated $MAPbI_3$ devices to show the large grains and uniform deposition over the electrodes. Scale bar is 20 μm. b) Normalized PL response to light excitation during light soaking studies under zero applied bias. c) Normalized PL response to the application of an electric field ranging from 0.05 $V\mu m^{-1}$ to 1 $V\mu m^{-1}$ under constant illumination. The bias is turned on about 5 s and turned off at about 100 s. d) Current response to the application of an applied bias. the left column shows the current when the bias is applied, and the right column shows the recovery after the bias is removed. The right column is rescaled to the right axis. The red, blue, and green line color represents a $[MAI]/[PbI_2]$ precursor ratio of 0.65, 1.0, and 1.35, respectively.

CHAPTER 5

CONCLUSIONS AND OUTLOOK

5.1 Conclusions

The slow transient optoelectronic response (STOR) of methylammonium lead triiodide ($MAPbI_3$) was studied in the context of the intrinsic defect properties. The first step toward realizing this goal is to develop a characterization platform that is capable of minimizing the extrinsic factors that may contribute to the STOR while maximizing the available characterization techniques and isolating the intrinsic material response. To that end, a testing platform utilizing a lateral interdigitated electrode (IDE) design was developed. The advantage of this design over the standard vertical solar cell device architecture includes simplified design, single material layer deposition with no buried active layers, and electric field parallel with the substrate enabling polarization-dependent mapping. By studying the dynamic photoluminescence (PL) and current response to applied light and voltage bias, as well as dynamic PL imaging, both a charge trapping and defect ion migration mechanism were identified in the STOR.

To determine the ultimate role of the defects in the STOR of $MAPbI_3$, a strategy to minimize the defects in the $MAPbI_3$ thin films was developed. The novel post deposition annealing technique was based on the unique solid-to-liquid phase transition of $MAPbI_3$ under methylamine (MA) gas. It was found that this phase transition was

reversible at elevated temperatures. Thus, a technique of thermal-induced recrystallization under methylamine atmosphere (TIRMA) was developed. This technique was capable of forming large area and pinhole-free thin films with grain sizes on the order of tens of micrometers, which is at least an order of magnitude larger than those fabricated by other common deposition techniques. These films exhibited significantly higher crystallinity consistent with the observation of very large single crystalline grains. Furthermore, blue shifted optical properties suggest a decrease in possible shallow defect traps, further supporting the high quality crystalline films. Further PL mapping with confocal microscopy was used to analyze the intra-grain carrier dynamics. Spectral and time resolved spatially mapping of a single crystal grain revealed a nonuniform PL response between the bulk crystal grain and the grain boundary. The grain boundary exhibited red-shifted emission and significantly shorter carrier lifetimes, suggesting that the grain is a source of nonradiative recombination. Utilizing the unique off-axis scanning in the confocal microscope, the spatial decay of the PL in the single crystal grain with a fixed excitation spot was mapped and fit to extract a carrier diffusion length of about 1.5 μm. Together with the average PL lifetime of about 35 ns, the free carrier mobility was calculated to be roughly 25 $cm^2V^{-1}s^{-1}$, which is comparable to other high quality films in high-performance devices.

Finally, the film composition and morphology was used as a tool to tune the defect properties of the $MAPbI_3$ film. The composition of $MAPbI_3$ was tuned around the stoichiometric value to create both PbI_2-excess and MAI-excess films. Based on the STOR to applied light and voltage bias, general trends identifiable across composition were revealed. The trends were further probed with light intensity and electrical bias

magnitude dependent studies. Based on these results, important correlations between the observed STOR and the expected defect properties were made. For example, the PbI_2-excess samples exhibited a much faster STOR and more stabilized response, which was attributed to the lack of significant concentrations of deep level defect states and possible PbI_2 passivation at the grain boundary. On the contrary, MAI-excess samples exhibited slow transient responses and only partial recovery, which was attributed to the hypothesized increase in trapping centers at high concentrations of iodide and lead vacancies as well as enhanced degradation due to migration of excess MA ions. Interestingly, stoichiometric samples showed the largest response variability to both light and electrical biases. The decreased stability at this composition was attributed to the large concentration of Schottky defects potentially leading to several different mechanisms. Finally, the STOR of the TIRMA treated films was measured. The results show that the STOR was greatly reduced as a result of the highly crystalline films, however, some unique PL responses are still to be understood.

5.2 Outlook

The findings presented in this thesis show great potential to understand the intrinsic material response of $MAPbI_3$. However, many follow up and supplementary studies are still needed. For example, to further understand the mechanisms behind the compositional dependent STOR, the films should be further characterized with X-ray diffraction (XRD), electron diffraction spectroscopy (EDS), and ultraviolet photoemission spectroscopy (UPS). These should give quantitative insight to changes in the material structure, final film composition, and defect concentrations respectively.

Additional studies beyond the compositional changes to analyze and control the STOR will include: introduction of molecular passivation agents to quench surface traps[1] across varying compositions to probe surface defect chemistry, systematic control of the grain size through surface energy modification,[2] and electrode interface passivation through ETL or HTL deposition on top of the gold electrodes. Future studies will also be expanded to include the high-performance perovskite compositions with A, B, and X-site substitution.[3] Furthermore, the confocal system introduced in Chapter 3 will be used to spatially map the spectral and time resolved PL response of $MAPbI_3$ between the electrode gap before, during, and after an applied electrical bias. This will give unprecedented insight to the charge carrier dynamics and mobile ions in the film relative to the electrode polarity to potentially identify different migrating ion species and other defect dynamics.

The TIRMA treated films will also be further optimized to realize the highest quality films. For example, molecular passivation at the grain boundaries will be used to reduce the nonradiative recombination pathway observed in these films. Surface modification with will be explored by controlling the surface wetting of the liquid to add further control of the recrystallization energy and growth kinetics. Finally, multi-component vapor treatment with formamidine,[4] methylamine, and/or butylamine will be explored as a method to create large grained, multicomponent Ruddlesden-Popper perovskite films with high-performance and improved stability,[5] The high-performance of each of these high quality films will be tested using the STOR characterization platform introduced in this thesis. Furthermore, these films will be fabricated into traditional device architecture to pursue high-performance devices. Based on the STOR

characterization, the TIRMA devices are expected to have low hysteresis and higher stability. The highly crystalline grains, long carrier lifetime, and high mobility suggest that these devices will bridge the thin film and single crystal optoelectronic property gap to realize high-performance devices.

These bottom up studies will be a significant contribution to the field of perovskite photovoltaics in understanding the intrinsic material response. This understanding is necessary for the field to advance from a lab-scale research field, to a competitive technology in the solar energy market.

5.3 References

1. deQuilettes, D. W.; Koch, S.; Burke, S.; Paranji, R. K.; Shropshire, A. J.; Ziffer, M. E.; Ginger, D. S., Photoluminescence Lifetimes Exceeding 8 μs and Quantum Yields Exceeding 30% in Hybrid Perovskite Thin Films by Ligand Passivation. *ACS Energy Lett.* **2016,** *1*, 438-444.

2. Bi, C.; Wang, Q.; Shao, Y.; Yuan, Y.; Xiao, Z.; Huang, J., Non-Wetting Surface-Driven High-Aspect-Ratio Crystalline Grain Growth for Efficient Hybrid Perovskite Solar Cells. *Nat. Commun.* **2015,** *6*, 7747.

3. Saliba, M.; Matsui, T.; Seo, J.-Y.; Domanski, K.; Correa-Baena, J.-P.; Nazeeruddin, M. K.; Zakeeruddin, S. M.; Tress, W.; Abate, A.; Hagfeldt, A.; Gratzel, M., Cesium-Containing Triple Cation Perovskite Solar Cells: Improved Stability, Reproducibility and High Efficiency. *Energy Environ. Sci.* **2016,** *9*, 1989-1997.

4. Zhou, Y.; Yang, M.; Pang, S.; Zhu, K.; Padture, N. P., Exceptional Morphology-Preserving Evolution of Formamidinium Lead Triiodide Perovskite Thin Films via Organic-Cation Displacement. *J. Am. Chem. Soc.* **2016,** *138*, 5535-5538.

5. Tsai, H.; Nie, W.; Blancon, J.-C.; Stoumpos, C. C.; Asadpour, R.; Harutyunyan, B.; Neukirch, A. J.; Verduzco, R.; Crochet, J. J.; Tretiak, S.; Pedesseau, L.; Even, J.; Alam, M. A.; Gupta, G.; Lou, J.; Ajayan, P. M.; Bedzyk, M. J.; Kanatzidis, M. G.; Mohite, A. D., High-Efficiency Two-Dimensional Ruddlesden–Popper Perovskite Solar Cells. *Nature* **2016,** *536*, 312-316.